

# **Custom-Designed Biohybrid Micromotor for Potential Disease Treatment**

Von der Fakultät für Naturwissenschaften der Technischen Universität Chemnitz  
genehmigte Dissertation zur Erlangung des akademischen Grades

*doctor rerum naturalium*

(Dr. rer. nat)

Vorgelegt von M.Sc. Haifeng Xu

geboren am 10. Juli 1990 in Jilin, China

eingereicht am 19. September. 2019

Gutachter: Prof. Dr. Oliver G. Schmidt  
Prof. Dr. Klaus Reinhardt

Tag der Verteidigung: 12. März. 2020

<https://nbn-resolving.org/urn:nbn:de:bsz:ch1-qucosa2-710484>



# Bibliographic Information

Haifeng Xu

Custom-Designed Biohybrid Micromotor for Potential Disease Treatment

Technische Universität Chemnitz, Fakultät für Naturwissenschaften, Dissertation, 2020

131 Seiten

## Abstract

Micromotors are recognized as promising candidates for untethered micromanipulation and targeted cargo transport. Their future application is, however, hindered by the low efficiency of drug encapsulation and their poor adaptability in physiological conditions. To address these challenges, one potential solution is to incorporate micromotors with biological materials as the combination of functional biological entities and smart artificial parts represents a manipulable and biologically friendly approach.

This dissertation focuses on the development of custom-designed micromotors combined with sperm and their potential applications on targeted diseases treatment. By means of 2D and 3D lithography methods, microstructures with complex configurations can be fabricated for specific demands. Bovine and human sperm are both for the first time explored as drug carriers thanks to their high encapsulation efficiency of hydrophilic drugs, their powerful self-propulsion and their improved drug-uptake relying on the somatic-cell fusion ability. The hybrid micromotors containing drug loaded sperm and constructed artificial enhancements can be self-propelled by the sperm flagella and remotely guided and released to the target at high precision by employing weak external magnetic fields. As a result, micromotors based on both bovine and human sperm show significant anticancer effect. The application here can be further broadened to other biological environments, in particular to the blood stream, showing the potential on the treatment of blood diseases like blood clotting. Finally, to enhance the treatment efficiency, in particular to control sperm number

and drug dose, three strategies are demonstrated to transport swarms of sperm. This research paves the way for the precision medicine based on engineered sperm-based micromotors.

**Keywords:** micromotors, sperm, drug delivery, cancer treatment, blood diseases, untethered robotics

# Table of Contents

1. General introduction .....	1
1.1. Motivation and goals .....	1
1.2. Structure of the dissertation .....	3
2. Background and state-of-the-art .....	5
2.1. Manufacturing at the microscale .....	5
2.1.1. Femtosecond two-photon lithography (FSTL) .....	6
2.1.2. Other fabrication methods .....	11
2.2. Motion at the microscale .....	12
2.2.1. Theory .....	12
2.2.2. Micromotors for therapeutic applications .....	14
2.3. Sperm-based micromotors .....	20
3. Materials and methods .....	23
3.1. Fabrication of microstructures .....	23
3.1.1. Coding .....	23
3.1.2. FSTL manufacturing .....	29
3.1.3. Electron beam evaporation .....	29
3.2. Fabrication of microfluidic chips .....	30
3.3. Liposomes immobilization .....	32
3.4. Drug loading in sperm .....	33
3.4.1. Sperm preparation .....	33
3.4.2. Drug loading process .....	33
3.4.3. Evaluation of the drug loading efficiency .....	34
3.4.4. Evaluation of encapsulation stability .....	36

3.4.5.	Evaluation of the sperm viability after drug loading .....	36
3.4.6.	Evaluation of the motility of DOX-HCl-loaded sperm .....	36
3.5.	Cancer cell culture .....	37
3.5.1.	Culture of HeLa cells and spheroids .....	37
3.5.2.	HGSOC-representative ex vivo tumour cell culture and spheroids .....	37
3.5.3.	Evaluation of antitumor efficacy of DOX-HCl loaded sperm .....	37
4.	Tetrapod-like sperm-motor for targeted drug delivery .....	39
4.1.	Background .....	39
4.2.	Drug loading in sperm .....	40
4.3.	Sperm-motor transport .....	45
4.4.	Cancer treatment .....	48
4.4.1.	Antitumor efficacy of drug loaded sperm .....	48
4.4.2.	Cancer treatment by DOX-HCl loaded sperm-motors .....	52
4.5.	Summary .....	55
5.	Human sperm as a medication for early ovarian cancer .....	57
5.1.	Background .....	57
5.2.	DOX-HCl loading in human sperm .....	59
5.3.	Anticancer effect .....	63
5.4.	Streamlined sperm-motor transport toward tumor spheroid .....	67
5.5.	Summary .....	71
6.	Sperm-motors for cargo delivery through flowing blood .....	73
6.1.	Background .....	73
6.2.	Design and characterization .....	75
6.3.	Swimming in blood .....	76

6.4.	Swimming against blood flow.....	78
6.5.	SHC sperm-motor for anti-coagulation application.....	83
6.6.	Summary.....	86
7.	Transport of multiple motile sperm cells.....	88
7.1.	Background.....	88
7.2.	Self-assembled train-like sperm-motors swarm.....	88
7.3.	Helical microcourier combined with a protein-based microflake .....	91
7.4.	Multi-pocket sperm-bus.....	101
7.5.	Summary.....	102
8.	Conclusions and Outlook.....	104
8.1.	Achievements.....	104
8.2.	Outlook .....	107
8.2.1.	Biology study .....	107
8.2.2.	Robotics study.....	108
	Bibliography: .....	110
	List of Figures .....	123
	Selbständigkeitserklärung.....	130
	Acknowledgements .....	132
	Publications.....	134
	Curriculum Vitae .....	136

## List of Abbreviations

<b>AFM</b>	atom force microscope	<b>HCl</b>	Hydrochloride
<b>BSA</b>	bovine serum albumin	<b>HLS</b>	Heparin loaded sperm-micromotor
<b>CLSM</b>	confocal laser scanning microscope	<b>MC</b>	microcourier
<b>DOX</b>	doxorubicin	<b>MF</b>	microflake
<b>DMEM</b>	Dulbecco's modified Eagle's medium	<b>NHS</b>	hydroxysuccinimide
<b>EDC</b>	1-ethyl-3-(3-dimethylaminopropyl) carbodiimide	<b>PBS</b>	phosphate buffer solution
<b>EDTA</b>	ethylene diamine tetraacetic acid	<b>PDMS</b>	polydimethylsiloxane
<b>FBS</b>	fetal bovine serum	<b>PNIPAM</b>	poly isopropyl acrylamide
<b>FSTL</b>	Femtosecond two-photon lithography	<b>SHC</b>	Streamline-horned cap
<b>HA</b>	Hyaluronic acid	<b>SP-TALP</b>	sperm-Tyrode's albumin lactate pyruvate
		<b>STIC</b>	serous tubal intraepithelial carcinoma



# 1. General introduction

## 1.1. Motivation and goals

Since the microworld started to show itself to human beings, people have been dreaming to make a nano or microscale vehicle that can voyage in the microworld, transport cargos and perform more complex operations based on one's imagination. In 1951, Taylor first discussed the swimming behavior of microorganisms and proposed a sheet model for the movement of the cells with flagella.<sup>1</sup> In 1959, Feynman passionately contemplated the future use of microscale robots in his historic lecture "There is plenty of room at the bottom". He specifically suggested the idea to "swallow a surgeon" to treat the wounds deep in our body where the traditional tools cannot reach and do the job in a non-invasive way.<sup>2</sup> This has fascinated people in the miniaturization of robots ever since. A famous movie "Fantastic Voyage" in 1966 picked up this idea and brought the audience into a future world where scientists could miniaturize a sailor in a microscale submarine so that they can travel in the blood circulation system and cure an injury in the human body, in particular performing laser ablation to tumor.<sup>3</sup>

Certainly, researchers have also been inspired and dedicated a huge effort on the study of robotics at the microscale. Diverse creative microscale robots (termed micromotors, microjets, microengines, microswimmers, or micropropellers, of which the sizes usually between 100 nm to 1 mm) have been invented and leading us closer and closer to valuable biomedical applications.<sup>4</sup> Medical treatments based on micromotors benefit from their mobility, compared to the earlier developed passive drug carriers, such as liposomes, nanoparticles and microcapsules.<sup>5</sup> During the use of passive drug delivery systems in the past decades, more and more problems have emerged, such as undesired accumulation due to the lack of active actuation system, fast clearance and degradation due to the elimination of the liver and blood,<sup>6</sup> decreased effective drug concentration due to the dilution by body fluid<sup>7</sup> and limited tissue penetration.<sup>8</sup> To address such challenges, micromotors are

therefore expected to be one of the next generation of drug delivery solution. To do the job at the microscale, micromotors have to overcome several hurdles. Firstly, locomotion of micromotors at low Reynold numbers in liquid environments are facing more difficulties than the macroscopic motors, due to the relatively strong Brownian noise under a negligible impact of the inertia.<sup>4</sup> Second, as the problem-solving abilities of micromotors rely on specific functionalizations or loaded cargos, elegant techniques are needed to endow micromotors with specific abilities without damaging them, which represents big challenges on manipulation at the microscale. Moreover, regarding the biomedical applications, the adaptability of micromotors can never be ignored. This also excludes all micromotors relying on extreme conditions which are harmful to the human body, such as high voltage electric field, violent chemical reactions and pathogenic bacteria. To address these challenges, combining biological components is expected as an efficient solution.

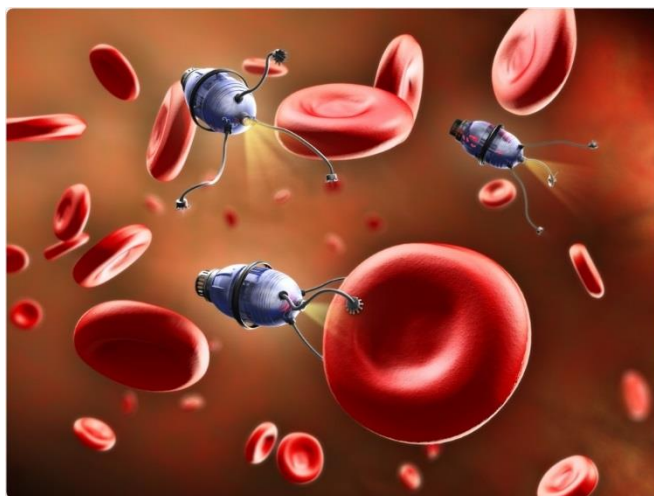


**Figure 1.** Prospective scenario of micromotors working in blood.<sup>9</sup> Reproduced with permission from © Conference Series LLC Ltd.

The sperm, as a highly differentiated cell, is a promising candidate to construct a hybrid micromotor to address the abovementioned challenges, thanks to the powerful propulsion provided by the sperm and its openness to various functionalizations for diverse applications. With the help of precise nano-manufacturing method, nowadays it is not as

unimaginable as before to artificially equip sperm to be functional micromotors as demanded. All of these motivate us to the main goal to develop novel sperm hybrid micromotors (sperm-motors) that could potentially work in the human body. These sperm-motors could be precisely navigated to the target site and controllably treat the diseases in situ in a non-invasive way.

## 1.2. Structure of the dissertation

This dissertation is organized as follows:

Chapter 2 introduces the background of the micromotors, from the manufacturing means at the microscale to the current research advances, focusing on biomedical applications. Thereafter, the superiority of the sperm as a biohybrid component to construct micromotors is emphasized, highlighting the motivation to develop sperm-motors towards disease treatment.

Chapter 3 details the experimental procedures in the manufacturing of the artificial component of sperm-motors, the functional treatment of sperm, the construction of sperm-motors and the essential evaluations of their applications on disease treatment.

Chapter 4 demonstrates the development of a tetrapod-like sperm-motor (sperm-tetrapod) and its application on cancer treatment. The artificial component here has a tubular body that can couple the sperm, and four arms that can bend and controllably release the sperm. The sperm-tetrapod can be precisely guided by an external magnetic field relying on the magnetic coating on the artificial component. When the sperm is loaded with anti-cancer drug, the sperm-tetrapod shows an effective cancer cell-killing effect.

Chapter 5 shows our exploration of the anti-cancer usage of sperm from bovine sperm treating over-passaged cancer cells to human sperm treating early passaged cancer lesion. Research in this chapter explains the suitability of sperm as drug carriers and introduces this sperm-based system one step closer to the application in the human body.

Chapter 6 demonstrates the development of a sperm-motor based on a streamline-horned cap (SHC) and its application in the blood circulation system. Achievements presented in this chapter not only broadens the administration route of the sperm-motor based drug delivery system, but also opens the gate for micromotors' application in blood against flow comparable to the realistic blood stream in the human body.

Chapter 7 introduces several strategies for multiple sperm transport towards higher drug dose based on more sperm and artificial components, or towards higher working efficiency of sperm. Particularly, a transport system based on a sperm adherent microflake and a helical microcourier is highlighted.

Chapter 8 summarizes all the achievements during the research and concludes the dissertation. Outlook with the following research directions and future applications is discussed.

## 2. Background and state-of-the-art

### 2.1. Manufacturing at the microscale

In the development of microrobotics, there has been a high demand for smaller and smaller machinery parts with more and more fine structures. Traditional macro mechanical manufacturing technology cannot meet the requirements of the machining precision of these microscale systems. Fine processing with a resolution at the nanoscale is thus critically important.

Bottom-up methods based on phase transition mechanism have been widely used to prepare passive micro or nanoscale drug delivery systems, such as liposomes, nanoparticles, microspheres and microcapsules.<sup>10</sup> However, no fine structure can be obtained from this uncontrollable technique based on self-assembling.<sup>11</sup> On the contrary, micro- and nanomanufacturing technology based on photo-lithography makes it possible to precisely design and polish the required devices or parts in details. This top-down technology allows specific reactions, for example photopolymerization, occurring locally at the specified position based on pre-programmed design. The patterning at the microscale mainly relies on a pre-fabricated mask or a maskless method based on directly laser writing.<sup>12</sup> However, the diffraction limit of lasers restricts the manufacturing resolution,<sup>13</sup> which has motivated the development of varieties of lithography methods in the recent decades (e.g. extreme ultraviolet lithography (EUVL), electron beam lithography (EBL), nanoimprint lithography (NIL), etc.), focusing on decreasing the wavelength of the laser, increasing the exposure intensity and dipping the lens in specific immersion liquids.<sup>13</sup> Among all existing lithography techniques, two-photon lithography has been regarded as one of the most promising methods to fabricate three-dimensional (3D) structures,<sup>14</sup> especially for the fabrication of micromotors.

### 2.1.1. Femtosecond two-photon lithography (FSTL)

Traditional lithography is generally a single-photon exposure process in 2D. Although 2D exposure technique can be used to manufacture the device with shape change in the third dimension by exposing the resist layer by layer, it is not possible to construct complex 3D structure with high resolution. The solution is to combine two techniques, two-photon lithography and femtosecond pulsed laser. FSTL is an ultra-fine processing technique that integrates ultra-fast laser technique, ultrahigh-precision positioning technique and photopolymerization technique.<sup>15</sup>

#### (1) Mechanism of FSTL

Femtosecond laser is an ultra-fast laser with a time-bandwidth at the femtosecond scale. It has ultra-high instantaneous power due to the highly repeated frequencies of the lasers. This high power enables the structure change of the material at the molecular level, inducing etching or polymerization. Besides, it has ultra-short pulse duration of the order of  $10^{-12}$  second.<sup>16</sup> This short action time does not induce thermal effect, protecting the treated material from thermal deformation.<sup>17</sup> Thus, FSTL only allows the chemical change of the photoresist occurring at the focal spot of the laser after a two-photon absorption, generating programmable 3D patterns. Since FSTL is seldom used on positive-tone resists, we will focus on its application on two-photon polymerization in this chapter. **Figure 2.1a** explains the process of two-photon absorption differently from a general single-photon absorption. In the process of a single-photon absorption, a molecule at the ground state absorbs one photon when the photon energy of the excitation laser equals the energy distance between the ground state and the excitation state of the electron. Then the excited electron induced the formation of breaking of specific chemical bonds.<sup>14</sup> In the two-photon absorption process, the illuminated molecule absorbs the first photon and goes into a virtual state with a very short duration or an actual state in a generally called stepwise absorption process. Local polymerization can result when the second photon arrives before the excited state decays. The absorption rate of two-photon process is formulated below:<sup>18</sup>

$$P = \sigma \frac{I^2}{h\nu}$$

where  $P$  represents the two-photon absorption rate,  $\sigma$  represents the two-photon absorption coefficient,  $I$  represents the illumination light intensity,  $h$  represents Planck constant and  $\nu$  represents the excitation light frequency. Since the two-photon absorption rate is directly proportional to the squared excitation light intensity, femtosecond laser stays as an advantageous choice for the laser source thanks to its high intensity density within a pulse duration. Besides, the two-photon induced polymerization only occurs at the position where the illumination intensity exceeds a certain threshold, as shown in **Figure 2.1b**. When the laser with a high intensity but a long wavelength is used, the size of the illumination threshold can be adjusted much smaller than the size of the focused laser spot, decided by the nonlinear optical effect of the applied material. Thus, the polymerization size of FSTL is much smaller than the laser diffraction limit, improving the manufacturing fineness to below 100 nanometers.<sup>18</sup> Besides, FSTL allows the efficient absorption through a thin film or non-transparent liquid sample by using infrared laser.<sup>19</sup> Combined with an ultra-precise motorized objective stage, 3D manufacturing with fine details below 100 nm can be achieved by precisely controlling the laser on/off and the focusing position out of pre-programmed CAD codes.

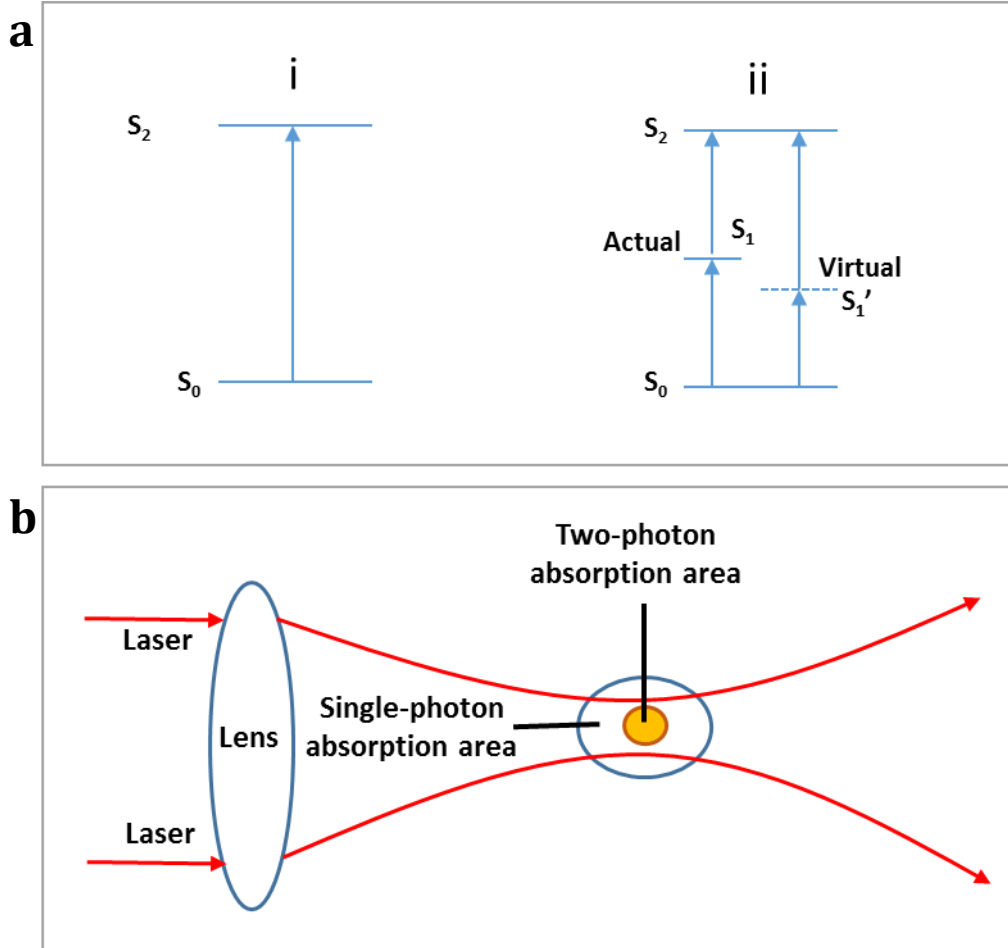


**Figure 2.1.** Difference between single-photon and two-photon absorption processes on (a) energy level; (b) exposure area.

A general FSTL platform is depicted in **Figure 2.2**. Femtosecond laser is focused inside the material through an objective with a large aperture. The exposure time and laser power can be adjusted by the shutter and attenuator. The exposure position is controlled by a micro-motorized system comprised of a piezoelectric-drive micro displacement platform, a galvanometers array and a motorized stage of the microscope. The manufacturing process can be real-time monitored by an external CCD system.<sup>20,21</sup> There are three positioning modes in the FSTL, namely stage moving, galvo scanning and piezo scanning modes. The stage movement is used to position the desired region of the photoresist under the objective.



This positioning can be fast but very coarse. The galvo scanning mode is suitable for the segment-to-segment manufacturing method, of which the manufacturing resolution is decided on the size of each segment.<sup>22</sup> Thanks to a low rotational inertia of the galvo, the response of the galvo scanning can be as fast as 0.5 ms. The piezo scanning mode has the highest resolution due to a high precision of the piezoelectric-driven platform (1 nm). However, due to the high inertia of the platform, the piezo scanning mode needs a long waiting time (more than 10 ms) after a large displacement. Thus, the piezo scanning mode is appropriate for a point-to-point writing method, in which the distance of two points is below 50 nm. This method is used to process the details of the sample, slowly but with a high resolution. By means of a combination of three positioning modes, microstructures can be fabricated precisely and fast in a large number of arrays.

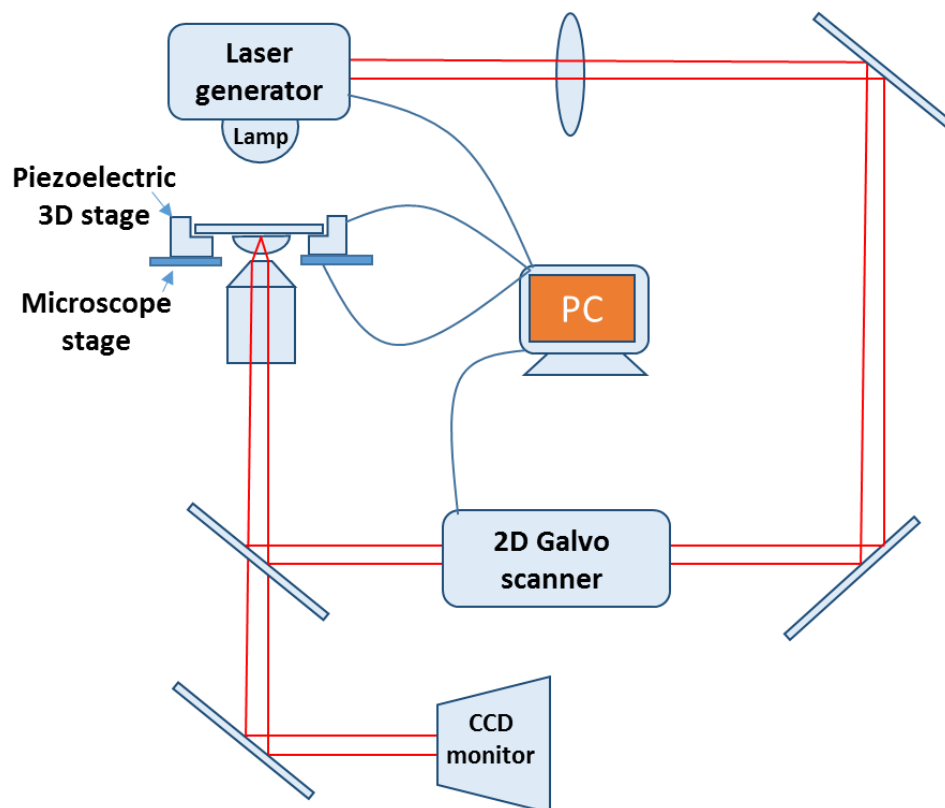


**Figure 2.2.** Typical FSTL setup

## (2) Applications of FSTL

FSTL makes it possible to manufacture complex devices in 3D dimensions with an ultra-high precision at fast speed. Early in 1997, Prof. Kawata in Osaka University first successfully fabricated a helical tube with a resolution at 120 nm by using FSTL.<sup>20</sup> In 2001, Nature reported the milestone research from his group, a 3D micro-cattle around 10  $\mu\text{m}$  long and 7  $\mu\text{m}$  tall (**Figure 2.3a**).<sup>23</sup> It took them 3 h to fabricate a single structure. Since then, FSTL has been largely improved on not only the processing efficiency, but also the processing resolution. A surging number of materials have been developed for 3D processing by FSTL with diverse properties. In terms of biomedical applications, FSTL are attracting attentions from researchers in various fields, including tissue engineering, microscopic imaging, and the study of microscale apparatus and new drug delivery strategies. **Figure 2.3b** illustrates a microscaffold made of three different photoresists that can selectively be functionalized with different proteins, allowing directed cells attachment in 3D.<sup>24</sup> Similarly, Marino et al. fabricated a porous microtube as scaffold for endothelial-like cells culture. This cell seeded microtube showed a potential to mimic the blood brain barrier.<sup>25</sup> Choi et al. recently fabricated a series of micromotors by FSTL for the purpose of cells transplantation. The micromotors could carry human stem cells and transport them in a mouse brain slice, indicating a potential remote control on tissue engineering.<sup>26</sup> Representing one of the most important applications of FSTL, more applications of FSTL on micromotors will be discussed in details in Section 2.2.

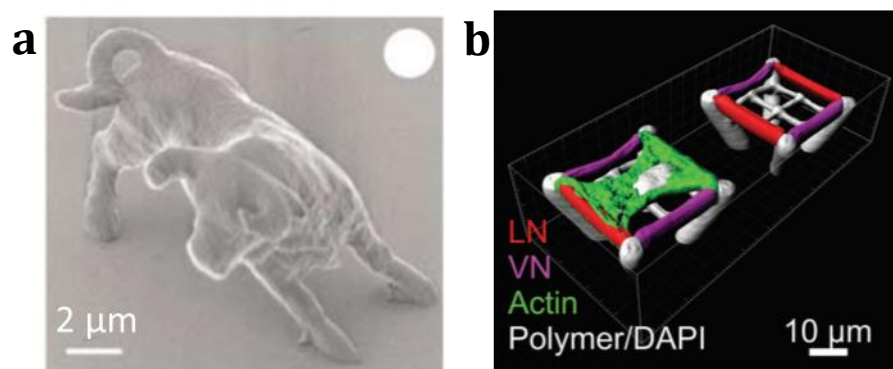


**Figure 2.3.** Examples of FSTL products: (a) Microcattle;<sup>23</sup> Reproduced with permission from Copyright © 2019, Springer Nature. (b) Microscaffold for cell culture.<sup>24</sup> Reproduced with

### 2.1.2. Other fabrication methods

As introduced above, the fabrication of micromotors can be generally classified as top-down and bottom-up methods. While FSTL represents one of the most recently established top-down methods, 2D lithography is the most commonly used one as an inexpensive method with high fineness and yield. In general, 2D lithographic processing relies on a pre-prepared photomask. The laser beam (e.g. UV light, visible light, ion beam) is projected on the photoresist-coated substrate through the mask, resulting in a polymerization or etching on the programmed region. The processing resolution is influenced by the fineness of the mask, the property of the photoresist and especially the diffraction limit of the applied laser. After further steps of baking and developing, 2D patterns at the microscale with the nanoscale resolution can be obtained.<sup>13</sup> Micromotors can be obtained by coating these microstructures with functional metal layers and detaching them off. As an example, our institute fabricated a catalytic microtube based on a rolled-up method by 2D lithography in 2009. Platinum coating on the surface enabled it to catalyze local decomposition of the  $\text{H}_2\text{O}_2$  fuel into  $\text{O}_2$  bubbles, initiating an autonomous propelling of the microtube.<sup>27</sup>

The bottom-up approach relying on molecular self-assembly is also widely used in the fabrication of micromotors without complex structures. The processing is inexpensive and fast, though custom design is not supported. Based on different molds or templates, various structures including Janus particles, microrods and microtubes can be obtained by homogenous phase transition,<sup>28</sup> electrodeposition<sup>29</sup> and layer-by-layer assembling.<sup>30</sup> Considering the diversity of this approach, more details about the applications will be explained in the next section in relation with specific micromotors. As a summary, a chart of the fabrication methods for micromotors can be found in **Figure 2.4**.

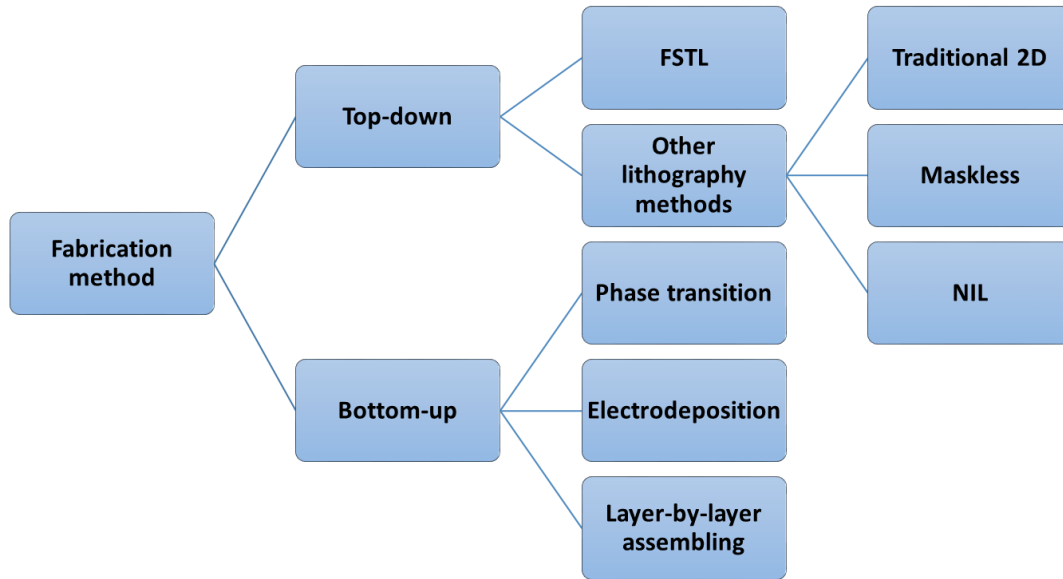


**Figure 2.4.** Fabrications methods for micromotors

## 2.2. Motion at the microscale

### 2.2.1. Theory

Motion of nano and micromotors in a Newtonian fluid is challenged by the absence of inertial forces. For an object swimming in fluid, the significance of the inertial forces relative to the viscous forces is decided by its Reynolds number, formulated as:<sup>4</sup>

$$Re = \frac{\rho a v}{\eta} = \frac{\text{Inertial forces}}{\text{Viscous forces}}$$

Where  $\rho$  is the fluid density,  $\eta$  is the fluid viscosity,  $v$  is the moving velocity of the object relative to flow and  $a$  is the characteristic dimension. Micromotors with low swimming velocity have very small Reynolds numbers ( $Re \ll 1$ ). For example, for a human sperm

swimming in water ( $a \sim 10 \mu\text{m}$ ,  $v \sim 100 \mu\text{m/s}$ ,  $p \sim 10^3$ ), the Reynolds number is around  $10^{-3}$ . Propulsion at the microscale at inertia-less regime thus requires fundamentally different mechanisms from macroscopic motion. In 1977, Purcell visualized the locomotion factors of miniature devices in fluid. To the opposite of macroscopic swimmers, micromotors cannot be propelled by time-reversible gliding.<sup>31</sup> For instance, when a microscale scallop moves forward by flapping its arms, it will return its initial position by resetting its arms, achieving zero net displacement (**Figure 2.5**). In view of this, locomotion at the microscale needs a continual propulsion system and an asymmetrical motion mechanism, either by a shape change with a deformable body or by a corkscrew-like motion. For example, some bacteria propel themselves by continuously bending their flagella. Likewise, sperm swim at a combinational mechanism with beating their flexible flagella and screwing their heads.<sup>32</sup>

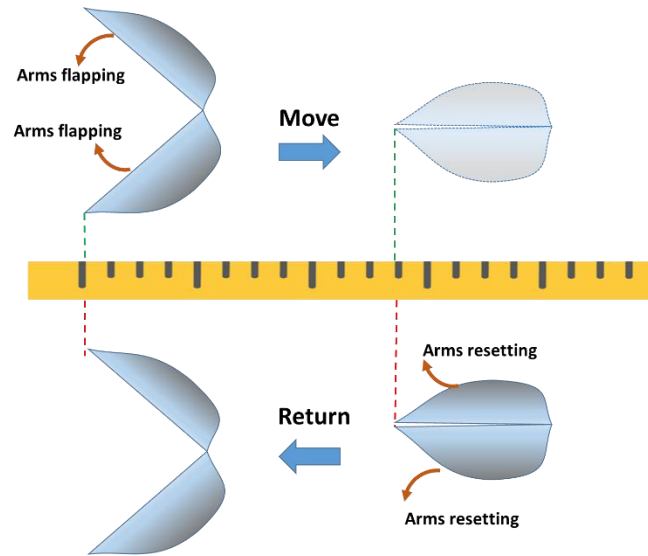


**Figure 2.5.** A microscale scallop in low Reynolds number conditions.

When the inertial forces are neglected in low Re numbers systems, motion at the microscale is highly dominated by the hydrodynamic resistance. In Newtonian fluid, the Navier-stokes equations that describe flow property can be then simplified as:<sup>33</sup>

$$-\nabla p + \mu \nabla^2 u = 0, \nabla \cdot u = 0$$

Where  $u$  represents the flow field,  $\mu$  represents the fluid viscosity and  $p$  represents the flow pressure. The linearity and instantaneity of the equations imply that the thrust force of the micromotor is counterbalanced by the hydrodynamic resistance (drag force) on it ( $F_{thrust} = F_{drag}$ ).<sup>33</sup> This principle has been extensively applied on the calculation of the propulsion force of micromotors, as the hydrodynamic resistance of a specific object can be calculated according to its configuration, surface features and the fluid properties. With the help of finite element analysis, the estimation of the propulsion force has been more and more efficient.

### 2.2.2. Micromotors for therapeutic applications

The following section is mainly based on the publication titled on “Micro- and nano-motors: the new generation of drug carriers” in *Therapeutic Delivery*. Reprinted with permission from [Therapeutic delivery, 2018, 9(4): 303-316] ([doi.org/10.4155/tde-2017-0113](https://doi.org/10.4155/tde-2017-0113)).<sup>5</sup> Copyright[2017] Future Science. Micromotors are attractive for diverse biomedical applications, especially on targeted drug delivery, offering advantages such as rapid transport, high tissue penetration and motion controllability. Compared to passive nano or microcarriers (e.g. liposomes, nanoparticles, microspheres) with low targeting efficiency, micromotors with powerful propulsion and intelligent guidance mechanisms can precisely transport drug to desired locations with a deviation in several micrometers. In general, micromotors can be categorized in three types according to the propulsion mode: chemical, physical and biological micromotors (**Figure 2.6**).<sup>34</sup>

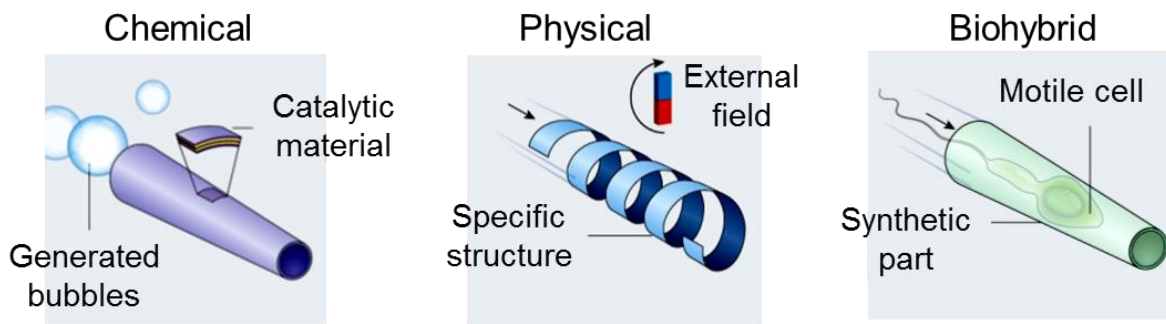


**Figure 2.6.** Three micromotor prototypes.<sup>34</sup>

## (1) Chemical micromotor

The chemical micromotor transforms the energy from a local chemical reaction into motion. It often contains an active substance (e.g. Mg, Pt, Ag, Pa) which can react with the environmental liquid or catalyze the decomposition of it. The micromotor is usually designed with asymmetrically distributed active materials to react with the liquid fuel and generate bubbles at the back end of the micromotor, facilitating its forward motion. The first demonstration of catalytic micromotors to capture and transport cargo was done by Sen's group in 2008, in which an Au-Pt bimetallic nanorod was propelled in  $\text{H}_2\text{O}_2$  solution by the decomposition product:  $\text{O}_2$  bubbles. Polystyrene particles were captured via electrostatic interaction by the nanorod and controllably transported at the presence of a Ni segment for externally magnetic guidance.<sup>35</sup> Since then, assorted Pt based micromotors have been fabricated out of different motivations. For instance, Kagan et al. showed for the first time the capture, transport and release of doxorubicin (DOX, a broad-spectrum anticancer drug) loaded polymeric particles and liposomes by using a similar Au-Pt micromotor. The release of such cargo was accomplished by a fast reversal of the micromotors' motion whereby the drag force imposed on the cargo counterbalanced the magnetic attraction from the microrod on it.<sup>36</sup> In the same year, Solovev et al realized the controlled manipulation and release of multiple microscale objects, including cells, by using rolled-up catalytic microengines. These microtubes were fabricated based on micro-patterns by 2D lithography. After the patterning, Ge, Pt and Ni layers were sequentially deposited as the sacrificial layer, the catalyst layer and the magnetic guidance layer, respectively. When the metals coated patterns were immersed in water, Ge layer was asymmetrically dissolved so that the residual metal layers were rolled by the created tension force. This was the first tubular micromotor and thus opened a way to transport cells on demand to build or repair tissues, as now has been shown by several groups.<sup>37</sup> However, the introduced systems were not ideal for medical applications as they relied on the use of toxic  $\text{H}_2\text{O}_2$  as fuel for their motion, making it necessary to identify more suitable materials and fuels. An alternative material is Mg, which is stable at room temperature and can react with water and create bubbles in an efficient manner. The metallic form of Mg is biocompatible and its ions are among the most abundant ones in the human body, being essential for the function of many organs.<sup>38</sup> As an explorative in vivo approach,

Wang et al. reported the application of Mg-based microparticles on the treatment of the infection in mouse's stomach. PLGA and chitosan were coated on the microparticles to encapsulate clarithromycin, an antibiotic drug. The motor was driven by the gastric acid in the stomach. It released clarithromycin during the dissolving of Mg. Although real-time tracking and guidance were not performed in the stomach of the mouse, a higher anti-infection efficacy was achieved compared to the passive microparticles.<sup>39</sup> Considering the applicability in the acid-free environment in vivo, Al-Ga/Ti was employed as a material combination that allows the motion of micromotors in water without the need of toxic fuels. This motion principle was based on the continuous hydrogen generation via liquid-metal embrittlement in the Al-Ga system, a reaction that happened between the Al alloy and water.<sup>40</sup> Such micromotors were also able to move in biological media but they exhibited a very short lifespan (few minutes). To date, no cargo release has been demonstrated with this system.

Enzymatic micro- and nano-motors can also move with biocompatible fuels such as glucose and urease. Here, the enzymes convert the chemical energy into kinetic motion. Since Feringa et al. reported the first carbon nanotube driven by enzymatic reactions in 2005,<sup>40</sup> different synthetic structures have been used to immobilize or carry enzymes to react with body fluid mimicking environment, leading to self-propulsion via enhanced diffusion or bubble formation. Recently, Sanchez's group reported the use of silicates based mesoporous nanomotors which moved in urease-based media relying on enzymatic reaction to carry and deliver DOX-HCl onto cancer cells in vitro. The drug-loaded nanomotors were shown more effective in killing cancer cells when they were in presence of urea, compared to passive carriers, due to the motor kinetics and the ammonia production by the catalytic decomposition of urea.<sup>41</sup> As a summary, detailed information of chemical micromotors is summarized in **Table 1**.<sup>5</sup>

Material	Propulsion mechanism	Guidance mechanism	Cargo(drug)	Loading mechanism	Target	Cargo release mechanism	Ref.
Au/Pt bimetallic nanorods	Catalytic (H <sub>2</sub> O <sub>2</sub> )	Magnetic	Biodegradable PLGA particles	Electrostatic – Catalytic	-	Drag force	36



Hollow Janus particles with Au nanoparticles and catalase enzyme	Catalytic (H <sub>2</sub> O <sub>2</sub> )	Magnetic	DOX	Physical absorption	HeLa cells	NIR	42
Biodegradable BSA/poly-L-lysine/gelatin and enzyme rocket	Catalytic (H <sub>2</sub> O <sub>2</sub> )	Magnetic	DOX	Physical absorption	HeLa cells	NIR	43
Mg based particles	Catalytic (acid)	pH-taxis	Antibiotic drug	Physical absorption	Mouse stomach	pH change	44,45
Hybrid stomatocyte nanomotors made of block copolymers	Catalytic (H <sub>2</sub> O <sub>2</sub> )	-	DOX	Physical entrapment	HeLa cells	pH-reducing agent	46,47
PEDOT/MnO <sub>2</sub> Janus beads	Catalytic (H <sub>2</sub> O <sub>2</sub> )	-	CPT	Electrostatic interaction	-	-	48
CaCO <sub>3</sub> based particles	Catalytic (acid)	-	Coagulation factors	Physical absorption	Bleeding sites	pH change	49
Silicates based mesoporous beads	Catalytic (urea)	-	DOX	Physical absorption	HeLa cells	Diffusion	41

**Table 1.** Details of chemical micromotors

## (2) Physical micromotors

Physically driven micro- and nano-motors are of great interest, especially for biomedical applications due to their fuel-free motion, as they can be actuated by external means such as magnetic fields, ultrasound and light. Dreyfus fabricated the first physically driven micromotor which contains a DNA-linked chain of colloidal magnetic particles as a magnetically driven flagellum.<sup>50</sup> This microswimmer was moved by oscillating the external magnetic field. For a better control on the guidance and geometry of the micromotor, Nelson et al. reported a helical micromotor fabricated by lithography. The swimming locomotion of this helical motor could be precisely controlled by three orthogonal electromagnetic coil pairs.<sup>51</sup> In 2014, their group developed a similar helical motor for remote-controlled targeted single-cell drug delivery. The micromotor was fabricated by FSTL with a higher fineness, facilitating a higher yield and a more precise control. Ni was coated on the surface as a magnetic layer to enable the remote guidance by an external rotating magnetic field. Calcein, as model drug was loaded on these motors with the help of the encapsulation of liposomes. Efficient calcein delivery to a single cell was achieved.<sup>52</sup> To broaden the application of the physical micromotor, our group previously developed a microhelix by two photon lithography toward assisted fertilization. The fineness of this helical motor was so

high that it could precisely swim to the specifically selected immotile sperm and capture it. When the sperm flagellum was confined in the inner part of the microhelix with the sperm head outside, the sperm was thus blocked on the microhelix and transported by it. This work can be an alternative method for in vivo artificial fertilization to avoid the oocytes explanting in the future.<sup>53</sup> However, the above mentioned micromotors controlled by the magnetic field always rely on efficient magnetic material and specific responsible structure, restricting the diversity of the micromotors. Considering this, researchers are also investigating the possibility to drive more different micromotors by other propulsion systems, such as electric field, sound field and light field. Certainly, none of them has to work independently. In the future, a more skilled micromotor with combined propulsion mechanisms can be envisioned to execute tasks in more complicated environments, such as blood and the cavities inside organs.

### (3) Biohybrid micromotors

Scientists combined the physical micromotors with the biological component initially for the purpose to enhance their adaptability to the human body or capacity for drug loading.<sup>54</sup> For example, Wu et al. encapsulated  $\text{Fe}_3\text{O}_4$  nanoparticles into red blood cells (RBCs). The fabricated RBC motors were able to be propelled by ultrasound fields and magnetically guided in the whole blood. RBC encapsulation largely enhanced the biocompatibility of the magnetic particles.<sup>55</sup> However, these RBC motors still need the power from the external ultrasound field which could be harmful to the other cell organisms in the human body. Some microorganisms owning migration abilities were developed to provide the propulsion of micromotors. For example, He et al. developed a hybrid neutrophil micromotor system which was guided along the chemoattractant gradients secreted by *Escherichia coli*.<sup>56</sup> DOX-HCl was successfully loaded and transported by this system. However, the maximum velocity of this motor was only  $0.17 \mu\text{m/s}$ . This represents the main problem of inactive motion in the use of these flagella-free organisms. Such low velocity brings practical difficulty for the guidance of these micromotors. The job can be even in vain if the motors were caught by the migrating immune cells or flushed away by the environmental fluid.

Self-propelled biological structures are intriguing for their ability to adapt and swim in complex environments at high speed thanks to their independent propelling systems. For instance, flagellated bacteria have been shown as efficient swimmers at the microscale.<sup>57</sup> A study of bacteria-driven micromotors demonstrated the transport of fluorescent beads. These bacteria exhibited a strong preference of swimming towards an L-serine gradient without significant speed change. Bacteria-driven motors can be also applied on the delivery of anticancer drugs. Taking advantage of the chemotaxis of *E. coli*, Park et al. refitted bacteria to be an active delivery system,<sup>58</sup> by coupling with polyelectrolyte multilayer microparticles embedded with magnetic nanoparticles. These motile bacteria could be efficiently guided targeting breast cancer cells under a chemoattractant gradient or a magnetic field, and release preloaded DOX-HCl into them, showing an enhanced DOX-HCl accumulation in the targeted cell compared to the immobile microparticles. Some special bacteria with connatural guidable system turn out to be more valuable on precise drug delivery. For example, the *Magnetococcus marinus* can load anticancer drugs with the help of liposomes and transfer to the desired targeted cancer tissue under the guidance of the magnetic and the chemical gradients.<sup>59</sup>

Despite the potential that bacteria showed on propelling micromotors, challenges are remaining regarding their use in human body. First comes the safety issue. Bacteria are one kind of the most infective exogenous organisms. They induce both acute and chronic inflammations due to the immunoreactions and the organs injury induced by the infection of bacteria. Besides, bacteria ordinarily have self-protection mechanisms, for example the endospore structure, to resist the elimination of the immune system and thus help them hide in tissue. After the hidden bacteria are triggered to recover by exponential proliferation, human body could suffer heavier damage.<sup>60</sup> Furthermore, any further import of bacteria will inevitably bring microbial flora imbalance, which will disorder the functions of the local organs or even the whole body.<sup>61</sup> In addition of the safety concern, the adaptability of bacteria in human body restricts their propulsion, since the body fluids are not suitable environment for their motion. The drug loading by bacteria also represents a problem, especially for those micromotors relying on the drug encapsulation by bacteria. As bacteria have active metabolism, payload drug is not safe, facing the degradation by the metabolic

system of the bacteria or the deactivating by secreted substances by the bacteria. Thereupon, a microorganism that is adapted in human body and can provide powerful propulsion is thus urgently needed. Among others, the sperm is one promising candidate.

### 2.3. Sperm-based micromotors

Sperms, as the male reproductive cells, are highly differentiated cells that are naturally optimized to efficiently swim in the female reproductive system. They are thus potential candidates for the treatment of cervical cancers and other gynecologic diseases. All mammalian sperm consist a head and a flagellum. The head contains densely coiled chromosome and very little amount of cytoplasm. On the anterior of the head covers acrosome that contains enzymes to penetrate the oocyte and induce fertilization.<sup>62</sup> The flagellum can be divided in two parts, the tail that can beat by its outer microtubule doublets, and the midpiece in which the mitochondria are located to provide the energy source (ATP) for the tail beating.<sup>63</sup> Hence, the propulsion is generated by the flagellum. Although the size and shape of sperm vary in different species, the cellular component and motion mechanism are conserved. We use bovine sperm as a model in this dissertation as they are good candidates to simulate human sperm with similar paddle-like shape and helical motion mode.<sup>64,65</sup> As illustrated in **Figure 2.7a**, the bovine sperm is about 60  $\mu\text{m}$  long including a 10  $\mu\text{m}$  long head and 50  $\mu\text{m}$  long flagellum. The head is about 5  $\mu\text{m}$  in width and 1  $\mu\text{m}$  in thickness. The sperm can swim in corkscrew-like helical motion thanks to the asymmetric bending and rolling of the flexible flagellum. The swimming speed of the sperm can be approximately 100  $\mu\text{m/s}$  with a propulsion force up to 128 pN,<sup>66</sup> enabling the sperm to be promising power supply for micromotors.<sup>67</sup>

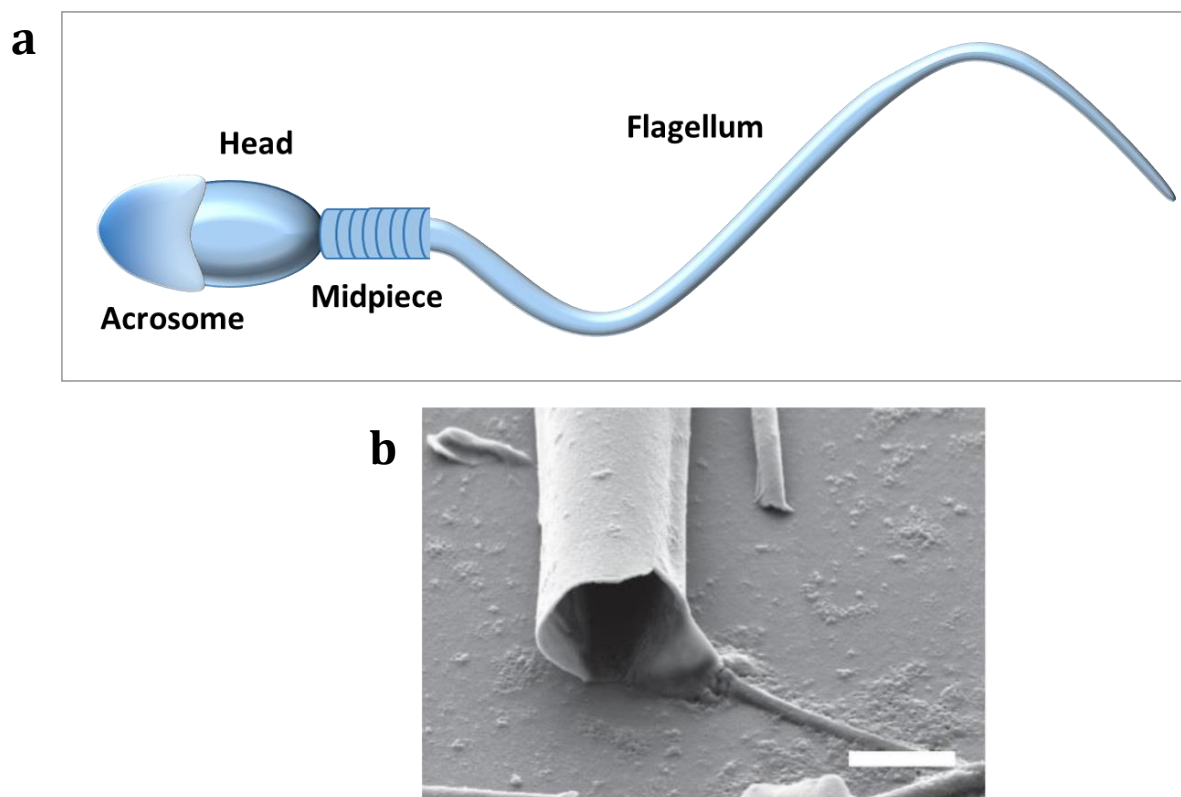


**Figure 2.7.** (a) Structure of a bovine sperm. (b) SEM of the tubular spermbot (scale bar: 5  $\mu\text{m}$ ).<sup>68</sup> Reproduced with permission from © 2016 WILEY-VCH Verlag GmbH & Co. KGaA, Weinheim.

Magdanz et al. fabricated the first sperm hybrid micromotor based on a rolled-up method in 2013.<sup>68</sup> The so-called spermbot comprises of a bovine sperm as propulsion mechanism and an artificial microtube as guidance mechanism (**Figure 2.7b**). The magnetic microtube was constructed by a nanolayer of Fe which was deposited on the patterned photoresist with a sacrificial layer by lithography. After the sacrificial layer was dissolved in water, the Fe layer was rolled-up into a conical tube by the tension force. The sperm was then able to be stuck in and propel it forward. This system showed its value on single sperm transport and its further potential on assisted fertilization toward oligospermia. The coupling efficiency of sperm and microtubes could be further increased with the help of a fibronectin coating or simply narrowing the tube.<sup>69</sup> To improve this system furthermore, they fabricated a PNIPAM microtube, a thermal-responsive polymer, to control the release of the sperm. They showed

that the sperm release could be triggered by increasing the temperature from 37 to 40 degree.<sup>70</sup>

Regarding the application on drug delivery, the sperm features unique properties advantageous over the other artificial or cellular carriers. First, the sperm has powerful propulsion force that facilitates a fast and efficient delivery. The propulsion of the sperm needs neither toxic fuels nor external power source that is harmful to body. It in fact does not need any fuel from the environment when all the energy is generated out of the stored fuel by its own mitochondria. The highly independent self-propulsion broadens its applicable environments. Second, the sperm provides a possibility to efficiently encapsulate hydrophilic drugs, which have high DNA-binding affinity<sup>71</sup> and thus can be stored in the crystalline nucleus of the sperm.<sup>72</sup> By doing so, the sperm membrane can protect drugs from body fluid dilution, immune-reactions and the degradation by enzymes. sperm can also efficiently avoid dose dumping, which is regarded as a major issue of micelle carriers, thanks to their compact membrane system.<sup>73</sup> Moreover, for microscale synthetic carriers such as microspheres, micro capsules, and drug-loaded micromotors<sup>74-76</sup> drug transfer is always a problematic issue due to the inefficient transmembrane transport between the carrier and the cell.<sup>77</sup> In contrast, sperm cells, with their somatic cell-fusion ability,<sup>78-80</sup> are expected to improve the drug transfer to the target cells as well as the drug availability, by directly delivering the drug into the targeted cell plasm through membrane-fusion events. Several proteins of the sperm membrane such as CD9 and integrins are involved in this process.<sup>78</sup> In the end, sperm do not proliferate or secrete any harmful substance, ensuring the safety of the hybrid micromotors in the in vivo use. All of these make the sperm an excellent choice to construct new biohybrid micromotors and thus make this sperm-motor to be a promising candidate for the next-generation active drug delivery system.

### 3. Materials and methods

#### 3.1. Fabrication of microstructures

The fabrication of the microstructures were done by a two-photon lithography technique (Nanoscribe). A console software naming Nanowrite was used to for the inner communication of the designed 3D file with the lithography machine. Its compiler can read 3D CAD files generated by, for example Solidworks or other 3D modeling softwares. However, a more efficient way is to code the laser path with specific functions and all the parameters manually, avoiding redundant exposure. The writing process can be all directed by the codes by guiding the laser to expose at certain locations with certain power for certain time. The work flow is as following: designing the purposed structure, coding the laser path with appropriate functions, optimizing the writing parameters, preparing photoresist and constructing the structure.<sup>21</sup> In this dissertation, we mainly introduce three different microstructures, the microtetrapod, the streamline-horned cap (SHC) and the helical microcourier (MC).

##### 3.1.1. Coding

The manufacturing codes were written by Describe. Galvo scanning mode was used to write the main parts of all three structures.

(1) The microtetrapod is assembled by two parts. A tubular body and four curved arms (as shown in **Figure 3.1**). The tubular body is formulated as:

$$x = 5.3\sin\theta$$

$$y = 5.3\cos\theta$$

$$z = h_1$$

$$\theta \in (0, 2\pi), h_1 \in (0, 15),$$

where  $(x, y, z)$  represents the positioning of the exposure spot,  $h_1$  represents the independent variable limited by the tube height and  $\theta$  represents the independent variable limited by the angle of the writing position in polar coordinates system. Here the laser power of exposure is 10 mW, the exposure time is 50 fs and the scan speed of the galvo is 80000  $\mu\text{m/s}$ .

The curved arm is formulated as:

$$x_1 = \left( 7.5 - \frac{h_2}{\tan\left(\arcsin\sqrt{\frac{h_2}{15}}\right)} \right) * \cos\left(\varphi - \frac{\pi}{6}\right)$$

$$x_2 = \left( 7.5 - \frac{h_2}{\tan\left(\arcsin\sqrt{\frac{h_2}{15}}\right)} \right) * \cos\left(\varphi + \frac{\pi}{6}\right)$$

$$y_1 = \left( 7.5 - \frac{h_2}{\tan\left(\arcsin\sqrt{\frac{h_2}{15}}\right)} \right) * \sin\left(\varphi - \frac{\pi}{6}\right)$$

$$y_2 = \left( 7.5 - \frac{h_2}{\tan\left(\arcsin\sqrt{\frac{h_2}{15}}\right)} \right) * \sin\left(\varphi + \frac{\pi}{6}\right)$$

$$z = h_2$$

$$\varphi = \left\{0, \frac{\pi}{2}, \pi, \frac{3\pi}{2}\right\}, h_2 \in (0, 14)$$

where  $(x, y, z) \{x \in (x_1, x_2), y \in (y_1, y_2)\}$  represents the positioning of the exposure spot,  $h_2$  represents the independent variable limited by the arm height and  $\varphi$  represents the



independent variable limited by the phase angle of each arm. Here the laser power of exposure is 9 mW, the exposure time is 50 fs and the scan speed of the galvo is 60000  $\mu\text{m/s}$ .

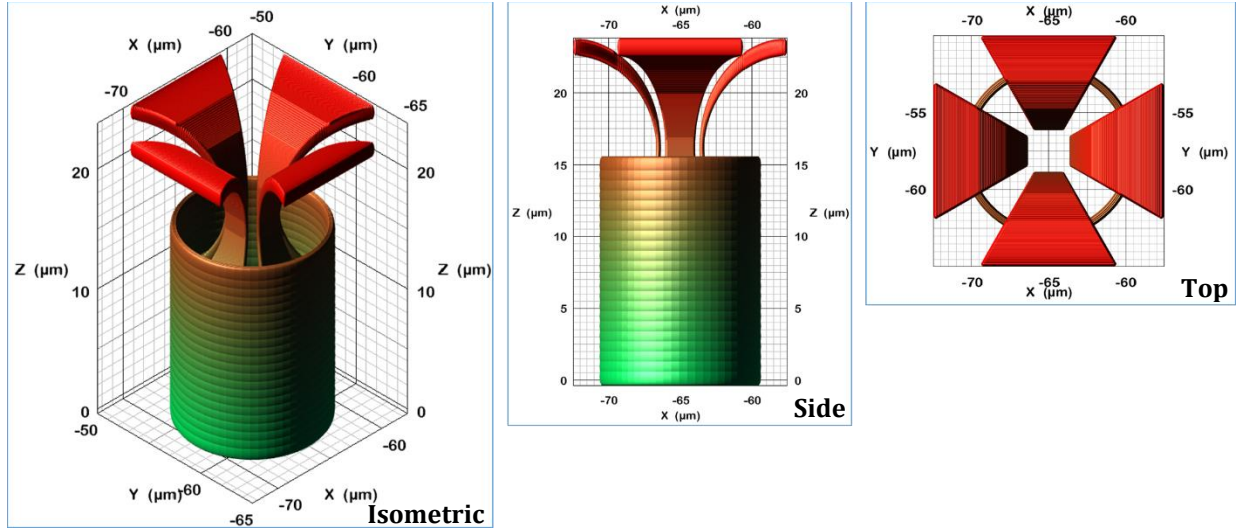


**Figure 3.1.** Design of the microtetrapod

(2) The SHC is assembled by two parts. An ellipsoid body and a tapered horn (as shown in **Figure 3.2**). The ellipsoid body is formulated as:

$$x = 6.5 \cos \theta * \sqrt{1 - \frac{h_1^2}{169}}$$

$$y = 6.5 \sin \theta * \sqrt{1 - \frac{h_1^2}{169}}$$

$$z = h_1$$

$$\theta \in (0, 2\pi), h_1 \in (0, 12),$$

where  $(x, y, z)$  represents the positioning of the exposure spot,  $h_1$  represents the independent variable limited by the tube height and  $\theta$  represents the independent variable limited by the angle of the writing position in polar coordinates system.

The tapered horn is formulated as:

$$x = \cos\varphi * \sqrt{1 - \frac{h_2}{3}}$$

$$y = \sin\varphi * \sqrt{1 - \frac{h_2}{3}}$$

$$z = h_2$$

$$\varphi \in (0, 2\pi), h_2 \in (0, 3),$$

where  $(x, y, z)$  represents the positioning of the exposure spot,  $h_2$  represents the independent variable limited by the horn height and  $\varphi$  represents the independent variable limited by the angle of the writing position in polar coordinates system. The laser power of exposure for the whole structure is 10 mW, the exposure time is 50 fs and the scan speed of the galvo is 60000  $\mu\text{m/s}$ .

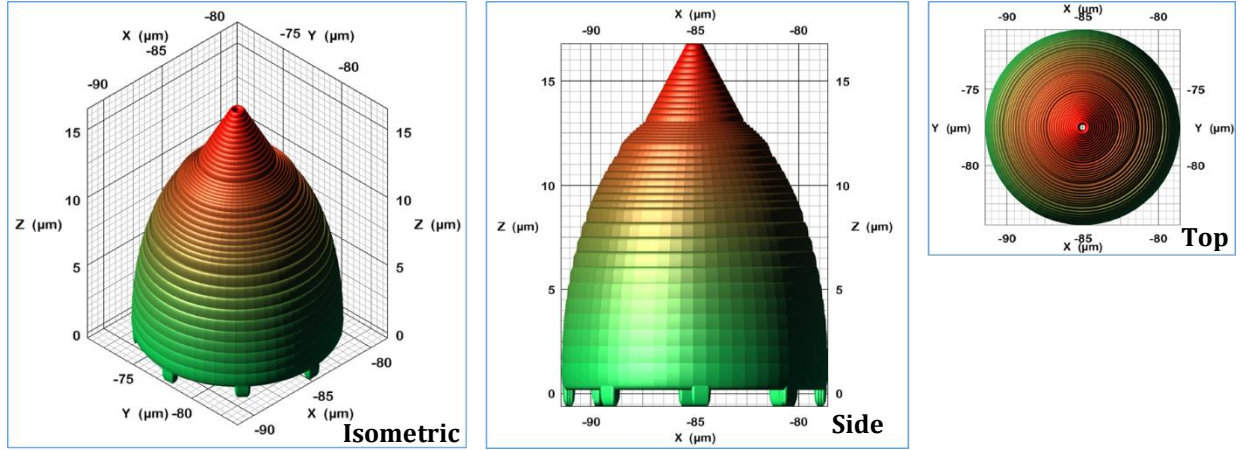


**Figure 3.2.** Design of the SHC.

(3) The MC is assembled by three parts. A tubular body, a cross frame and a helical tail (as shown in **Figure 3.3**). The tubular body is formulated as:

$$x = 40\sin\theta$$

$$y = 40\cos\theta$$

$$z = h_1$$

$$\theta \in (0, 2\pi), h_1 \in (0, 30),$$

where  $(x, y, z)$  represents the positioning of the exposure spot,  $h_1$  represents the independent variable limited by the tube height and  $\theta$  represents the independent variable limited by the angle of the writing position in polar coordinates system. Here the laser power of exposure is 10 mW, the exposure time is 50 fs and the scan speed of the galvo is 80000  $\mu\text{m/s}$ .

The cross frame is

$$x_1 = -20\sin\sigma$$

$$x_2 = 20\sin\sigma$$

$$y_1 = -20\cos\sigma$$

$$y_2 = 20\cos\sigma$$

$$z = 0$$

$$\sigma = \left\{0, \frac{\pi}{2}\right\},$$

where  $(x, y, z) \{x \in (x1, x2), y \in (y1, y2)\}$  represents the positioning of the exposure spot  $\sigma$  represents the independent variable limited by the angle of the writing position in polar coordinates system. Here the laser power of exposure is 12 mW, the exposure time is 50 fs and the scan speed of the galvo is 60000  $\mu\text{m/s}$ .

The helical tail is formulated as:

$$x_1 = 30\cos\left(\frac{h_2}{2\pi}\right)$$

$$x_2 = 30\cos\left(\frac{h_2}{2\pi} + 1\right) + 1.5$$

$$y_1 = 30\sin\left(\frac{h_2}{2\pi}\right)$$

$$y_2 = 30\sin\left(\frac{h_2}{2\pi} + 1\right) + 1.5$$

$$z = h_2$$

$$h_2 \in (0, 120),$$

where  $(x, y, z) \{x \in (x1, x2), y \in (y1, y2)\}$  represents the positioning of the exposure spot,  $h_2$  represents the independent variable limited by the tail. Here the laser power of exposure is 2 mW, the exposure time is 50 fs and the scan speed of the galvo is 80000  $\mu\text{m/s}$ .

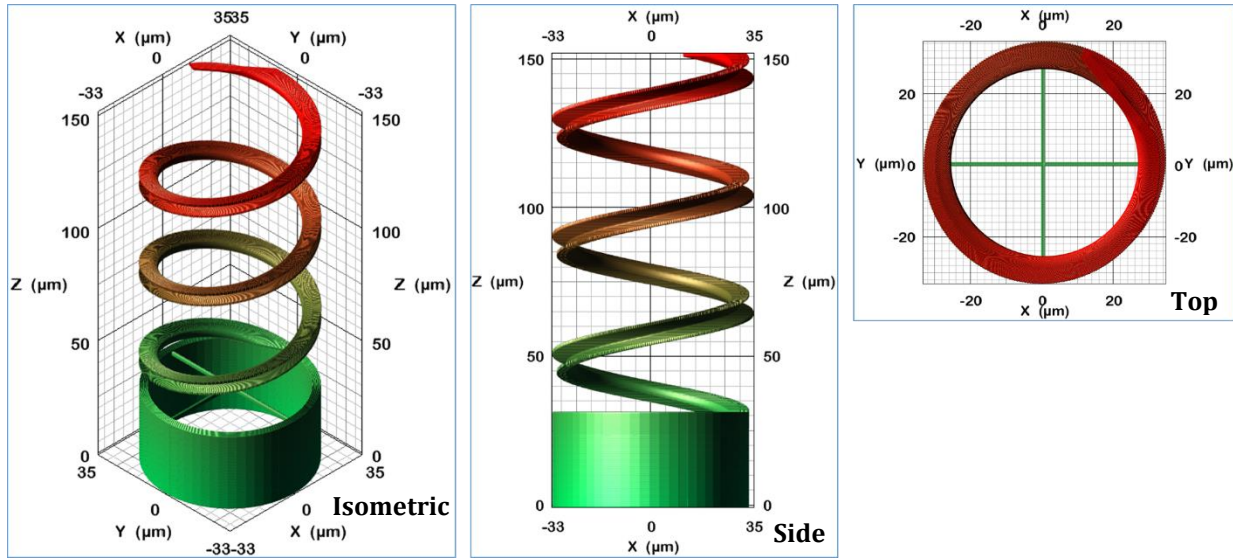


**Figure 3.3.** Design of the microcourier.

### 3.1.2. FSTL manufacturing

SiO<sub>2</sub> substrate were cleaned by nonpolar and polar organic solvents under ultrasound in sequence. Then the dried substrate was exposed to O<sub>2</sub> plasma for 1 min to enhance the wettability of the surface. Photoresist IP-DIP was dropped on the substrate and the objective was dipped into the photoresist. The interface between the substrate and the resist as the starting point of writing was detected with the signal amplitude at 50% and the exposure rate of the signal capturing by the autofocus camera at 70%. After writing, the sample was developed in propylene glycol methyl ether acetate (PEGMA) for 20 min and washed in isopropanol for 3 min to remove the residual IP-DIP. Finally, the sample was dried in a critical point dryer ((CPD, Autosamdri®-931, Tousimis Research Corporation) to avoid structure transformation by the tension force during drying.

### 3.1.3. Electron beam evaporation

Electron beam evaporation (E-beam), as a type of physical vapor deposition, is widely used to generate thin films at the nanoscale.<sup>81</sup> During the deposition process, an electron beam is

generated by an electron gun to bombard the target material. Atoms of the target can be transformed then into gaseous phase and re-precipitate on the substrate surface at a certain low rate, ranging from 0.1 to 10 Å/s. The deposition thickness is monitored by a quart crystal microbalance. The deposition rate can be then controlled by changing the heating current. The whole deposition is performed in a high vacuum chamber to avoid oxidation and any other chemical reactions. In this dissertation, an e-beam evaporator Edwards auto 500 e-beam (Moorfield Nanotechnology Limited) was used for the deposition. Ti, Fe, Au and SiO<sub>2</sub> of high purity (99.995 %) were used separately for different purposes. The heating voltage was set at 5 KV and the heating current was set at around 80, 70, 50 and 10 mA , separately for Ti, Fe, Au and Si<sub>2</sub>, inducing deposition rates at 3, 1, 1, 1 Å/s.

As an example of the fabrication of the artificial microstructures, **Figure 3.4** illustrates the whole process of the fabrication of microtetrapods.

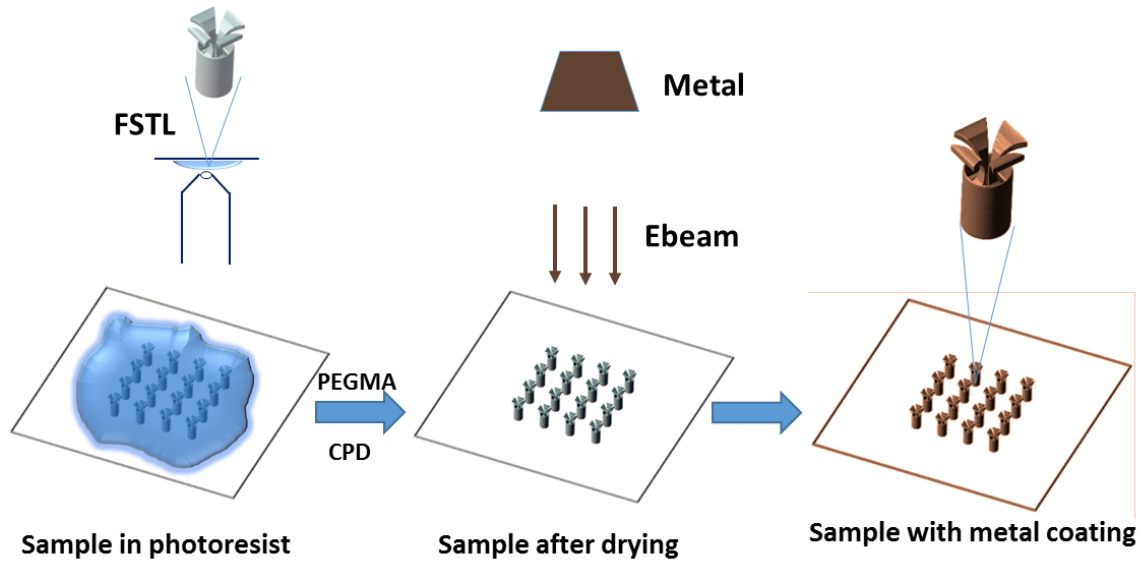


**Figure 3.4.** Fabrication of microtetrapods

### 3.2. Fabrication of microfluidic chips

Microfluidic chips are widely used in the study of micromotors to visualize the motion and precisely control the flow. In our research, polydimethylsiloxane (PDMS) microchannels were used to provide a confined space with clear visualization to monitor the swimming behavior of the micromotors, culture cancer cells at the microliter scale and control the flow rate. The fabrication was done by a molding method as exhibited in **Figure 3.5**. PDMS gel was plasticized on the mold to duplicate channels with the reversed shape. Finally, the channels were bound to clean glass or silicon wafers to obtain the microfluidic chips with channel thickness from 10 to 1000  $\mu\text{m}$ . The molds were manufactured based on a maskless lithography method on a negative photoresist. First, a layer of photoresist SU-8 2075 was spin-coated on a silicon wafer with specific thickness adjusted by the spin speed. After essential pre-bake to evaporate the solvent, the lithography was done by a direct laser writing machine (MLA), which applies a focused laser beam to selectively expose the desired area according to a 2D CAD design. The UV exposure decomposes the initiator and creates the active photoacid.<sup>82</sup> A direct post-bake was employed immediately after laser writing to induce the polymerization of the photoresist in the exposed area with photoacid. Then the sample was developed in acetone and baked again to enhance its stability.

PDMS prepolymer was prepared with the base and curing agent at a ratio of 10:1. After 30 min of degassing, the mixture was filled in the mold and baked at 75 °C for 3 hours. After that, the polymerized PDMS channel was peeled off and punched into corresponding inlets and outlets. Finally, the PDMS channel and a glass slide substrate were treated in O<sub>2</sub> plasma for 1 min and then bound together by a silicon oxygen bond<sup>83</sup> created at 90 °C for 20 min.

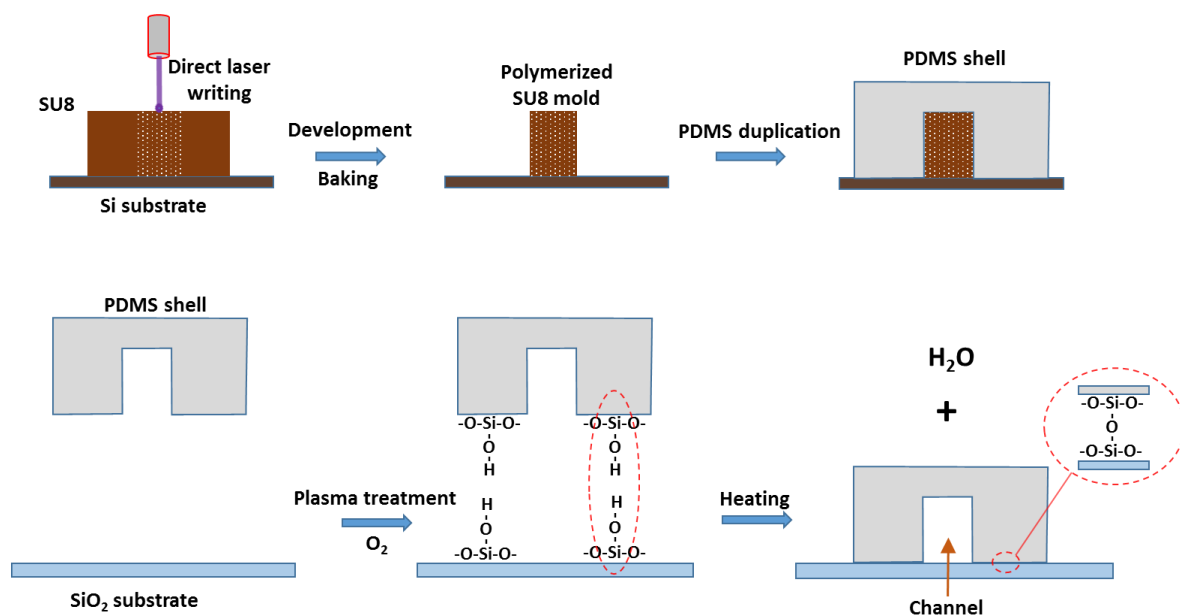


**Figure 3.5.** PDMS channel fabrication

### 3.3. Liposomes immobilization

Unilamellar liposomes were prepared by using a mini liposome extruder (Avanti). Briefly, 1,2-distearoyl-sn-glycero-3-phosphoethanolamine (DSPE) and cholesterol at a weight ratio of 4:1 were fully mixed and dried under the protection of nitrogen flow. After that, the mixture was dispersed in heparin sodium salt (Alfa Aesar) solution at a concentration of 50 mg/mL and extruded at 60 °C. The liposomes immobilization was accomplished by an improved method from the literature.<sup>59,84</sup> First, the microcaps were carboxylated by carboxyethylsilanetriol (abcr). And then they were incubated in the liposome solution with the presence of 1-Ethyl-3-(3-dimethylaminopropyl)carbodiimide) (EDC) / N-Hydroxysuccinimide (NHS) at 37°C. After that, the sample was washed by water for three times and dried in a critical point drier.



### 3.4. Drug loading in sperm

#### 3.4.1. Sperm preparation

##### (1) Preparation of bovine sperm samples:

Bovine sperm cells were recovered by thawing cryopreserved sperm straws rapidly in a water bath at 38 °C for 2 min, and washed with BoviPure 100 / BoviDilute (40%/ 80%) by centrifugation at 300g in soft mode for 5 min.<sup>85</sup> After the third centrifugation, 100 µL SP-TALP was gently added on the sperm pellet to induce a swim-up selection. After 40 min of incubation, the top liquid containing motile sperm was extracted out and diluted by SP-TALP to 1 mL for subsequent use.

##### (2) Preparation of human sperm samples

Human sperm samples were obtained from patients attending the Department of Reproductive Medicine, St Mary's Hospital, Manchester for routine fertility treatment, following written informed patient consent with approval from the Yorkshire & The Humber-Bradford Leeds Research Ethics Committee (18/YH/0130). Samples were washed with SPERM Rinse™ (Vitrolife) and suspended in G-IVF™ PLUS medium (Vitrolife). SPERMGRAD™ (Vitrolife) was used to separate progressively motile sperm out by density gradient centrifugation according to the G-Series Manual (Vitrolife). After purification, sperm samples were stored at room temperature for subsequent use.

#### 3.4.2. Drug loading process

**Figure 3.6** illustrates the loading process in sperm. In the following **Chapter 4** and **5**, DOX-HCl is used as a model drug to evaluate the encapsulation performance of sperm cells. DOX-HCl is a widely approved chemotherapeutic medication with a broad application spectrum in cancer therapy since 1974.<sup>86</sup> Its liposomal form (Doxil) is also used primarily for gynecologic cancer treatment.<sup>87</sup> Fluorescein isothiocyanate conjugated bovine serum albumin (FITC-BSA) is used as a non-toxic control model. Briefly, 1 mg/mL of FITC-BSA (Sigma-Aldrich, Germany) and DOX-HCl (Sigma-Aldrich, Germany) solution were prepared

in SP-TALP, respectively, and stored under dark conditions at 4 °C as stock solutions. To prepare DOX/BSA-loaded sperm cells, a mixture of sperm solution and FITC-BSA or DOX-HCl solution at specific concentrations were co-incubated in a humidified atmosphere of 5% CO<sub>2</sub> in air at 37 °C for 1 h. After washing the sample 2 times with SP-TALP by centrifugation at 300 g for 5 min, the pellet of drug-loaded sperm was redispersed in SP-TALP with progesterone (20 ng/mL) and stored in the incubator under dark conditions for subsequent use. It is important to note that the samples were to be used within 4 h to guarantee sperm motility.

For the DOX-HCl loading in human sperm, the incubation was done at room temperature for 40 min.

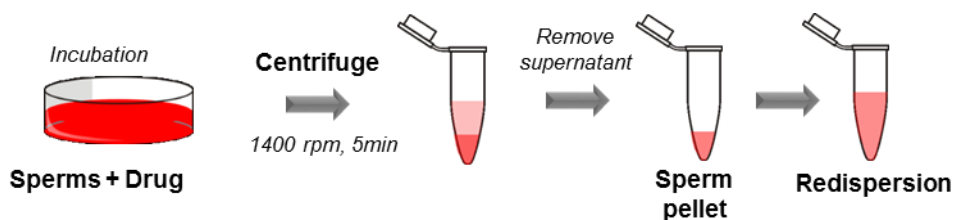


**Figure 3.6.** DOX-HCl loading in sperm

### 3.4.3. Evaluation of the drug loading efficiency

The success of the drug loading procedure was evaluated by the determination of the encapsulation efficiency. DOX-HCl-loaded sperm were prepared as mentioned before with a concentration of  $3 \times 10^6$  sperm per mL. The samples of DOX-HCl solution were designed as a series of concentrations with 10, 20, 50, 100 and 200 µg/mL. FITC-BSA-loaded sperm were prepared with FITC-BSA solution with a concentration of 100 µg/mL. After incubation of sperm in these solutions, the respective supernatant was collected after centrifugation and filtered through a 2 µm pore size membrane. The sperm were resuspended after purification as mentioned before. Fluorescence images were taken at an excitation wavelength of 470 nm (DOX-HCl: Ex 470 nm, Em 580 nm;<sup>88</sup> FITC-BSA: Ex 470 nm. Em 509 nm<sup>89</sup>) (Cell Observer, Carl Zeiss Microscopy GmbH).

(1) Indirect method for bovine sperm evaluation

In this method, the concentration of DOX-HCl was determined with a fluorescence spectrometer in FL-RL mode (SpectraMax® M2, Molecular Devices, LLC.). SP-TALP solution was used as blank control for all measurements. The concentration of the residual DOX-HCl was determined by measuring the supernatant of each sample after centrifugation.<sup>90</sup> The encapsulation efficiency was calculated as the ratio of encapsulated drug to the total amount of the used drug:

$$DOX \text{ loading ratio} = \frac{\text{total weight of the used DOX} - \text{weight of residual DOX}}{\text{total weight of the used drug}}$$

$$DOX \text{ amount per sperm} = \frac{\text{total loading amount}}{\text{number of used sperms}}$$

The drug loading amount was determined by the difference between the initial amount of DOX-HCl before incubation and the residual amount in the supernatant after co-incubation, which were both quantified by their respective fluorescence signals.

(2) Direct method for human sperm evaluation

In this method, amount of the encapsulated DOX-HCl was directly determined by lysing the sperm. DOX-HCl loaded human sperm were lysed for 30 mins in Triton-X 100 (20%). The mixture was then incubated in acidified isopropanol (0.75 N HCl) at 4 °C over night. After that, the samples were centrifuged at 12000g for 10 minutes and the released DOX-HCl in the supernatant was determined with a fluorescence spectrometer as mentioned before while the acidified isopropanol with sperm lysate as blank control.<sup>91</sup> DOX-HCl solution was dissolved in acidified isopropanol with sperm lysate to depict standard curve. The encapsulation efficiency was calculated as:

$$DOX \text{ loading ratio} = \frac{\text{weight of loaded drug}}{\text{total weight of the used drug}}$$

$$DOX \text{ amount per sperm} = \frac{\text{total loading amount}}{\text{number of used sperms}}$$

#### 3.4.4. Evaluation of encapsulation stability

The encapsulation stability test was carried out by calculating the accumulative release ratio of DOX-HCl from sperm into SP-TALP. Drug-loaded sperm were incubated in SP-TALP in a dark place under humidified atmosphere, 5% CO<sub>2</sub> and 37°C. At each time point, the samples were centrifuged and 0.5 ml of supernatant was collected and replaced with 0.5 ml of SP-TALP. After 96 hours, the samples were treated with ethylene diamine tetraacetic acid (EDTA)-Trypsin for 3 mins to release all drug into the solution. Fluorescence spectroscopy was used to quantify the DOX-HCl concentration of the supernatant. The accumulative release ratio was calculated as the ratio of the accumulated amount of the drug to the total amount of it. SP-TALP was used as blank control.

#### 3.4.5. Evaluation of the sperm viability after drug loading

DOX-HCl-loaded sperm were prepared as mentioned before by incubating sperm ( $8 \times 10^5$  sperm in 1 mL) with DOX-HCl at a concentration of 100 µg/mL. After purification, sperm were incubated in a humidified atmosphere of 5% CO<sub>2</sub> in air at 37 °C. After specific time periods, drug-loaded sperm were analyzed by fluorescence microscopy (Cell Observer, Carl Zeiss Microscopy GmbH), using a commercial LIVE/DEAD Viability Kit (ThermoFisher). Briefly, sperm solution ( $10^6$  sperm) were incubated with 5 µL of diluted Component A (SYBR 14, 10%) for 10 min and 5 µL of Component B (propidium iodide) for 5 min, respectively. After washing, sperm analysis was performed at an excitation wavelength of 470 nm to visualize the live sperm.

#### 3.4.6. Evaluation of the motility of DOX-HCl-loaded sperm

DOX-HCl-loaded sperm were prepared as mentioned before. Unloaded sperm were treated with the same method as the control sample. After purification, sperm were incubated in SP-TALP in a humidified atmosphere of 5% CO<sub>2</sub> in air at 37 °C. At certain time points along 36 h, 100 µL of sperm ( $10^4$  per each sample) was extracted from the Petri dish and added into the counting chamber to study the motility. For that, a computer-assisted sperm analysis

(CASA) system (AndroVision®, Minitube GmbH) was employed. 10 fields (*ca.* 500 sperm) of each sample were counted at each time point.

### 3.5. Cancer cell culture

#### 3.5.1. Culture of HeLa cells and spheroids

HeLa cells were cultured at 37°C in a humidified atmosphere containing 5% CO<sub>2</sub> in Dulbecco's modified Eagle's medium (DMEM) supplemented with 10% (v/v) fetal bovine serum (FBS), 100 U/mL penicillin, and 100 µg/mL streptomycin.<sup>92</sup> For spheroids culture, HeLa cells were recovered and maintained for 2 weeks before use. To prepare spheroids with homogeneous sizes, equal amounts of HeLa cells ( $2 \times 10^5$  cells resuspended in 4 mL) were added to 3.5-cm cell-repellent dishes (Greiner bio-one) after trypsinization and PBS washing. After two days of maturation, spheroids were separated in different groups and incubated with related treatments.

#### 3.5.2. HGSOC-representative ex vivo tumour cell culture and spheroids

OCMI66 cells were provided by Stephen Taylor. In brief, from ascites, red blood cells were lysed, the remaining cellular fraction harvested by centrifugation, and the cells maintained in OCMI media<sup>93</sup> in 5% O<sub>2</sub> and 5% CO<sub>2</sub> at 37°C in a humidified atmosphere. Serial passaging and selective detachment was used to eliminate white blood cells and separate tumour fractions from stromal cells. Experiments were performed at early passage numbers (p20s). The OCMI66 culture has been previously characterised including drug sensitivities (Nelson et al., has been submitted). The project is covered by an MCRC Biobank license held by Stephen Taylor (16\_STTA\_01). OCMI66 spheroids were prepared as for HeLa cells (see above).

#### 3.5.3. Evaluation of antitumor efficacy of DOX-HCl loaded sperm

DOX-HCl-loaded sperm were prepared as mentioned before by incubating blank sperm ( $8 \times 10^5$  sperm in 1 mL) with DOX-HCl at a concentration of 100  $\mu\text{g/mL}$ . After purification, 100  $\mu\text{L}$  of sperm solution ( $8 \times 10^4$  sperm) was added into HeLa spheroids suspension (4 mL) and co-incubated in a humidified atmosphere of 5%  $\text{CO}_2$  in air at 37 °C. Spheroid control was prepared by adding 100  $\mu\text{L}$  of SP-TALP while blank sperm control was prepared by adding 100  $\mu\text{L}$  of blank sperm solution ( $8 \times 10^4$  sperm). DOX-HCl solution control was prepared by incubating HeLa spheroids with 100  $\mu\text{L}$  of DOX-HCl solution at a concentration of 15  $\mu\text{g/mL}$ . The LIVE/DEAD Viability Kit (ThermoFisher) was employed to stain cells and analyze the cell viability. Briefly, HeLa spheroids were washed and digested by trypsin-EDTA to a single-cell suspension at certain time points. After that, cells were incubated with 1  $\mu\text{L}$  of Component A (SYBR 14) for 10 mins and 5  $\mu\text{L}$  of Component B (propidium iodide) for 5 mins, respectively. Cell counting was performed under excitation at the wavelength of 470 nm for live cells and 540 nm for dead cells (4 samples for each group,  $10^4$  cells for each sample) (Cell Observer, Carl Zeiss Microscopy GmbH).

## 4. Tetrapod-like sperm-motor for targeted drug delivery

This chapter is based on the publication titled: Sperm-hybrid micromotor for targeted drug delivery. Reprinted with permission from [ACS Nano 2018, 12, 1, 327–337] ([doi/10.1021/acsnano.7b06398](https://doi.org/10.1021/acsnano.7b06398)). Copyright [2018] American Chemical Society.

### 4.1. Background

The development of drug delivery systems that provide effective doses locally in a controlled way is one of the main goals in the worldwide fight against cancer.<sup>94,95</sup> The current challenges include the unspecific uptake by other organs,<sup>6</sup> limited tissue penetration<sup>8</sup> and the decrease of effective concentration due to the dilution in body fluids.<sup>7</sup> Among the most promising nano- and microcarriers approaches to overcome such hurdles are cellular drug delivery systems, where a cell or microorganism acts as drug carrier, as they have advantages like cell membrane fluidity, ability to interact with other cells/tissue, long lifespan and high biocompatibility.<sup>96</sup> Stem cells, for example, have been used as a combinatorial drug delivery system towards regenerative therapy.<sup>97</sup> Macrophages and red blood cells with and without synthetic guidance or propulsion components have also been suggested as carriers for cancer therapy<sup>98</sup> and sustained drug release in blood,<sup>99</sup> respectively. Likewise, self-propelled cells, as a combination of cellular encapsulation and propulsion, have interested scientists all over the world due to their swimming performance in complex physiological microenvironments.<sup>68,100</sup> For example, magneto-aerotactic bacteria were reported to deliver drug-loaded liposomes to the hypoxic regions of tumor tissue in mice.<sup>59</sup> Bacteria, with chemotactic<sup>101</sup> properties and/or with associated synthetic guidance components,<sup>102–104</sup> can transport and deliver drugs into tumor tissue, showing great potential as self-propelled drug delivery carriers. Nonetheless, it is noteworthy that rapid clearance or even autoimmune reactions might be caused by the immune response to certain bacteria.<sup>105</sup>

Compared to other cellular drug carriers, sperm are promising candidates for the treatment of gynecologic diseases due to their environmental adaptability, their encapsulation and protection ability to drug and their somatic cell-fusion ability, as summarized in **Section 2.3**. Previous research demonstrated the use of sperm as carriers of nanoparticles<sup>106</sup> and lipid vesicles<sup>107</sup> on the sperm membrane for protein localization and potential biomacromolecule transport, respectively. In this chapter, we present a tetrapod-like sperm-motor for targeted drug delivery. This system comprises a motile sperm cell as the propulsion source and drug carrier, and the microtetrapod featuring four arms which release the sperm cell *in situ* when they are bent upon pushing against a tumor spheroid. Providing controllable guiding and release mechanisms, the tetrapod-like sperm-motor can potentially deliver drug to tumor cells and furthermore avoid undesired drug accumulation in healthy tissue. This system combines several intriguing features, namely high drug loading capacity, self-propulsion, *in situ* mechanical trigger release of the drug-loaded sperm, sperm penetration ability and improved drug availability.

## 4.2. Drug loading in sperm

In this chapter, DOX, as a model drug, was loaded in bovine sperm by co-incubation of DOX-HCl and live sperm, as described in **Section 3.4.2**. After purification, the incubated sperm sample was redispersed in the sperm medium. The drug-loading of sperm was evaluated by fluorescence microscopy as shown in **Figure 4.1a**, as DOX-HCl exhibits self-fluorescence at 470 nm excitation wavelength. It was calculated that 98% of the sperm cells (*ca.* 3500 sperm cells) were loaded with DOX-HCl. DOX-HCl was predominately found in the head of sperm as can be seen in **Figure 4.1a(ii)**. A 3D reconstructed image, obtained from overlaid z-stack images of a single sperm cell is shown in **Figure 4.1a(iii)**, indicating that DOX-HCl was mainly loaded inside the sperm head. This can be attributed to the drug adsorption on the condensed chromosomes by binding to proteasomes<sup>108</sup> and the drug dispersion in the cytoplasm that remains in the head of the sperm after maturation.<sup>63,106</sup> As a complementary experiment, we loaded sperm with Fluorescein isothiocyanate labelled bovine serum



albumin (FITC-BSA), a model for protein drugs as an alternative control. In this case, sperm behaved differently from the loading of DOX-HCl. FITC-BSA accumulation occurred all over the sperm, including head, midpiece and tail (**Figure 4.1b**).

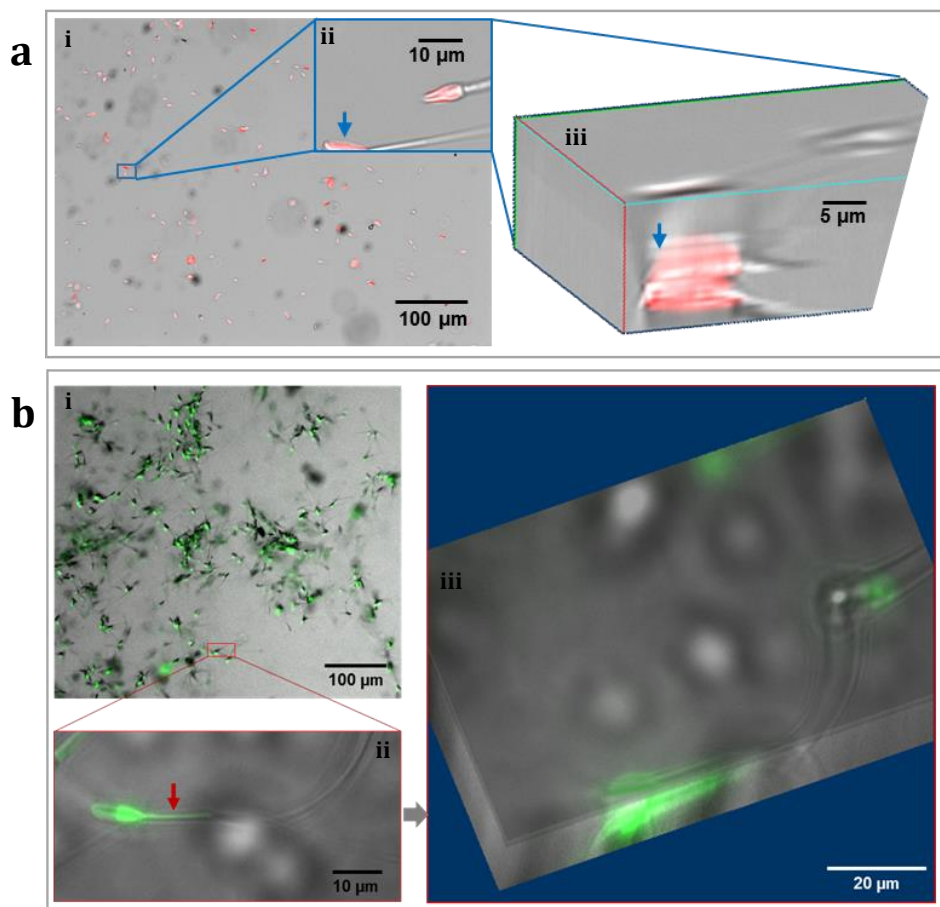


**Figure 4.1.** sperm loaded with (a) DOX-HCl; (b) FITC-BSA. (i), (ii), (iii) represent 10×, 40× and 3D reconstruction of z-stack images.

The loading efficiency was measured by fluorescence spectrometry, as described in the 3.4.3. The encapsulation efficiency was calculated as the ratio of encapsulated drug to the total amount of the used drug. The drug loading amount was determined by the difference between the initial amount of DOX-HCl before incubation and the residual amount in the supernatant after co-incubation, which were both quantified by their respective

fluorescence signals. **Figure 4.2** depicts the drug loading profiles related to DOX-HCl concentration. In the solution with a concentration of  $3 \times 10^6$  sperm per mL, the loading amount of DOX-HCl increased approximatively linearly with the concentration of DOX-HCl ranging from 10 to 200  $\mu\text{g/mL}$ . Hence, the loading ratio remains at around 15% for all concentrations. For the maximum concentration of DOX-HCl in our experiments, the loading amount was up to 37  $\mu\text{g}$  in 500  $\mu\text{L}$  sperm solution. This amount indicates an average encapsulation of 15 pg of DOX-HCl per single sperm cell.

The result of the drug loading ratio calculation highlights the high encapsulation capacity of sperm cells. Previously, Munerati et al reported successful loading of DOX-HCl into macrophages. Similar to our results, DOX-HCl was found inside the cell (2.5 pg per cell), particularly in the nucleus, with a higher concentration compared to the residual DOX-HCl solution in the culture medium (cell size roughly 15-20  $\mu\text{m}$ ). To explain this loading profile, the authors referred to the adenosine triphosphate (ATP)-mediated permeabilization of cells as a possible encapsulation mechanism.<sup>109</sup> In our research, DOX-HCl was used because cells also exhibit improved uptake of ionic DOX-HCl<sup>110</sup> compared to molecular DOX, which is normally taken in by facilitated diffusion.<sup>86</sup> This could allow the use of high local doses of anticancer drugs while reducing systemic toxic effects. Further research is required to investigate in detail the transport mechanism through the sperm membrane.

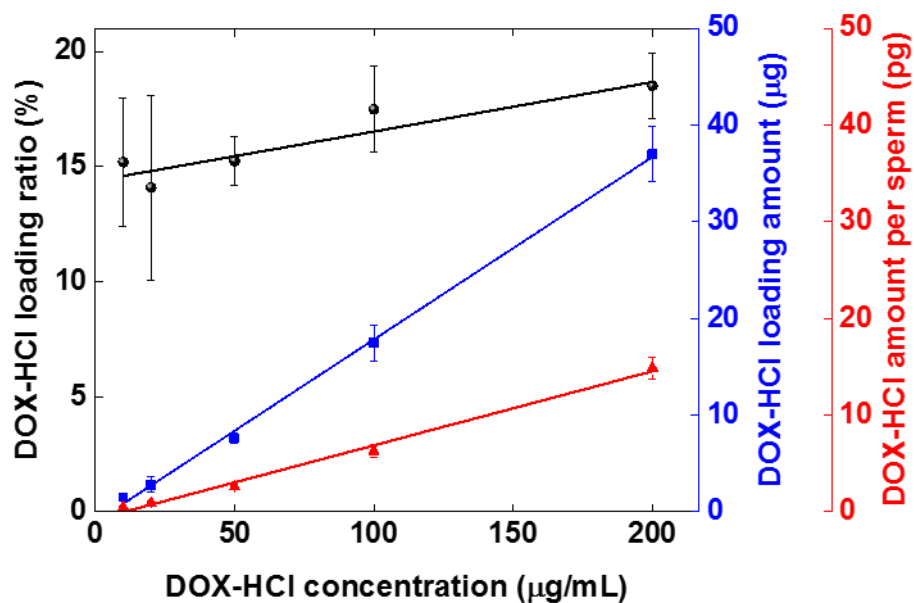


**Figure 4.2.** Encapsulation efficiency of DOX-HCl in sperm.

In order to analyze the influence of DOX-HCl on sperm, two complementary tests were performed. First, the viability of DOX-HCl-loaded sperm was analyzed using a commercial LIVE/DEAD kit. No significant difference was observed compared to unloaded sperm as more than 30% of sperm were still alive in both cases after 4 hours of culture in SP-TALP. As a more direct study to determine the most apt sperm for the intended goal of drug delivery, sperm motility test was suggested, as it not only provided information about sperm viability but also about their ability to transport the drug. **Figure 4.3a** shows the motility change of sperm after the loading process of DOX-HCl at 100  $\mu\text{g/mL}$ . A control sample with unloaded sperm was incubated in SP-TALP without drug under the same incubation and purification conditions. Motilities of both sperm samples decreased over time similarly. In the first 4 h, the percentage of motile sperm decreased from *ca.* 56% to 36%, which is however still sufficient enough to couple with the micromotors for the subsequent experiments. After 8 h of incubation, *ca.* 25% of sperm were still motile in both groups. Thus, we suggest to perform the drug-delivery experiment within 8 h after the drug-loaded sperm are prepared, which is

sufficient to reach any organ from the reproductive system (the maximum traveling distance is about 144 cm, considering an average velocity of the sperm-hybrid micromotor of 50  $\mu\text{m/s}$ ). Thus, the influence of DOX-HCl on sperm viability is not significant. This can be explained by the fact that DOX-HCl kills cancer cells by interfering with their macromolecular biosynthesis.<sup>111</sup> Unlike cancer cells, mature sperm have terminated most of their macromolecular synthesis due to the lack of a complete endomembrane system.<sup>112</sup> The propelling power is all generated in the mitochondria in the sperm's midpiece.<sup>63</sup> Therefore, taking account of the observation that the velocity significantly decreased when the DOX-HCl concentration was higher than 100  $\mu\text{g/ml}$  (probably due to the membrane destruction by the high osmotic pressure), we used a concentration of 100  $\mu\text{g/mL}$  DOX-HCl to load the sperm for the subsequent experiments. Another advantage of sperm comes from their incomplete metabolic system,<sup>112</sup> as sperm can protect a contained drug within its lipid bilayer like a liposome, but does not metabolize it like stem cells or other somatic cells would do. We also carried out a test on the encapsulation stability. The results show that less than 10% of drug was leaked into the medium after 8 h (**Figure 4.3b**). This means that the DOX-HCl encapsulation by sperm is sufficiently stable for subsequent drug delivery experiments.

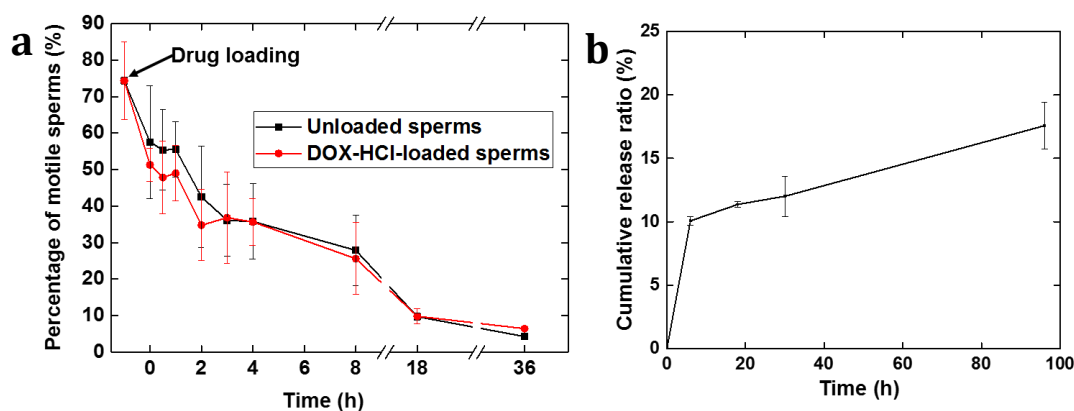


**Figure 4.3.** (a) Sperm motility after drug loading. (b) Stability of DOX-HCl loading in sperm.

### 4.3. Sperm-motor transport

The microtetrapods were fabricated in an array with 14400 structures on a substrate at  $2 \times 2$  cm<sup>2</sup>. The dimensions of the microstructure are shown in **Figure 4.4a**. At the narrowest point between the four arms, the maximum distance is 4.3  $\mu$ m. In preliminary experiments, the dimensions of the structure were optimized according to the dimensions of the sperm cell (for the experiments shown in this chapter, bovine sperm cells were selected for their paddle-like shape similar to human sperm), of which the head is on average 4.5  $\mu$ m wide, 1  $\mu$ m thick and 10  $\mu$ m long (**Figure 4.4b**). **Figure 4.4c** shows the finite element simulation validating the bending capability of the microtetrapod geometry. By calculation, when a force of about 128 pN (average sperm force obtained from literature)<sup>66</sup> was applied to one of the arms, the resulting displacement was 116 nm, which was enough to release the sperm. The displacement would increase up to 407 nm when the applied force is 450 pN, which could be generated by a hyperactivated sperm (which exhibits higher tail amplitude and asymmetric beating pattern).<sup>66</sup>

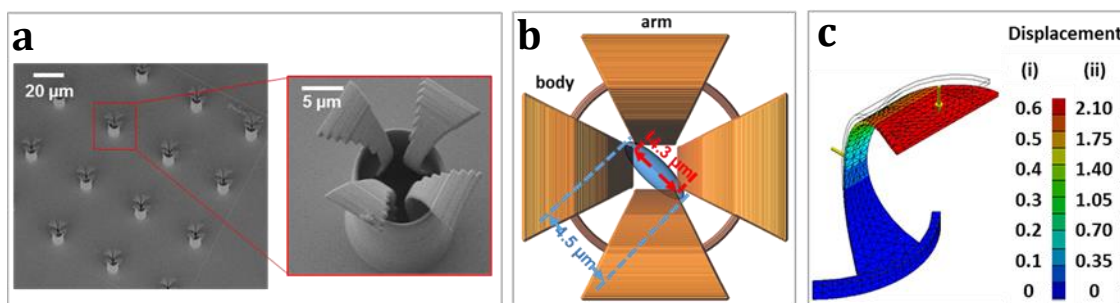


**Figure 4.4.** Geometry of the microtetrapod. (a) SEM images. (b) Top view of the microtetrapod with schematic sperm head inside. (c) Finite element analysis results demonstrating the deformation of one single arm. Yellow arrows represent the applied forces. (i) 128 pN from a motile, non-hyperactivated sperm, and (ii) 450pN from a hyperactivated sperm.

When a sperm reaches a tetrapod, it gets mechanically trapped inside the cavity of the tubular part and starts to push the microtetrapod forward. The tubular body of the microtetrapod is only 2  $\mu\text{m}$  longer than the sperm head, thus the sperm tail can still beat freely outside the tube to provide powerful propulsion.<sup>69</sup> Compared to free sperm, the average swimming velocity of the sperm-hybrid motors is nonetheless decreased by 43% from  $73 \pm 16 \mu\text{m/s}$  to  $41 \pm 10 \mu\text{m/s}$  (average of 15 samples of sperm-hybrid motors). All measurements were performed in SP-TALP at room temperature. Despite the variability among different sperm samples, the main reason for the velocity reduction is thought to be the increase of the fluid drag that is provoked by the synthetic material and the complex structure of the tetrapod. The asymmetrically distributed metal coating makes it possible to guide the microtetrapod or the tetrapod-like sperm-motor. **Figure 4.5a** illustrates a rectangular track of a guided sperm-hybrid motor. The hybrid motor was easily steered by changing the direction of the external magnet. After coupling to a tetrapod, the sperm still rotated when the hybrid motor moves forward due to the helical motion of the sperm,<sup>113</sup> which means the microtetrapod did not change the characteristic motion of the coupled sperm. The vertical guidance of a sperm-tetrapod is shown also in **Figure 4.5b**. The sperm-hybrid motor was steered to swim vertically out of plane simply by tilting the external magnet vertically. Before starting the experiments with sperm cells, tetrapods were always treated with Pluronic® F-127 solution to reduce undesired adhesion<sup>114</sup> between the sperm membrane and the microtetrapod surface.

PDMS microfluidic channels were fabricated as a platform for the investigation of the sperm release mechanism. **Figure 4.5c** shows the sperm escape when the sperm-motor hit a wall. The majority of tetrapods was found to rotate together with captured sperm due to either surface interaction between the sperm membrane and the material surface or the mechanical locking of the sperm head inside the structure. In these cases, it always took several seconds from the moment when the microtetrapod hit a wall until complete release of the contained sperm, which we found beneficial to release the sperm specifically when the sperm reaches the intended target and hits it for a while. Sperm release occurred in both cases when two arms hit a corner or when four arms hit a wall, while the release processes were different. When the motors came into contact with the targeted barriers, they still

rotated for a while after the forward swimming was stopped. As shown in **Figure 4.5c**, the sperm-tetrapod rotation stopped faster when two arms hit a corner because of the geometric gap between the arms which was easily caught on a corner. Once the rotation stopped, the sperm cell escaped when the microtetrapod arms opened (release in around 7 s). When four arms hit a wall, the rotation was not stopped because the arms were not locked. Thus, the sperm release took longer when four arms were bent on a wall (around 12 s). In both cases, tetrapods were pushed back by around 3  $\mu\text{m}$  after the sperm escaped. The reason for this recoil is the microtetrapod arm's elasticity that makes them recover their original shape once the pushing sperm is gone and thus generate a spring force opposite to the initial pushing direction. Even though there is a substantial diversity in bovine sperm dimensions, swimming behaviors and fabricated tetrapods within a sample, more than 2/3 (15 out of 22) of the coupled motors were shown to have successfully released sperm cells.

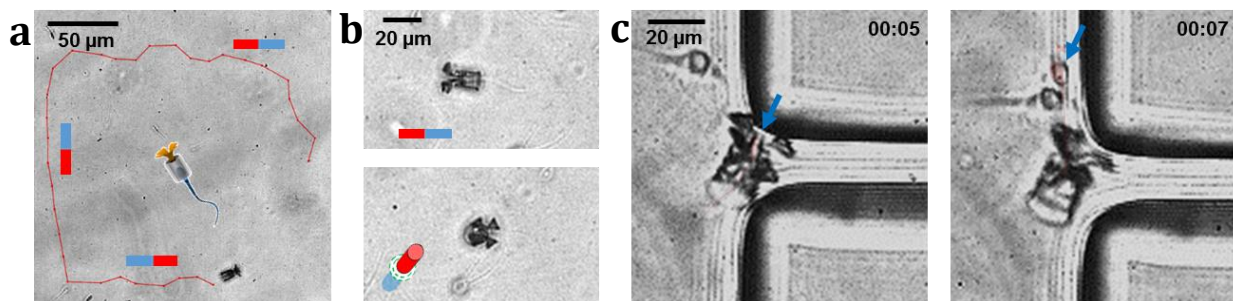


**Figure 4.5.** Track (red line) of a sperm-hybrid motor under magnetic guidance in the (a) horizontal plane and (b) vertical plane. (c) Image sequence of a sperm release process when the arms hit the corner of a PDMS wall. Blue arrows point at the sperm head. Time lapse in min:s.

The mechanically triggered release performance relies on the elasticity of the microtetrapod arms and the sperm force. It has been demonstrated that the type of monomer and the cross-linking parameters contribute to the elasticity of photosensitive polymeric materials.<sup>14</sup> Thus,

in order to avoid accidental release events, we did not choose a softer polymer material but optimized the laser power that initialized cross-linking instead. In our simulation, the applied force was given according to the maximum pushing force of a sperm in low-viscosity fluid ( $2.29 \cdot 10^{-3} \text{ Pa}\cdot\text{s}$ ).<sup>115</sup> In addition, the sperm can generate a more powerful force when the head is pushing against an obstacle, as has been reported elsewhere.<sup>116</sup> Moreover, the sperm force can be up to 20 times higher when the sperm is hyperactivated and swims in the viscoelastic fluid of the female reproductive system.<sup>66</sup> All these parameters should be considered for future applications in vivo.

## 4.4. Cancer treatment

### 4.4.1. Antitumor efficacy of drug loaded sperm.

HeLa cells, as derived from cervical cancer cells, were cultured into spheroids as 3D tumor model to evaluate the influence of drug-loaded sperm on cell death (see details in **Section 3.4**).<sup>92</sup> In order to visualize the drug distribution into the tumor spheroid with no damage on it, we first employed FITC-BSA as a proof of concept for protein-based drugs (**Figure 4.6**). We observed that after 24 hours co-incubation of BSA-loaded sperm with spheroids, sperm were found not only in the solution, but also in the spheroids as shown in the overlaid z-stack images, demonstrating the tissue penetration capability of sperm. According to a semi-quantitative analysis by using ImageJ, the integrated fluorescence intensity which represents the total amount of BSA, increased 1.8 times compared to the amount at the beginning of the experiment. The observed spreading area of FITC-BSA increased 7.4 times. This indicates that the increase of the fluorescent area was not only because more sperm swam into the spheroid over time, but also because more FITC-BSA was transferred from sperm into the HeLa spheroid. Here no further studies were performed, as in this work we focused on the study of the antitumor efficacy of DOX-HCl loaded sperm.



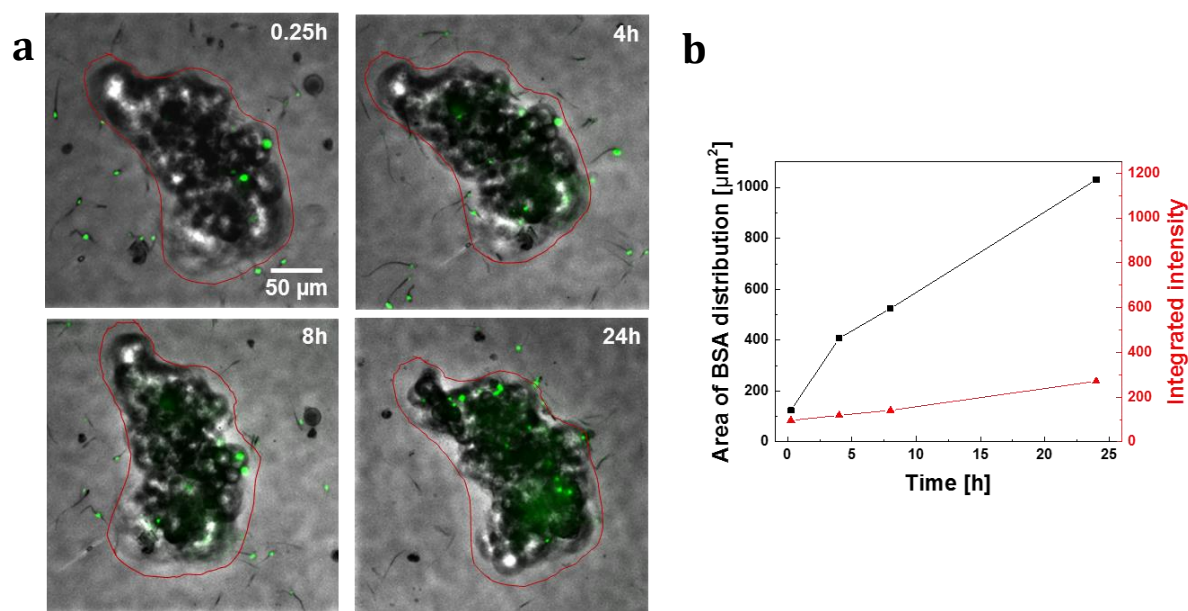


**Figure 4.6.** FITC-BSA distribution in a HeLa spheroid after the co-incubation of FITC-BSA loaded sperm with a HeLa spheroid. (a) Overlaid z-stack images. Red lines circle the spheroid. FITC-BSA is fluorescing in green under an excitation light of 470 nm. (b) Semi-quantitative analysis of the fluorescence intensity of the spheroid shown in (a). Area of BSA distribution describes the spreading area of FITC-BSA fluorescence signals on the spheroid, i.e. drug distribution. Integrated intensity describes the sum of fluorescence intensity in the red-circled spheroid in (a), which corresponds to the total amount of FITC-BSA in the spheroid.

The cell-killing efficacy of DOX-HCl was investigated by co-incubation of DOX-HCl-loaded sperm ( $8 \times 10^4$  sperm in 100  $\mu\text{L}$  SP-TALP) with HeLa spheroids. Spheroids without any sperm or drug, with unloaded sperm and with DOX-HCl solution were cultured as control experiments. As mentioned above,  $8 \times 10^4$  sperm in 100  $\mu\text{L}$  solution can load at the maximum 1.5  $\mu\text{g}$  of DOX-HCl. Therefore, the control group using DOX-HCl solution was prepared with the same drug concentration (1.5  $\mu\text{g}$  DOX-HCl in 100  $\mu\text{L}$  SP-TALP). **Figure 4.7** illustrates the drug transport into a spheroid during 72 h when it was treated with DOX-HCl-loaded sperm. Red fluorescence shows the average intensity of 36 overlaid z-stack

images and indicates the presence of DOX-HCl. Gradually, DOX-HCl was found increasingly in the center of the spheroid over time. After 72 h, the size of all spheroids decreased due to the drug-induced cell death. Consequently, broken clusters and ruptured cells were observed in the medium (**Figure 4.7** at 72 h).

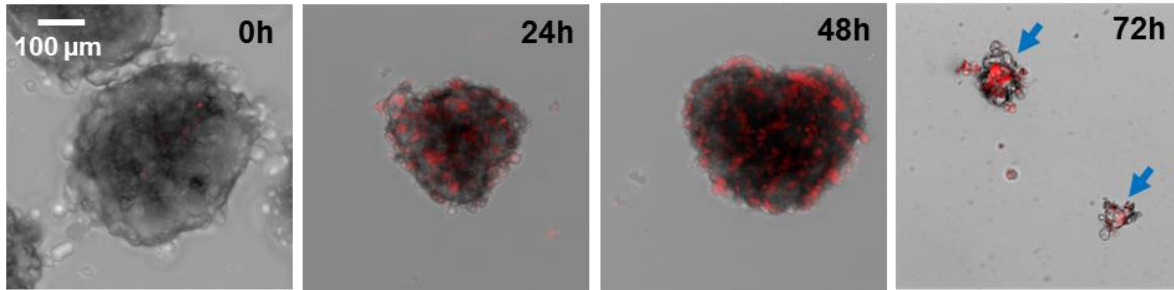


**Figure 4.7.** Overlaid z-stack images of HeLa spheroids under treatment by DOX-HCl-loaded sperm. Red color shows the fluorescence of DOX-HCl under an excitation light with a wavelength of 470 nm. Blue arrows point at ruptured spheroids.

**Figure 4.8** shows the cell viability analysis performed by LIVE/DEAD staining with SYBR Green Kit.<sup>117</sup> In the first 24 h of culture there was no significant change in all groups while after 48 h DOX-HCl-loaded sperm showed a cell-killing effect comparable to the DOX-HCl solution treatment with the same amount of DOX-HCl. A lower percentage of live cells was found after the treatment with DOX-HCl-loaded sperm (47%) or DOX-HCl solution (45%) compared to the spheroid control group (68%). After 72 h, no significant decrease of cell viability was found in the samples of control spheroid and DOX-HCl solution. In contrast, the sample with DOX-HCl-loaded sperm showed the lowest percentage of live cells (13%) among all groups. Unloaded sperm showed a negative effect on HeLa spheroids as well, as the percentage of live cells was only 37%, probably attributed to the spheroid disintegration induced by the sperm beating and hyaluronidases reaction (from sperm membrane) with the extracellular matrix. Hyaluronidases are enzymes expressed by sperm to catalyze the degradation of hyaluronic acid, the extracellular matrix of oocyte-

surrounding cumulus cells.<sup>118</sup> However, it is also well-known that hyaluronic acid plays an important role in the proliferation and migration of tumor tissue.<sup>92</sup> Therefore the motility and the hyaluronidases wielded by sperm cells allow them to penetrate deep into a tumor spheroid not only to disintegrate it but also to achieve an effective *in situ* drug administration.

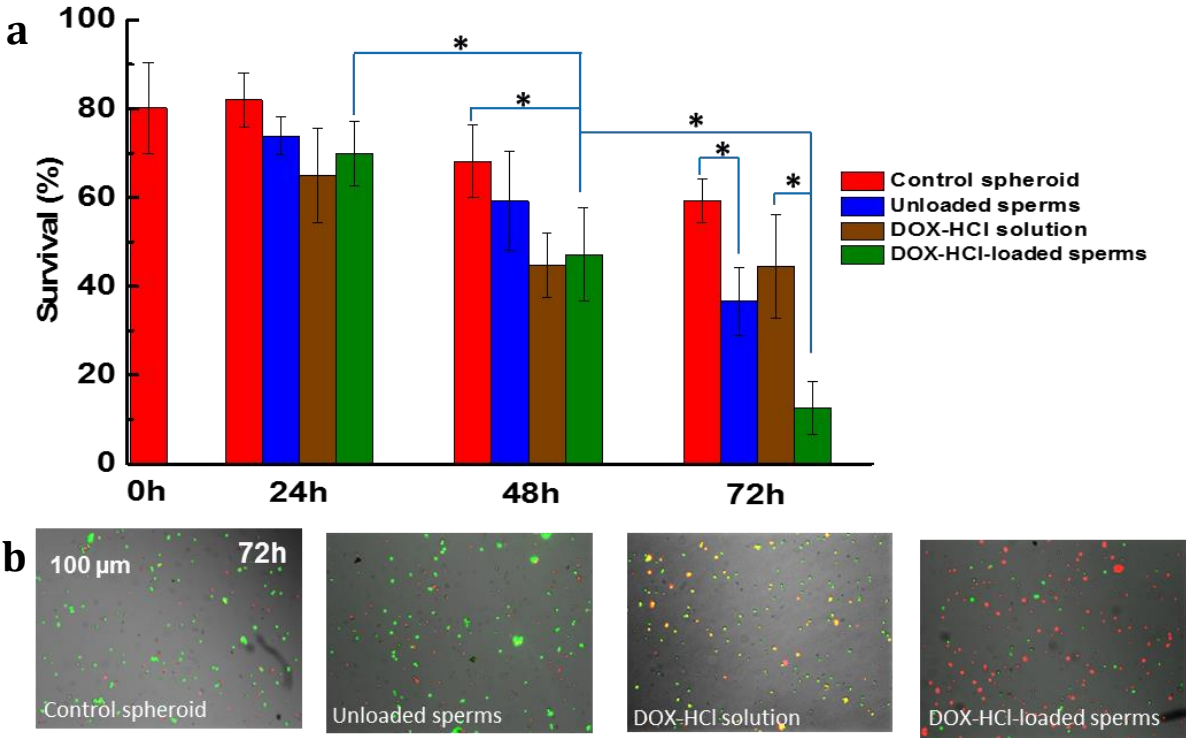


**Figure 4.8.** (a) Histogram of the percentage of live cells relative to the total amount of cells at different time points. ( $n = 4$ , cell count =  $10^4$  for each sample, \*  $p < 0.01$ , ANOVA analysis, degree of freedom for T-test is 6). (b) LIVE/DEAD staining images of cells from digested spheroids at 72 h.

In our experiment, HeLa spheroids were cultured for 3 days in advance. During cell culture in the lab, HeLa spheroids sustain a balance between cell proliferation and death.<sup>117</sup> When the number of live cells increases, the number of dead cells increases as well, especially in the necrotic core of the spheroid, as the nutrients from the medium can hardly reach the

interior cells. Since DOX-HCl in solution phase can be rapidly taken in by the outer cell layer of spheroids, a pronounced effect of the DOX-HCl solution group in the first 48 h was observed. However, when dissipated in the cell medium, diluted DOX-HCl was apparently not sufficient to induce the death of more cells from 48 h to 72 h (**Figure 4.8b**). This manifests an advantage of the sperm-hybrid delivery system for the *in vivo* application scenario: the ability to avoid drug dilution in body fluids. Overall, by means of functional combination of cargo protection and tissue penetration of sperm and the cell-killing efficacy of the drug, this biocompatible delivery strategy employing DOX-HCl-loaded sperm cells poses an intriguing alternative dosage form that is able to induce a death rate of nearly 90% after 72 h of treatment on HeLa spheroids, as it is shown in **Figure 4.8**.

#### 4.4.2. Cancer treatment by DOX-HCl loaded sperm-motors

*In vitro* drug delivery experiments were performed in a microfluidic channel to investigate the potential application of the sperm-hybrid micromotors for drug delivery (**Figure 4.9a**). As depicted in **Figure 4.9b**, sperm are first loaded with DOX-HCl, then coupled in microtetrapods. After essential guidance, the DOX-HCl loaded tetrapod-like sperm-motors reach the target and then discharge the drug loaded sperm.

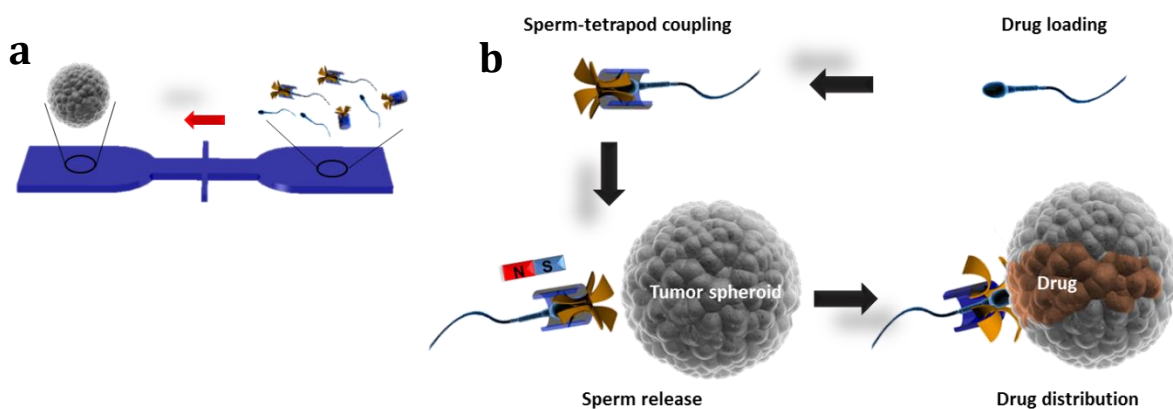


**Figure 4.9.** (a) Schematic of the microfluidic chip for drug-loaded sperm transport and delivery. (b) Schematic depicting tumor targeted drug delivery by a sperm-hybrid micromotor under magnetic guidance with mechanical sperm release trigger.

In order to observe the sperm release in details, sperm-hybrid micromotors were first guided to HeLa cell clusters by using external magnetic fields. **Figure 4.10a** shows an example of how a coupled sperm cell was released on a cells cluster, and adhered to one of its cells. The same sperm release mechanism was observed with DOX-HCl-loaded sperm-hybrid micromotors that targeted dense HeLa spheroids. We successfully achieved the transport of a DOX-HCl-loaded sperm cell through a microfluidic constriction channel and its release into a tumor spheroid. The distance travelled in this experiment was *ca.* 1.8 cm in total and the journey took approximately 8 minutes. The sperm cell was released as the microtetrapod arms hit the outer boundary of the tumor spheroid, and then continued swimming through it until it adhered to one of the cells. **Figure 4.10b** shows the release distribution of delivered DOX-HCl over 8 hours. The measured fluorescence intensity of the drug-loaded sperm decreased while the fluorescence signal spread over the spheroid over time. This indicates that DOX-HCl was released from the sperm cell into the spheroid. After 8 hours, the targeted HeLa cell experienced a significant cell body shrinkage (size decreased by about 40%), which is known to be a sign of the first stage of cell apoptosis.<sup>119</sup>

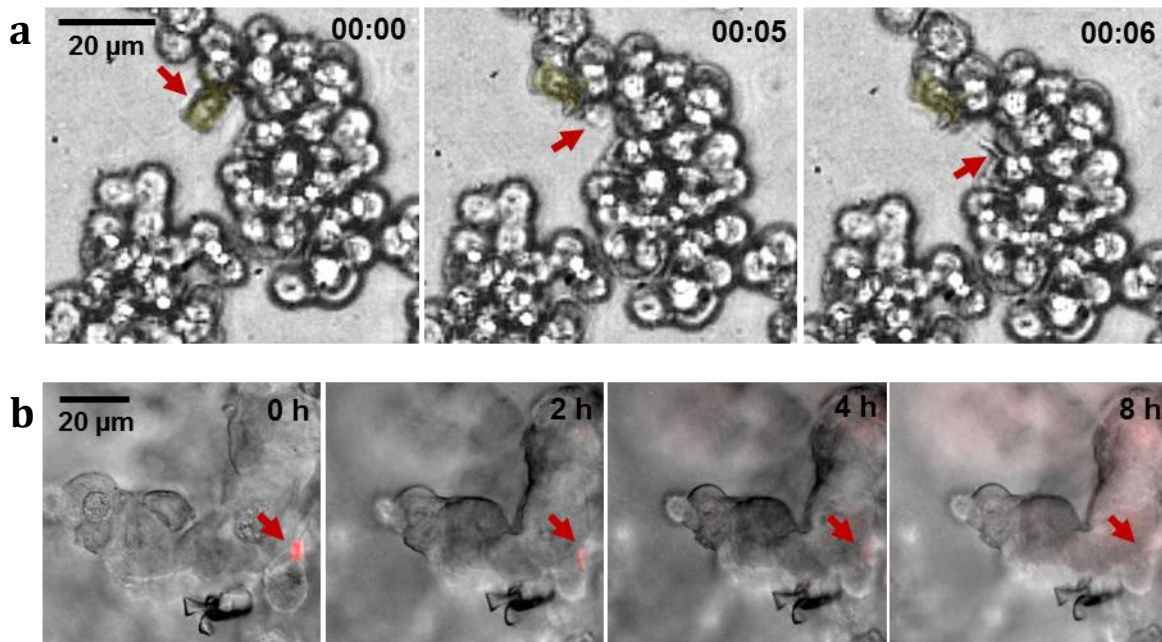


**Figure 4.10.** (a) Image sequence of the sperm release process when the arms hit HeLa cells. Time lapse in min:s. Red arrows point at the sperm head. (b) DOX-HCl distribution in a HeLa spheroid with overlaid z-stack images of the fluorescence channel (20 images with a stack separation distance of 2  $\mu\text{m}$ ). Red arrows point at the sperm head.

**Figure 4.11** shows scanning electron microscopy images of the membrane fusion of sperm and HeLa cells. A HeLa spheroid that was treated with unloaded sperm served as a control sample in this experiment. 24 hours after the sperm release event, the anterior part of the sperm head was fused with the targeted HeLa cell while the midpiece and the flagellum remained outside. Blebs and vesicles were observed on the HeLa cell that was fused with a DOX-HCl-loaded sperm, indicating its death by apoptosis (**Figure 4.11a**). Cells fused with unloaded sperm did not show such blebs (**Figure 4.11b**) and thus were presumably still alive, just as unfused cells. In literature, this interaction between sperm cells and somatic cells is attributed to the somatic fusion ability of acrosome-reacted spermatozoa.<sup>78</sup> So, by taking advantage of this sperm cell fusion ability, the direct transfer of the drug from sperm to cancer cells minimizes the dilution of drug into extracellular matrix or body fluids. At the current stage, the dosage that one single delivered sperm carried, and the resultant drug



distribution that could be observed nearby after tumor infiltration, was apparently not sufficient to induce the cell death of the whole spheroid. This makes the investigation of multi-sperm transport necessary, which will be pursued in future studies to achieve an effective tumor treatment.

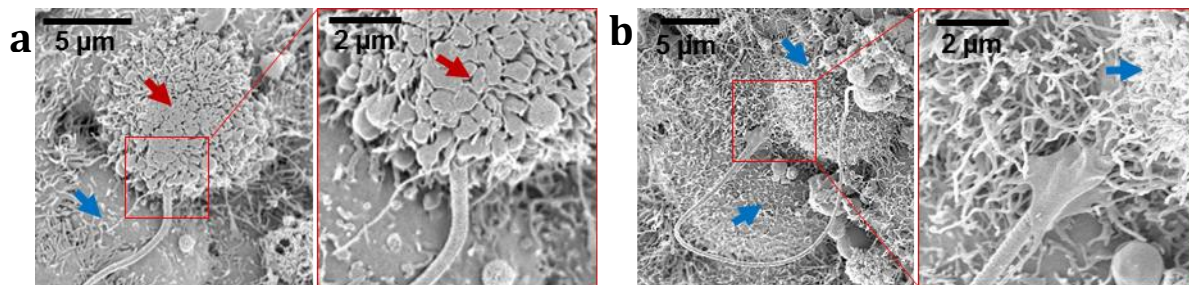


**Figure 4.11.** SEM images showing the sperm-HeLa cell fusion. (a) Cell fusion with the DOX-HCl-loaded sperm; (b) Cell fusion with an unloaded sperm. Red arrows point at a cell in apoptosis and the blue arrows point at live cells.

## 4.5. Summary

In summary, a drug delivery system based on sperm-hybrid micromotors was proposed. In such an assembly, sperm are utilized as drug carriers for potential cancer treatment in the female reproductive tract, as the sperm can swim into a tumor spheroid thanks to its capacity to fuse with somatic cells, transferring the drug efficiently to the target cell/model tumor in the process. sperm also showed a high drug encapsulation capacity of *ca.* 15 pg per sperm. Moreover, the sperm cell serves as propulsion source while a magnetic microstructure is used for guidance and release of the sperm: When the arms of the microstructure hit HeLa cells, they bend and thus open a way to free the sperm. Bovine sperm were used as model cells to load DOX-HCl as a model drug against HeLa cells. For that, HeLa cell spheroids were cultured as an *in vitro* tumor model. DOX-HCl was locally distributed into the HeLa cell

spheroids, showing higher tumor cell-killing efficacy (87 %) within the first 72h, compared to simple drug solution (55%) with the same dose.



## 5. Human sperm as a medication for early ovarian cancer

This chapter is based on the publication of arXiv preprint, 2019, <https://arxiv.org/abs/1904.12684>, titled: Human Spermrobots for Cancer-Relevant Drug Delivery.

### 5.1. Background

Ovarian cancer ranks fifth amongst cancer deaths in women, and top amidst all gynecological cancers. Less than 30 percent of women survive the disease for more than ten years.<sup>120</sup> Fallopian tubes are found to be the main primary lesion of ovarian cancer, especially high-grade serous ovarian cancer (HGSOC), the most common and aggressive type of ovarian cancer.<sup>121</sup> However, fallopian tubes are narrow structures situated deep inside the body, and thus, notoriously difficult to access, making it challenging to examine or eliminate them in a non-invasive manner. Most current anti-cancer treatments rely on generic chemotherapies and can lead to severe side effects, such as nausea, fatigue, anemia and infection.<sup>122</sup> Drug delivery of chemotherapeutics is usually mediated by passive carriers that rely on the body's circulatory system, and thus, pose significant challenges regarding their applicability for long-distance transport and targeting.<sup>123</sup> Therefore, new technologies that can access fallopian tubes to treat such cancer precursor lesions are sorely required.

Sperm-motors are excellent candidates not only to perform their natural function of fertilization but also to target gynecological cancers, in particular early pre-invasive HGSOC lesions, also known as serous tubal intraepithelial carcinoma (STIC) lesions, as an early non-invasive treatment option. **Chapter 4** presents the anti-cancer potential of bovine sperm. Given the ultimate goal of translating sperm-based drug delivery to human patients and considering potential acceptance issues surrounding bovine sperm, success of the next steps of this technology critically depends on the transferability to human material. This challenge represents no minor obstacles given the major differences in the makeup between animal

and human sperm. Thus, besides anatomical differences, sperm obtained from different species can vary in their membrane composition, which could impact on the drug translocation process.<sup>124</sup> Moreover, bovine sperm DNA is condensed via a single packaging protein known as protamine P1, whereas human sperm make use of two different protamines, P1 and P2, with also some residual histone packaging, leading to highly diverse chromatin structures and increased stability of chromatin in bovine over human sperm.<sup>125</sup> In addition, human sperm nuclei are more variable than those of many other species.<sup>126</sup> Thus, it is not surprising that translatability of results from bovine to human sperm is deemed challenging. Moreover, the efficacy of bovine spermbots has only been previously tested on overpassed cervical cancer cells, in which decades of genetic and phenotypic drift have led to major differences between cell line batches as well as to the original cancer.<sup>127</sup> Therefore, the efficacy of engineered human sperm in more patient-representative cancer models of the reproductive tract are highly desired. As the reproductive cancer of strongest unmet need and due to its unique etiology inside the fallopian tube, ovarian cancer, particularly HGSOC, is especially attractive in this regard.

In **chapter 4**, we presented a tetrapod-like microstructure for the transport of drug-loaded bovine sperm and confirmed the cancer-killing effect of this targeting drug delivery system. However, the drug-loading properties of human sperm and their successful implementation into a steerable micromotor remain unstudied. Here, we present a fully functional drug carrier based on human sperm. We shed light on the subcellular localization of a chemotherapeutic drug inside the sperm, investigate the interaction between the drug and human sperm and measure the anticancer efficacy of this system for the first time on 3D reproductive cancer cell cultures including early-passage ovarian cancer HGSOC patient samples (**Figure 5.1**). Moreover, we establish a new streamlined cap to transport and release human sperm. These streamlined sperm-motors start addressing major challenges towards the in vivo application of the technology, such as efficient targeting of cancer tissues via external magnetic guidance and drug-dose control through simultaneously supplying defined numbers of human sperm loaded with known concentrations of chemotherapeutic drugs.

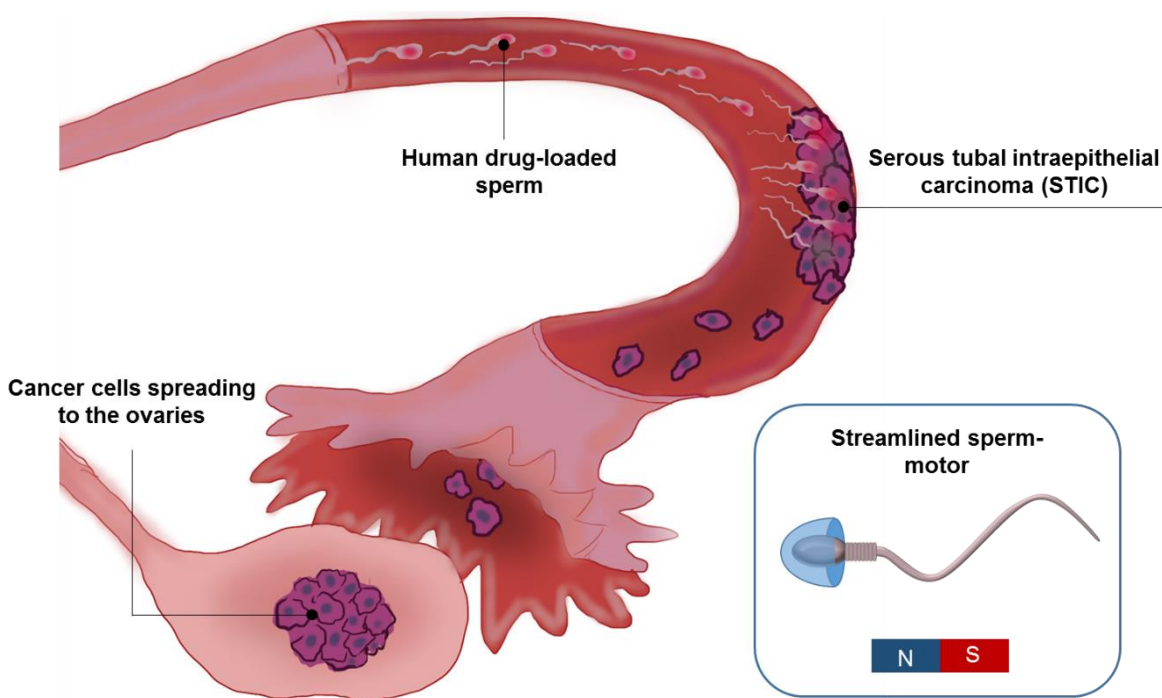


**Figure 5.1.** Human sperm-based drug-delivery system to target early ovarian cancer precursor lesions. Inset shows an alternative design for carrying human drug-loaded sperm.

## 5.2. DOX-HCl loading in human sperm

DOX-HCl was loaded into human sperm as introduced in **Section 3.3**. The loading ratio was determined by fluorescence spectrometry by a direct method, different from the measurement for bovine sperm. After 1 h of co-incubation,  $3.32 \pm 1.4\%$  of DOX-HCl ( $50 \mu\text{g/mL}$ ) was loaded into  $3 \times 10^5$  sperm. The drug loading in one sperm is  $5.53 \pm 2.34 \text{ pg}$ . Compared to the research on bovine sperm in **chapter 4**, in which the encapsulation capacity of individual bovine sperm was determined at around  $5.53 \text{ pg}$ , human sperm show a lower encapsulation capacity in line with their smaller size (around  $1/8$  the volume of bovine sperm). **Figure 5.2a** exhibits a cluster of human sperm loaded with DOX-HCl, as indicated by

their red fluorescence at an excitation wavelength of 458 nm (DOX-HCl autofluorescence). According to our observations by fluorescence microscopy, DOX-HCl was successfully loaded not only into motile but also into immotile sperm cells. In fact, we observed almost complete penetrance of drug loading in sperm obtained from a total of 22 patients and donors sampled in this study.

Using confocal laser scanning microscopy combined with an Airyscan system for high- and super-resolution sperm imaging, we obtained in-depth information on the intracellular location of the encapsulated drug inside human sperm. We first fixed the drug-loaded sperm with paraformaldehyde to preserve their internal structure. Outer sperm membrane was stained with Alexa Fluor 488-conjugated wheat germ agglutinin (WGA), a lectin selectively binding to N-acetylglucosamine and N-acetylneuraminic acid residues of glycoproteins present in the sperm membrane and detectable at an excitation wavelength of 514 nm.<sup>128</sup> Likewise, DOX-HCl was detected using an excitation wavelength of 458 nm. Acquired z-stack images, separated by 10 nm, showed clearly the drug distribution in different planes. As shown in **Figure 5.2b**, DOX-HCl was detectable predominantly in the sperm head. Notably, 98% of the sperm head is occupied by the nucleus after maturation.<sup>129</sup> Based on this fact, we conclude that DOX-HCl localizes to the sperm nucleus, in agreement with the high DNA-affinity exhibited by DOX, which might enable DOX-HCl binding to chromosomal sperm DNA.<sup>108</sup> We also observed structures resembling nuclear vacuoles<sup>130</sup> in the drug-loaded sperm (**Figure 5.2c**), where little or no DOX-HCl could be detected. The location of these structures differed among individual sperm. In addition to the advantages of DOX-HCl as a therapeutic molecule, it also has potential to be used as a dye to further characterize sperm nuclei in living and motile sperm cells in the future. We further confirmed that WGA can serve as an efficient membrane dye for human sperm, clearly depicting the structure of the sperm membrane around the head, midpiece and tail regions. Particularly, there was a staining difference between the peri-acrosomal space and the post-acrosomal region, which in the future could be helpful to gain insights into different subcellular compositions of sperm membranes. Based on the 3D-reconstructed image of the DOX-HCl loaded sperm in **Figure 5.2b**, the volume of the sperm was integrated to be 14.2  $\mu\text{m}^3$ . Thus, the DOX-HCl density was calculated to around 0.38 g/mL as the ratio of the above-mentioned amount of

drug loaded per sperm to its volume. Since the nucleus of a single sperm contains around  $3.23 \times 10^{10}$  nucleotides,<sup>131</sup> we deduce that around  $1.70 \times 10^{-23}$  g of DOX-HCl would be available for binding per base pair, meaning that a single DOX-HCl molecule could bind to roughly every 6<sup>th</sup> nucleotide of the DNA.

Moreover, the percentage of motile sperm was preserved after drug loading, similarly to our previous work performed on bull sperm. Statistically, the average velocity of human sperm after 1 h of drug loading ( $18 \pm 5$   $\mu\text{m/s}$ ) showed no significant difference to unloaded sperm ( $21 \pm 5$   $\mu\text{m/s}$ ) according to measurements using a computer-assisted sperm analysis software package (CASA auto-tracking system). Since the properties of sperm samples from different patients and donors markedly differ, we compared the same sperm sample before and after drug loading. The above-mentioned drug loading process was performed at room temperature to optimize sperm motility and viability for extended periods of time (about 24 h). We also studied sperm motility at 37°C as the physiological temperature at which human sperm operate in vivo. In this experiment, an unloaded sperm sample served as a control, which was incubated in sperm medium (SP-TALP) under the same incubation and purification conditions as the drug-loaded sperm but in the absence of DOX-HCl. Motilities of both sperm samples decreased similarly over time: after 8 h of incubation, around 10% of sperm remained motile in both groups (**Figure 5.2d**).

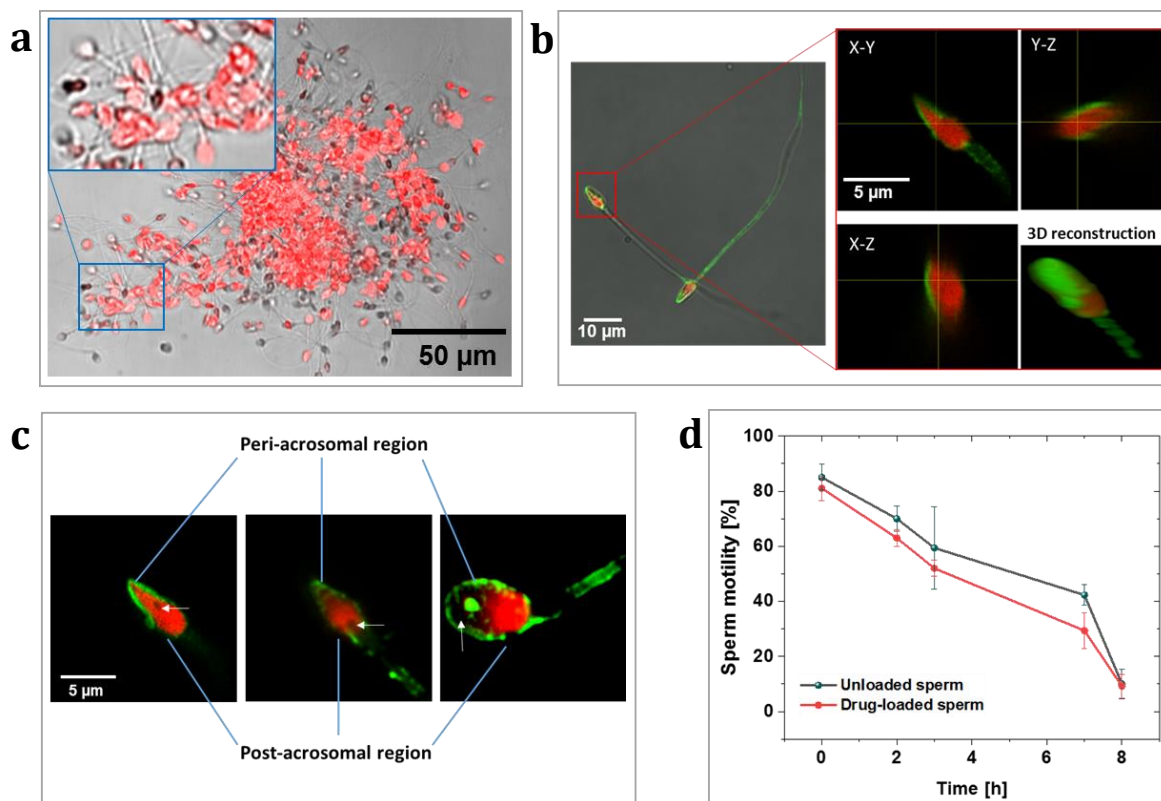


**Figure 5.2.** DOX-HCl loading sperm. (a) Merged fluorescence and bright-field images of DOX-HCl-loaded sperm. Red color indicates autofluorescence of DOX-HCl. (b) Fluorescence and Airyscan images of two DOX-HCl-loaded human sperm, revealing the precise location of DOX-HCl inside sperm heads. Green indicates membrane staining by Alexa Fluor 488-conjugated wheat germ agglutinin (WGA). Red indicates DOX-HCl autofluorescence within sperm heads. (c) DOX-HCl localizes to the nucleus inside the sperm head. Detailed information on three different sperm cells. White arrows point at structures resembling nuclear vacuoles. DOX-HCl autofluorescence shown in red; Alexa Fluor 488-conjugated wheat germ agglutinin shown in green. (d) Percentage of motile sperm monitored over 8 h in unloaded and DOX-HCl-loaded human sperm (data represent means of two different samples, with a sperm count of 100 sperm per sample. Error bars represent standard deviations between samples).

### 5.3. Anticancer effect

We evaluated the anticancer effect of DOX-HCl-loaded human sperm by performing cytotoxicity assays of relevant cancer cell spheroids. Firstly, we tested the influence of sperm medium (SP-TALP) on 3D cell cultures of cervical cancer-derived HeLa cells. After 96 h of co-incubation, we detected  $148,406 \pm 5,531$  living cells after treatment with SP-TALP (100  $\mu$ L SP-TALP in 4 mL cell solution), showing no significant difference to the cell number in the untreated control group ( $151,250 \pm 1,750$  cells). Since the sperm medium had no significant influence on cell proliferation, any cell number variations in the subsequent experiments can be attributed to the anti-cancer effects of human sperm and/or the chemotherapeutic drugs they carried. **Chapter 4** presented the killing effect of drug-loaded bovine sperm on HeLa cells spheroids. To test if drug-loaded human sperm were also able to induce cytotoxicity in HeLa cell spheroids, we plated equal amounts of HeLa cells ( $2 \times 10^5$  cells resuspended in 4 mL cell medium) onto 16 3.5-cm cell-repellent dishes and incubated them for 2 days to induce spheroid formation. The resulting spheroids were split into 4 groups and co-incubated separately with the following samples: (i) DOX-HCl-loaded and (ii) unloaded human sperm ( $10^4$  sperm for each sample, suspended in 100  $\mu$ L SP-TALP), (iii) 53 ng DOX-HCl dissolved in 100  $\mu$ L SP-TALP, equaling the amount of DOX-HCl added in (i), and (iv) a blank control using 100  $\mu$ L of HeLa cell medium. DOX-HCl-loaded sperm were purified to remove the excess of drug after the loading process, prior to treatment. After 96 h of treatment with DOX-HCl solution HeLa spheroids showed no difference compared to the blank control and remained intact displaying smooth and distinct outer spheroid boundaries. By contrast, spheroids treated with DOX-HCl-loaded sperm became severely disintegrated leading to a plethora of small cell aggregations, floating cells and ruptured cell fragments (**Figure 5.3a**), while unloaded human sperm elicited intermediate effects. Conceptually, metastatic cancer progression relies on individual, or clusters of, cancer cells dissociating from the original tumor, traveling to their secondary sites, and reattaching there.<sup>132,133</sup> To mimic aspects of this process in vitro, we briefly trypsinized the spheroids after 96 h in all groups to obtain single-cell suspensions that we re-seeded into 10-cm cell culture dishes. After 12 h of attachment inside the incubator, we estimated the cell re-attachment capability

as the ratio of attached cells in the group-of-interest to that of the control group. As demonstrated in **Figure 5.3b**, treatment with DOX-HCl-loaded human sperm led to drastically reduced re-attachment rates of HeLa cells, as illustrated by an elimination of 93.8% of the cells compared to the control. Unloaded human sperm also impacted on HeLa spheroids, leading to a reduction in re-attachment to 58.0%. This sperm-specific effect that was independent of DOX-HCl could be due to partial spheroid disintegration and cell damage induced by the sperm' hyaluronidase reaction and tail beating, an intriguing aspect of this micromotor system that requires further investigation in the future. It was reported before that the plasma membrane and DNA of cancer cells can be damaged by external mechanical beating produced by rotating microdiscs.<sup>134</sup> Our findings suggest a new route for mechanically induced cancer cell death by sperm tail beating. Compared to the microdisk beating, sperm possess a more powerful motorized structure, with their tail beating capable of generating forces up to 450 pN.<sup>66</sup> Cell integrity can be damaged under such a hitting force. In the drug solution group, which contained the same overall DOX-HCl amount as the drug-loaded sperm, DOX-HCl was present at a final concentration of 13.25 ng/mL in the cell medium, lower than the effective dose that HeLa cells are sensitive to.<sup>135</sup> Consequently, no effective impact of cell re-attachment was observed in this group, in agreement with our previous results using bull sperm.

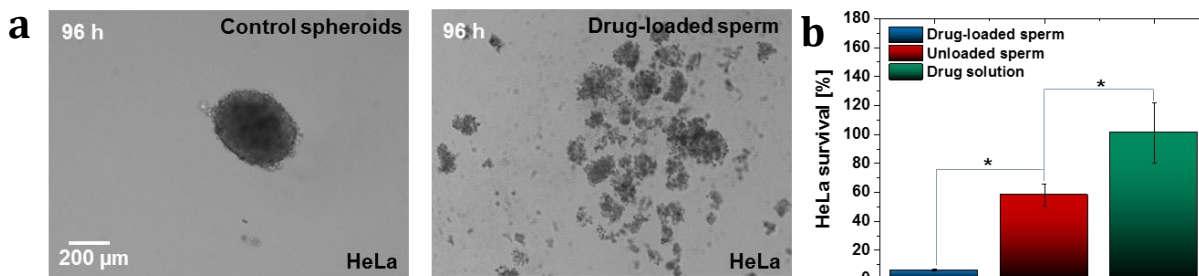


**Figure 5.3. Anti-cancer effects of DOX-HCl loaded human sperm on HeLa cells.** (a) Optical microscopy images of HeLa cell spheroids before and after 96 h of treatment with drug-loaded human sperm. (b) Survival rate of HeLa spheroid-derived cells after 96 h of



treatment (data represent means +/- standard deviations of n = 4 independent biological replicates, HeLa cell count  $\sim 1.5 \times 10^5$  in blank spheroids. \* p < 0.01, ANOVA analysis).

HeLa cells were established in the 1950s as the first in vitro cancer model system and immortalised cancer cell line. While major breakthroughs have been and are being accomplished using this cell line, the thousands of passages that HeLa cells have undergone since its establishment have led to the acquisition of many de novo characteristics that vary between different HeLa batches and their cervical cancer of origin.<sup>136</sup> Therefore HeLa cells and other common overpassaged cancer cell lines are limited in predicting the cellular and molecular behaviors of cancers and patient responses in vivo, such as drug resistance mechanisms.<sup>137</sup> To obtain a better understanding of the reaction of appropriate original tumor cells to DOX-HCl-loaded sperm, we assessed the anti-cancer effects on ex-vivo 3D cultures of early-passage ovarian cancer samples derived from an HGSOc patient (OCMI66). The OCMI66 cells are part of a living ovarian cancer cell biobank recently generated and characterized by one of our teams at the Manchester Cancer Research Centre (Nelson et al., has been submitted). The samples in this biobank were extensively validated by p53 profiling, exome sequencing, global transcriptomics and karyotyping based on single-cell whole genome sequencing. Moreover, these cells have been cultured in vitro for only short time periods, minimizing the risk of genetic and phenotypic drift phenomena that could potentially mask key molecular features of the original tumour. Indeed, drug profiling of these cancer samples demonstrated that their sensitivities are consistent with patient responses, highlighting the potential of these biobank cultures as an invaluable tool for making in vitro discoveries with improved translational potential over conventional cancer cell lines.

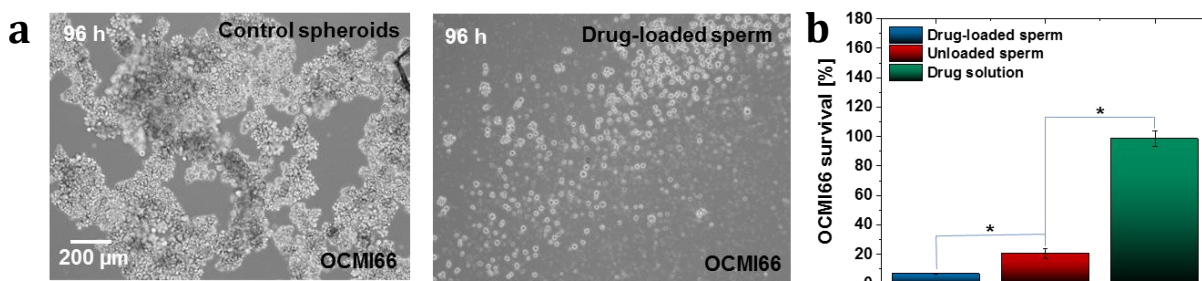


**Figure 5.4. Anti-cancer effects of DOX-HCl loaded human sperm on HGSOC cells.** (a) Optical microscopy images of HGSOC cell spheroids before and after 96 h of treatment with drug-loaded human sperm. (b) Survival rate of HGSOC spheroid-derived cells after 96 h of treatment (data represent means  $\pm$  standard deviations of  $n = 4$  independent biological replicates, HeLa cell count  $\sim 1.5 \times 10^5$  in blank spheroids. \*  $p < 0.01$ , ANOVA analysis).

Ovarian cancer is of particular interest to the spermbot technology presented in this work, as it represents the highest unmet need of all gynecological cancers.<sup>120</sup> Moreover, while it was long assumed that the majority of ovarian cancers originate from within the ovaries, it is now well established that the most aggressive and common type of ovarian cancer, HGSOC, develops as STIC lesions inside the fallopian tube, an area of the reproductive tract currently impossible to access for molecular analysis with non-invasive technologies.<sup>138</sup> This recent dogma change in ovarian cancer etiology makes sperm-based drug delivery to pre-invasive HGSOC lesions a highly desirable and timely approach.

The spheroids that OCMI66-derived HGSOC cells formed were looser and smaller compared to HeLa spheroids, possibly because of the high migration activity we observed in these cells when grown on 2D cell culture dishes (**Figure 5.4a**). Similar to sperm treatment of HeLa cells, DOX-HCl-loaded human sperm showed a high reduction of re-attachment of OCMI66-derived cells of up to 93.3%, while DOX-HCl solution barely influenced the re-attachment rates of OCMI66-derived cells. Surprisingly, unloaded human sperm also showed a strongly reduced re-attachment of 79.4% in these experiments (**Figure 5.4b**). A potential reason could be the looser structure of OCMI66-derived spheroids over those of HeLa cells, making

them more susceptible to sperm-mediated disintegration and cell death through tail beating. These tests demonstrate a high effectiveness of drug-loaded human sperm on early-passage HGSOC cancer samples and have potential to lay the groundwork for new routes of biocompatible and non-invasive cancer treatments in humans in the future.

DOX-HCl-loaded sperm represent a new approach with great potential for effective cancer treatment of gynecological cancers of unmet need. The approach combines advantages of chemical medication with biological properties of sperm (active motion, somatic cell fusion<sup>78</sup> and mechanical tail beating). Sperm-mediated drug delivery holds promise for drug dosing, encapsulation and transport. Specifically, membrane encapsulation can protect functional drugs (DOX-HCl) from dilution by body fluids and enzymatic degradation. Moreover, the presence of chromosomes in the sperm head has potential to provide ample opportunities for intracellular storage of DNA-binding drugs such as DOX-HCl. In addition, the ability to self-propel combined with peristalsis of female reproductive organs make sperm attractive for carrying drugs for long durations and distances inside the gynecological tract in a protected manner. Since this is the first exploration of human sperm as a therapy for gynecological cancers, the complete mechanism of drug transfer remains unclear. However, it is intriguing to speculate that the ability of sperm to fuse with somatic cells as previously reported has potential to enhance the drug uptake by cell-to-cell transfer.<sup>[14,24]</sup> In this regard, it is notable that sperm are capable to fuse with a variety of cells and that the resulting chimeric cells can be stably cultured for more than 50 passages.<sup>80</sup> As a consequence, local transfer of entrapped drugs to targeted cancer cells via sperm-cell fusion and/or alternative mechanisms could increase the utilization ratio of the loaded drugs, which could improve drug efficacy and potentially reduce the development of drug resistance.<sup>139</sup>

#### 5.4. Streamlined sperm-motor transport toward tumor spheroid

Although randomly propelling DOX-HCl-loaded human sperm show an encouraging therapeutic effect on the cancer cells tested in this study, being able to target the drug-loaded sperm to the cancer spheroids would facilitate more efficient dosage and reduce undesired drug accumulation. Towards this aim, a streamlined cap was designed as a hollow semi-ellipsoid structure for human sperm transport. The contact surface in an ellipsoid shape can largely avoid turbulence flow, thereby decreasing the pressure drag on the structure. As illustrated in **Figure 5.5a**, the water resistance and energy loss of this streamlined cap were reduced to one third of that of a tubular cap based on the same diameter and length. With a lower flow resistance, such a sperm-hybrid micromotor saves energy and is thus expected to swim for longer time periods. These microcaps were fabricated by FSTL and coated with Fe so that they can be aligned by external magnetic fields (for details, see 3.2). Owing to protective coating with Ti, the microcaps had no negative impact on cell growth compared to the blank control group (**Figure 5.5b,c**), consistent with Ti being considered as a biocompatible material<sup>140</sup>.

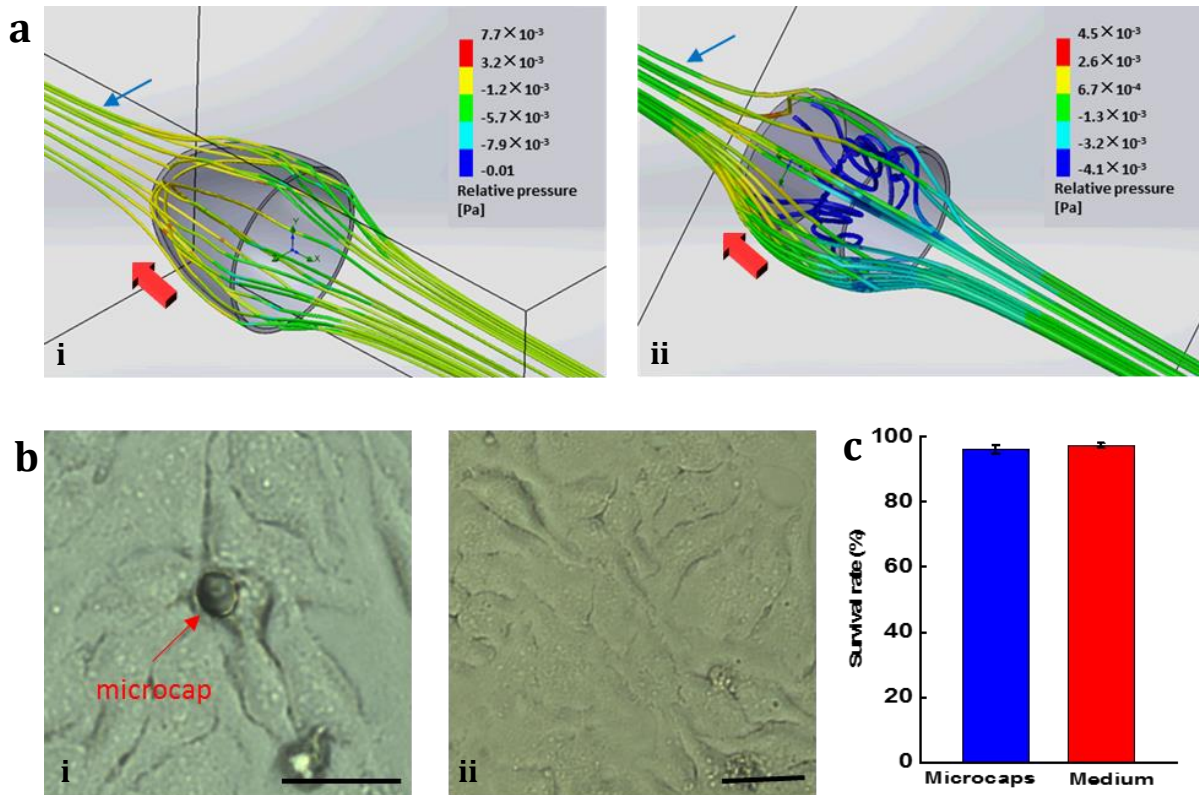


**Figure 5.5.** (a) Flow simulations of (i) a streamlined and (ii) a tubular sperm cap based on the same diameter and height. Red arrows indicate the swimming direction of the microcaps. Blue arrows point at the fluid flow. Finite element analysis tool: SOLIDWORKS Flow Simulation; flow medium: water; velocity: 21  $\mu\text{m/s}$  (the average velocity of a spermbot at 20°C in HeLa medium); roughness: 0;  $f$ : total resistance. Biocompatibility evaluation of the microcaps. (b) Optical images of (i) microcaps treated group and (ii) cell medium control group. Scale bars: 30  $\mu\text{m}$ . (c) HeLa cell survival after 3 days culture.

The sperm were mechanically coupled by co-incubating them with the caps (**Figure 5.6a**). The large opening at the equatorial plane of the cap enabled us to couple up to 3 human sperm in a single cap at the same time (**Figure 5.6b**), showing a new way for multiple sperm transport (**Figure 5.6c**). Apart from the difference in shape from the previous tetrapod-motor, the new cap designs were much larger in relative size ratio. Specifically, the opening diameter was  $\sim 6$  times as big as the width of human sperm heads for the new cap compared to a 4:1 ratio for the previously reported tetrapod-motor.<sup>[14]</sup> The feasibility of generating functional sperm-based micromotors in this size range represents a critical step towards future real-time in vivo imaging of spermbots inside the reproductive system in preclinical experiments.<sup>34</sup> As such, these hybrid micromotor designs provide an important starting point to facilitate real-time guidance of sperm to their desired destinations within the reproductive tract.

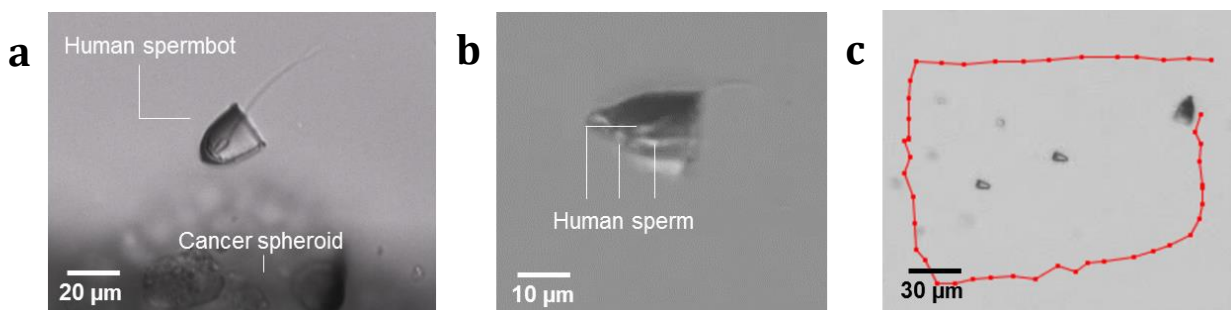


**Figure 5.6.** (a) Drug-loaded spermbot approaching OCM166 cell spheroid. (b) Transport of up to three human sperm using the proposed streamlined magnetic cap. (c) Magnetic guidance of a human spermbot.

Moreover, here we developed a simple sperm release mechanism by swerving the cap via rapid change of orientation of the imposed magnetic field (**Figure 5.7a**). This technique has been applied before to release individual cells or particles hydrodynamically from an artificial support structure.<sup>141</sup> **Figure 5.7b** shows the complete process to transport and release sperm onto a cancer cell spheroid. The sperm was coupled to a streamlined microcap and guided to an OCM166-derived HGSOC cell spheroid. Then, we rotated the external magnet to turn over the microcap thereby releasing the sperm. The contact surface of the sperm and the cap are assumed to be smooth without causing friction in between the two surfaces. As a result, the theoretical swerve angle for decoupling is  $90^\circ$ . Whereas the sperm head undergoes a wiggling angle ( $57^\circ$ ) on the short-time scale to balance the torque generated by tail beating, the resulting theoretical swerve angle was deduced to be  $147^\circ$  to ensure a successful release. The larger the swerve angle, the higher the swimming stability of this system but the more difficult it is to release the sperm. Hence, this approach relies on a compromise between swimming stability and release reliability to ensure optimal microcap function. After the sperm escaped the cap, it swam towards the cancer cell spheroid tissue. In the future, further experiments need to be implemented to evaluate the efficiency of this release mechanism for cancer treatment.

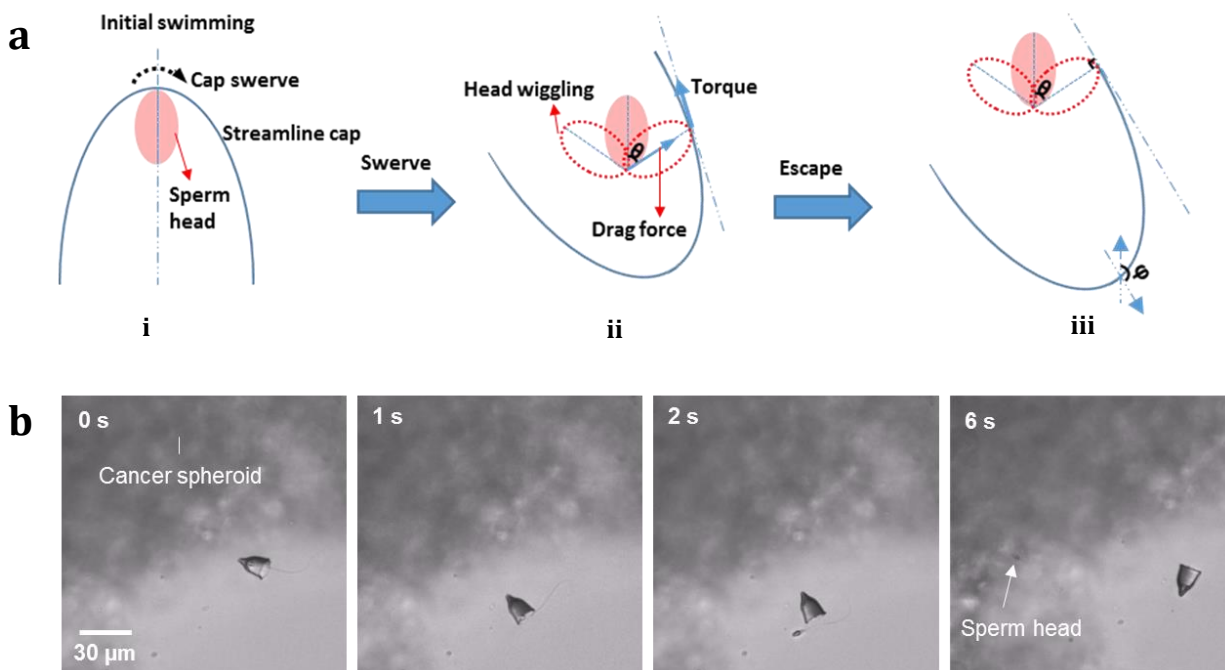


**Figure 5.7.** (a) Ejection mechanism of sperm from streamlined cap. The sperm head was regarded as an ellipse in its projective plane, in which the projection of the streamlined cap takes the shape of a semi-ellipsoid structure (blue line). The encapsulated sperm bears a drag force along its long axis (i) and can only move tangentially in the semi-ellipsoid structure of the cap. The cap swerving is carried out by rapidly changing the direction of the imposed magnetic field. In this situation the torque is always directed along the tangent line in the same direction of the drag force during continuous swerving of the cap (ii). Sperm escape occurs when the drag force becomes perpendicular to the tangent line (iii). After taking the wiggling angle of the sperm head ( $\theta$ ,  $57^\circ$ , middle panel) into account, the resultant critical decoupling angle is shown as  $\varphi$  ( $147^\circ$ ). (b) Guidance and release of a DOX-HCl-loaded human sperm onto an OCMI66 cell spheroid.

## 5.5. Summary

This chapter presents the application of human sperm combined with DOX-HCl for potential treatment of female gynecologic diseases, in particular cervical and ovarian cancers of unmet need. Human sperm can encapsulate DOX-HCl in their crystalline nuclei,<sup>72</sup> where we observed its presence using high- and super-resolution laser microscopy. Moreover, due to the compact membranes of sperm,<sup>142</sup> hydrophilic drugs taken up and encapsulated by the sperm are well protected from dilution by body fluids and enzymatic degradation. We calculated that each DOX-HCl loaded sperm can hold around 5.53 pg of drug, indicating a potential binding ratio of around 1:6 DOX-HCl molecules to nucleotides. Neither the viability nor swimming performance of human sperm was markedly affected by drug loading, indicating the robustness and potential suitability of this protocol for future treatments using human sperm as drug carriers. These findings are likely to significantly broaden this research field not only regarding sperm as drug carriers, but also for using DOX-HCl as an alternative non-invasive nuclear dye to further observe and characterize nuclear structures inside living sperm. Re-attachment tests demonstrated strong anti-cancer effects of drug-loaded human sperm on spheroids derived from a commonly used cervical cancer cell line and HGSOC cells recently extracted from an ovarian cancer patient. The latter cells are part of a newly established ovarian cancer biobank, known to display key features of the original cancer such as the responsiveness to certain chemotherapeutic drugs. Over 94% of cancer cells were incapable of re-attaching after 4 days of treatment in both cases. Combined with the proposed streamlined microcaps, drug-loaded human sperm can be precisely guided to the specific cancer target in vitro.



## 6. Sperm-motors for cargo delivery through flowing blood

This chapter is based on the publication titled: Sperm Micromotors for Cargo Delivery through Flowing Blood. Reprinted with permission from [ACS nano, 2020, 14(3), 2982-2993] ([doi.org/10.1021/acsnano.9b07851](https://doi.org/10.1021/acsnano.9b07851)). Copyright [2020] American Chemical Society.

### 6.1. Background

While micromotors are attracting intensive attention in the exploration of the next generation of drug delivery systems, the blood circulation system, as the most common administration route, has only rarely been explored as a transportation route for micromotors. Among the few attempts, catalytic microjet engines were shown to swim in H<sub>2</sub>O<sub>2</sub> solutions containing ten times diluted red blood cells under static conditions.<sup>143,144</sup> Magnetically-driven micro-helices were also tried out in blood dilutions, observing a stick-and-slip motion, which was related to the colloidal jamming of the blood cells.<sup>145</sup> Another attempt was made by using CaCO<sub>3</sub> microparticles as potential hemostatic agents.<sup>49</sup> Unlike the first two cases where micromotors moved in static blood solutions, CaCO<sub>3</sub> microparticles swam against blood flowing up to 5.9 mm/s by the propulsion of locally generated CO<sub>2</sub> bubbles, though with only random motion due to the lack of a guidance mechanism. However, the above-mentioned self-propelled particles and microengines were driven by toxic fuels like H<sub>2</sub>O<sub>2</sub> or acidic substances, being far away from any application in living organisms when envisioning a medical treatment. Another strategy has been to turn red blood cells (RBCs) into micromotors. Wu *et al.* functionalized RBCs with magnetic particles for guidance while propelling them with acoustic waves. The experiments in this work were focused on studying the stability of RBCs micromotors under acoustic waves, but experiments under

flow conditions showing a specific function of cargo release were not shown.<sup>55</sup> A more recent work reported a 2 mm helical robot able to perform mechanical rubbing of blood clots in *in vitro* and *ex vivo* models containing PBS buffer against a flow of ca. 10 mL/h, which corresponds to a flow velocity of 0.22 mm/s (considering a vessel diameter of 4 mm).<sup>146</sup> The flow rate in this work was similar to that of small arterioles, capillaries, and venules. However, the operation of micromotors under more realistic blood stream conditions remain a challenge due to the high complexity of the blood fluid and its high flow rates in the circulatory system. Besides, blood contains a variety of macro- and small molecules which can influence the motion and function of any medical micromotor.<sup>147</sup> Blood pH is regulated in a narrow range between 7.35 and 7.45, thus, any modification of the blood composition by adding other substances for fueling the micromotors would be lethally harmful in any further realistic application.<sup>148</sup> Half of the whole blood consists of different cell types, including  $5 \times 10^9$  red blood cells/mL,<sup>147</sup> which would continuously interfere with the micromotors mobility, consuming a lot of energy in the process. Finally, micromotors are also exposed to the innate immune system in blood, which would eliminate the micromotors by e.g. phagocytosis when specific receptor activation is induced by the micromotors<sup>149</sup> or the micromotors have too small size ( $<5 \mu\text{m}$ ).<sup>150,151</sup>

To overcome the abovementioned hurdles, sperm-based micromotors seem more promising to our view. The most important feature of sperm micromotors to operate in the blood stream, is in our view their ability to swim against flow (rheotaxis), which is one of the most efficient guidance mechanisms for sperm to reach the oocyte when accomplishing their natural function,<sup>152</sup> Additionally, in combination with a synthetic magnetic scaffold, sperm-micromotors can be precisely guided and operated by an external magnetic field to further release a cargo at the right place and time. It is also believed that sperm-micromotors could operate for longer times in the human body before being eliminated by the immune system due to their higher propulsion force compared to the migration speed of phagocytes,<sup>153,154</sup> and their size differences.<sup>151</sup> In addition, some specific proteins expressed on the sperm membrane and the proteasomes can suppress the local immune reaction.<sup>155,156</sup> It is also worth noting that unlike active bacteria, sperm do not proliferate or secrete any harmful bio-substances, making them safe for medical use.

In this chapter, we present streamlined-horned caps (SHCs) hybrid sperm-micromotors (**Figure 6.1**), which can efficiently and controllably swim against flowing blood. We optimize the hydrodynamic structure of the sperm-micromotor to be able to adapt to high flow rates and explore its flow-resisting capability. The sperm-micromotors furthermore are assembled into train-like carriers (sperm-trains), allowing the guidance of multiple sperm and enabling multiple functional cargoes transport. As a proof-of-principle of a potential medical use, we functionalize the microcaps with heparin-loaded liposomes to realize a localized anticoagulant function. This study not only opens up new application scenarios for medical micromotors in the circulatory system, but envisions a new administration route of sperm or sperm-hybrid micromotors for future therapeutical applications.

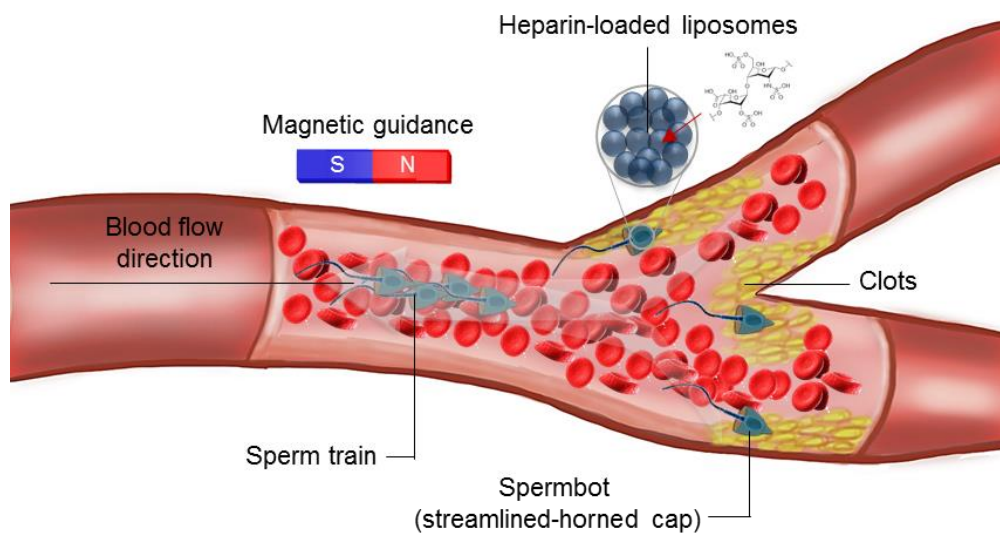


**Figure 6.1.** Concept of the blood-adapted SHC sperm-micromotors

## 6.2. Design and characterization

Different to other *in vivo* applications, any medical mission in blood faces a particularly complicated working environment, including the presence of various substances and cells, complex hemorheological properties, and high flow rates. In order to efficiently design and

manufacture a sperm-micromotor, we first ran flow simulations and compared the hydrodynamic characteristics of two different designs, a tubular and a streamline-horned cap (SHC) with the same diameter (13  $\mu\text{m}$ ) and height (15  $\mu\text{m}$ ). **Figure 6.2a** shows the relative pressure on both cap designs when subjected to an aqueous solution containing solid spheres of about 5  $\mu\text{m}$  diameter. As expected, the tubular cap is obstructed by the spheres-mimicking cells on its front surface with a high static pressure. In contrast, the shape of the SHC facilitates the passing of the sphere-mimicking cells forming a stable wake flow around it. At a swimming speed of 50  $\mu\text{m/s}$ , the energy loss of the SHC is about 47% of the tubular cap one. To verify the performance of both designs, the microcaps were fabricated by two-photon lithography (SEM images of the SHC are shown in **Figure 6.2b**), followed by the coating of Fe, Ti and  $\text{SiO}_2$  nanofilms for both magnetic guidance and biocompatibility.

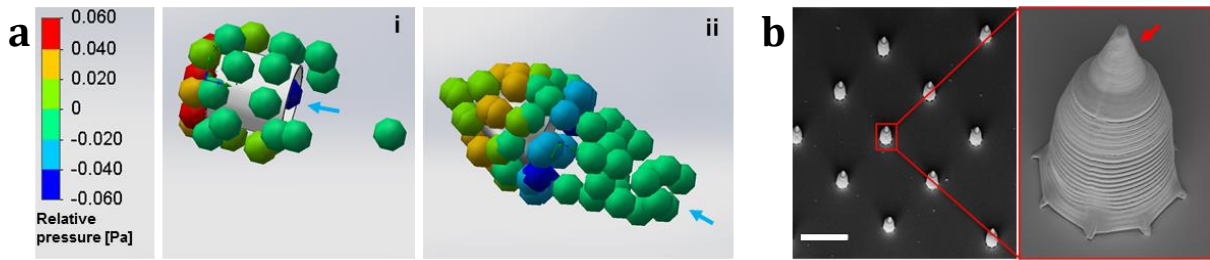


**Figure 6.2.** (a) Hydrodynamic simulations of (i) tubular and (ii) SHC caps, assuming a swimming speed of 50  $\mu\text{m/s}$  and particles mimicking red blood cells of 5  $\mu\text{m}$  in diameter. Blue arrows point at the swimming direction. (b) SEM images of SHCs. The red arrow indicates the horn structure used for enhancing the micromotor motion in blood. Scale bar: 40  $\mu\text{m}$ .

### 6.3. Swimming in blood

Microcaps were mixed with sperm and added into 4 $\times$  diluted whole blood. We used bovine sperm for our experiments as their morphology is similar to human sperm. As a result, we observed that free sperm retained a high swimming performance, with an average speed of

76 ± 17 μm/s (n = 17), comparable to free sperm in sperm medium (89 ± 14 μm/s, n = 30). However, due to the obstructing blood cells and the lack of guidance, freely swimming sperm tended to swim on circular trajectories forming hollow regions from where the sperm were not able to escape (see **Figure 6.3a,i**). When swimming in confined space, such as the oviduct, sperm tend to swim near the walls (thigmotaxis), displaying circular or curvilinear trajectories due to the chirality of the flagellar beating.<sup>157</sup> The asymmetric beating of the flagellum pushes the nearby blood cells out of the swimming area. As more and more cells are pushed close to each other, the cells form a dense boundary wall, trapping sperm inside the formed pool. For that reason, the use of a synthetic component, in particular a magnetic cap, serves as a guidance vehicle for sperm to ensure the controllable delivery of therapeutic cargoes at the desired location by applying external magnetic fields. As an example, the coupling efficiency of sperm and SHC microcaps can reach up to 62 ± 19% (n = 6) with respect to the total amount of microcaps. In this case, the sperm concentration was 3×10<sup>4</sup> sperm /μL and the number of microcaps was 100 caps/μL.

In agreement with the hydrodynamic simulations, the magnetic tubular sperm-micromotors could not swim in 4× diluted blood for a long period of time due to the heavy load created by the stacked blood cells on the flat front side of the tubes, as shown in **Figure 6.3a, ii**. In contrast, SHC sperm-micromotors swam more efficiently, even in 2× diluted blood thanks to the front horn which easily squeezed through the blood cell crowd (see **Figure 6.3a, (iii)**). In this way, blood cells in front of the micromotor were pushed aside, pass by in the vicinity of the cap wall forming a broad wake flow behind the SHC (**Figure 6.3b**). From 8× to 2× diluted blood, the swimming velocity of the SHC sperm-micromotors continuously decreased as shown in **Figure 6.3c**.

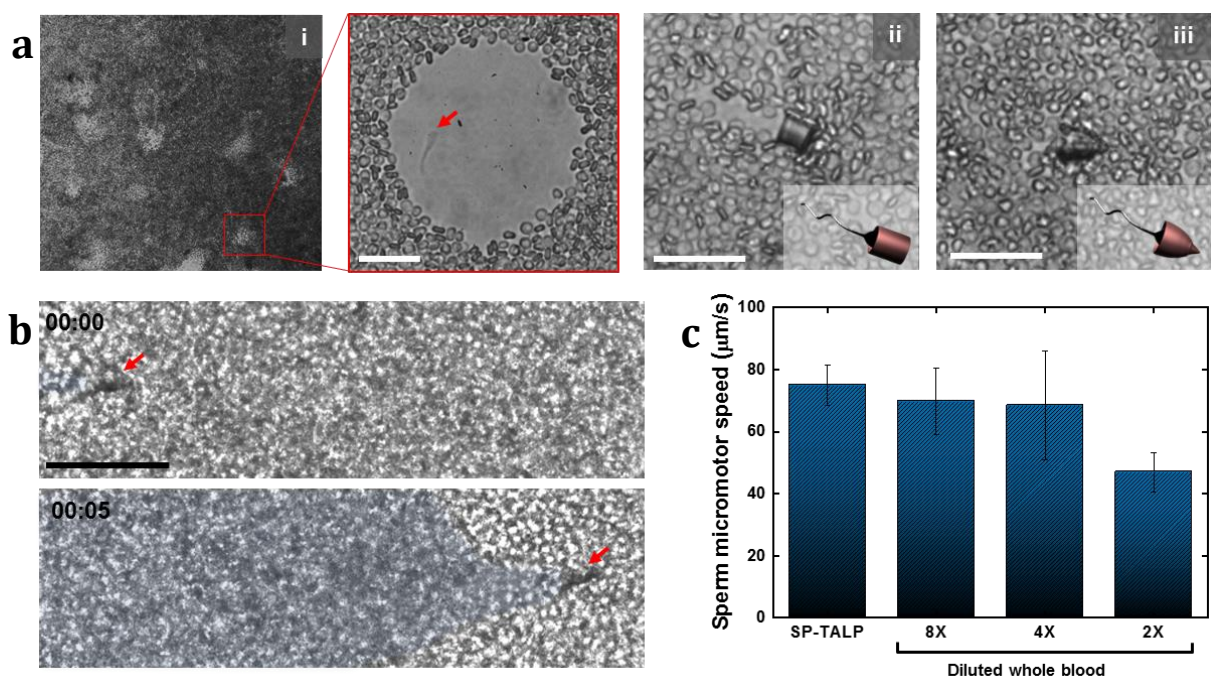


**Figure 6.3.** (a) (i) Free sperm moving in 8× diluted blood; Sperm-micromotors with (ii) a tubular and (iii) a SHC cap in static 8× blood solution. (b) Image sequence of a SHC sperm-motor moving in static 2× blood. Transparent blue region indicates the wake flow resulting from their motion. (c) Speed comparison of SHC sperm-micromotors varying with the dilution of whole blood and sperm medium.  $n=4$ . Scale bars: 40  $\mu\text{m}$ .

## 6.4. Swimming against blood flow

Some of the barriers that micromotors have to face to operate in the blood stream are the high flow rates and the presence of a large number of cells. The physiological blood linear velocity in microcirculation (particularly in the venules) is ca. 0.4 mm/s.<sup>158</sup> This number decreases to ca. 0.15 mm/s at disease sites when suffering for example embolism.<sup>159,160</sup> Thus, micromotors have to overcome the hitting of blood cells and the resistance from the serum flow at a high velocity. To investigate the swimming capability of SHC sperm-micromotors, we used PDMS microfluidic chips to mimic blood vessels of ca. 100  $\mu\text{m}$  in diameter and

imposed a continuous or pulsatile flow using a syringe pump for the experiments. Firstly, sperm-micromotors were introduced into the microfluidic channel containing 2× diluted blood under a flow velocity of 0.167 mm/s to verify their magnetic response and the possibility to guide them in such complex conditions (**Figure 6.4a**). Then, by maintaining the permanent magnetic field at a fixed orientation along the microchannel, and keeping the flow velocity at 0.167 mm/s, we evaluated the rheotaxis capability of the sperm-cap assembly. Positively, we observed a similar behavior of the sperm-micromotors swimming against the flow as compared to free swimming sperm, when keeping their orientation upstream using an external magnetic field. In the natural case, sperm reorient in fluid flow to align against the flow direction and swim upstream through the oviduct channel. This process is still not well understood and there are contradictory hypotheses where rheotaxis is explained as a purely physical phenomena, or as an active process where the fluid flow is sensed by sperm mechanosensitive channels. Recent studies suggest that no significant difference exists in both flagellar beating and released  $\text{Ca}^{2+}$  ions between rheotaxis and freely swimming sperm, indicating that it is mainly a hydrodynamic effect between the sperm flagellum and its surrounding fluid flow.<sup>161</sup> Based on our experiments, the same concept applies to the sperm-micromotor, probably because the flagellar beating of the coupled sperm is not affected by the cap as it was designed with a large opening and size which fits to the sperm head, allowing for full amplitude sperm beating (**Figure 6.4b**).

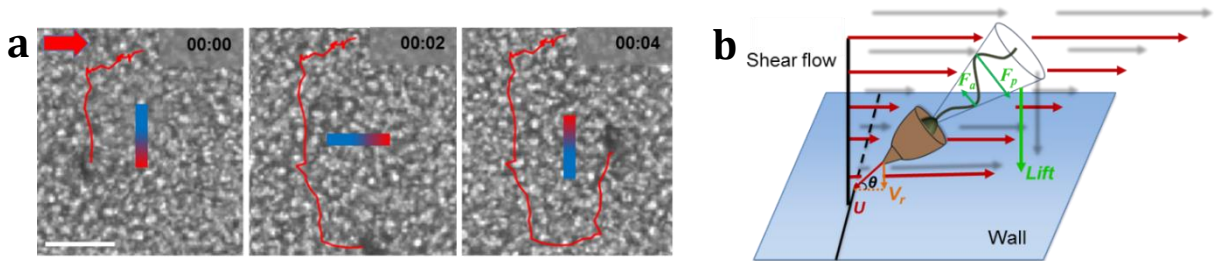


**Figure 6.4.** (a) Magnetic guidance of a SHC sperm-micromotor swimming against blood flow at a velocity of 0.167 mm/s. Scale bar: 40  $\mu\text{m}$ . (b) Rheotaxis of the sperm-micromotor. Chiral beating and imbalance of hydrodynamic force on posterior ( $F_p$ ) and anterior flagellum ( $F_a$ ),



if  $F_p > F_a$ , a net lift force is generated on the flagellum, perpendicular to the flow direction. The lift force provides the sperm-micromotor a rheotactic velocity ( $V_r$ ) toward the wall, leading to a total swimming speed ( $U$ ) at an angle ( $\theta$ ) to the horizontal direction.

By increasing the fluid velocity, sperm-micromotors also lower their rheotaxis speed until reaching a critical blood flow velocity where the speed of the sperm-micromotor decreases down to 0  $\mu\text{m/s}$ . If the blood flow velocity exceeds the tolerance limit of the sperm-micromotor speed, the sperm is not able to swim further and instead is dragged into the direction of the blood flow (see **Figure 6.5a**). **Figure 6.5b, i** depicts the absolute sperm-micromotor speed as a function of the blood velocity. When the sperm-micromotor speed decreases down to 0  $\mu\text{m/s}$ , the flow velocity is around 0.175 mm/s, indicating that the rheotactic speed equals the flow velocity. This value is higher than the swimming speed in static blood due to the wall stress shear gradient which facilitates the progression of sperm even though the volume flow in the blood vessel is much higher than the natural sperm swimming speed. Sperm can also generate stronger thrust force in the presence of a load (fluid resistance), as previously reported for flagellated *Chlamydomonas cells*.<sup>162</sup> Additionally, sperm-micromotors are expected to swim even against higher flow velocities when using channels with larger cross sections. However, in our experiments we used 100  $\mu\text{m}$  channels to avoid difficulties visualizing and tracking sperm-micromotors through the dense blood cells. To explore the influence of continuously changing flow velocity on the swimming performance of sperm-micromotors, we defined a sequence of linearly increasing flow rates by using a syringe pump over a time period of 80 s, increasing the flow velocity up to the maximum and decreasing it again to the original value. As anticipated, the sperm-micromotor moves forward at decreasing speeds upon the increase of the flow velocity (**Figure 6.5b, (ii)**). Then, after reaching the threshold flow velocity, the sperm thrust force cannot overcome the fluid drag force, and the sperm-micromotor is displaced along with the fluid into the direction of the flow. If the flow decreases again, the sperm-micromotor recovers its speed but with a slightly lower magnitude, probably due to the sperm energy consumption over time and the previously imposed flow load.



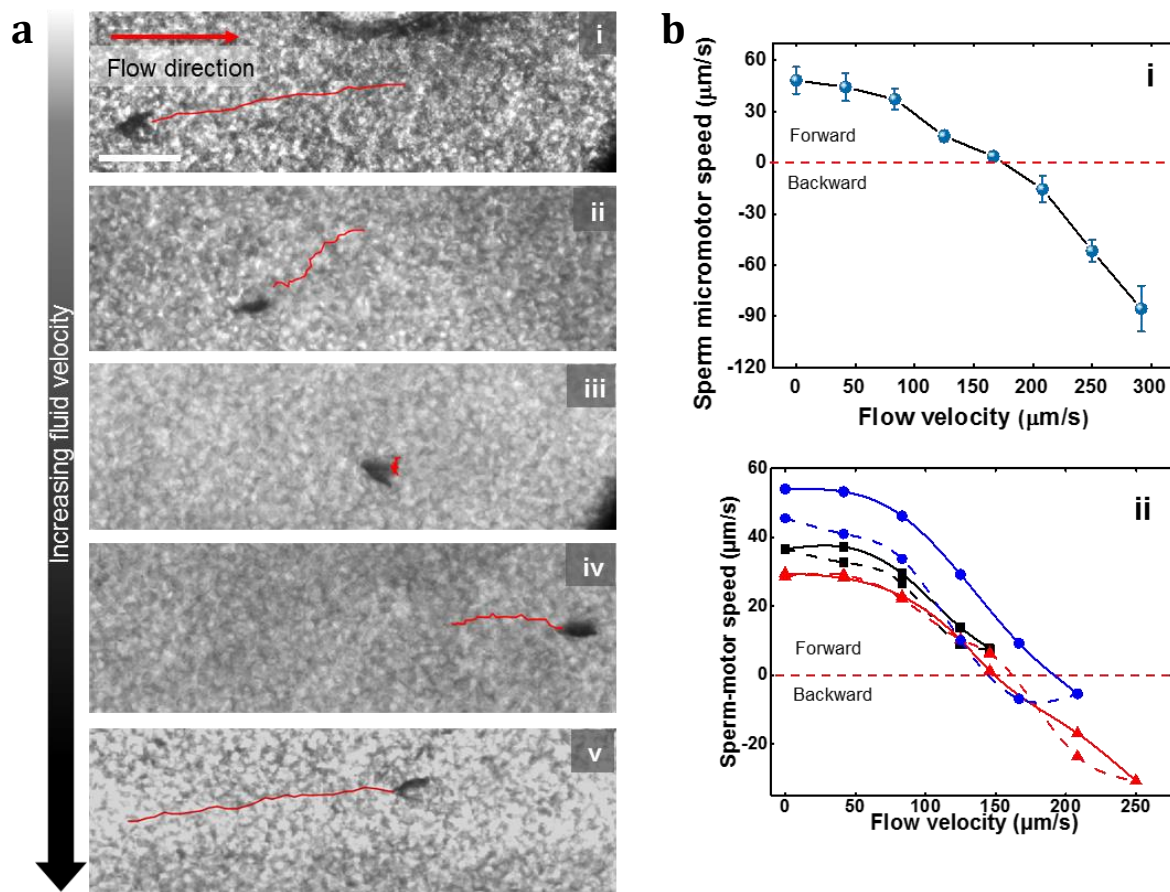


**Figure 6.5.** (a) Track of SHC sperm-micromotors against flowing blood at a velocity of (i) 0.042; (ii) 0.125; (iii) 0.167; (iv) 0.208; (v) 0.292 mm/s. The duration of the tracking in all cases was 3 s. Scale bar: 40  $\mu\text{m}$ . (b) Absolute swimming speed of SHC sperm-micromotors versus blood flow velocity. (i) Sperm-micromotor speed against varying flow velocity ( $n = 4$ ); (ii) Hysteresis loops of speeds of three sperm-micromotors swimming against continuously changing blood flow.

Blood circulation in the human body is mainly caused by two powerful driving forces: the heart beat for arterial ejection,<sup>163</sup> and the muscle pump for venous and capillary returns.<sup>164</sup> The periodicity of the muscle pump depends on the rhythm of the muscular movement. In view of this, we programmed the pulsing perfusions to observe the adaptability of the sperm-micromotor in periodically changing blood flow. We set the impulse cycle as 3 s to mimic the

rhythm of blood return by the respiratory muscle pump under quiet breathing conditions.<sup>165</sup>

**Figure 6.6a, i** shows the forward displacement when the sperm-micromotors swim against pulsing blood flow at a velocity of 0.125 mm/s. In 8 cycles of perfusions (24 s), the sperm-micromotors progressed forward over a distance of about  $596 \pm 43 \mu\text{m}$  in total. The increasing displacement fluctuated with the pace of the perfusing pulsation. We also programmed a stronger pulsing flow at 0.208 mm/s. Although the sperm-micromotor could barely progress forward when the perfusion was on, it could still speed up very fast and continue moving in between two perfusions (**Figure 6.6a, (ii)**). Moreover, we found a ratchet brake mechanism that could help the sperm-micromotor swim against higher pulsing flows. In this case, the sperm-micromotors were first guided towards the wall and forced to constantly swim near the substrate. Due to the preference of the sperm to move near surfaces, also called thigmotaxis, the sperm-micromotor can swim forward parallel to the substrate when the flow is off. When the flow is on, the sperm starts swimming against it (rheotaxis) until the flow rate reaches the threshold value in which the sperm is not able to swim forward (see **Figure 6.6b**). After that, the sperm is not able to hold its head upstream, thus it is necessary to reorient it by the magnetic field, until the horn in the engineered cap is in contact with the channel surface, serving as an anchor. When the flow decreases again, the sperm-micromotor recovers its swimming speed and successfully progresses until the next flow peak is reached. As depicted in **Figure 6.6b, iii**, the flow impact was at that moment counterbalanced by the induced static friction between the top horn of the sperm-micromotor and the substrate. With this mechanism, sperm-micromotors could even resist high flow velocities (up to 0.833 mm/s) and still recover to swim forward when the perfusion was off.

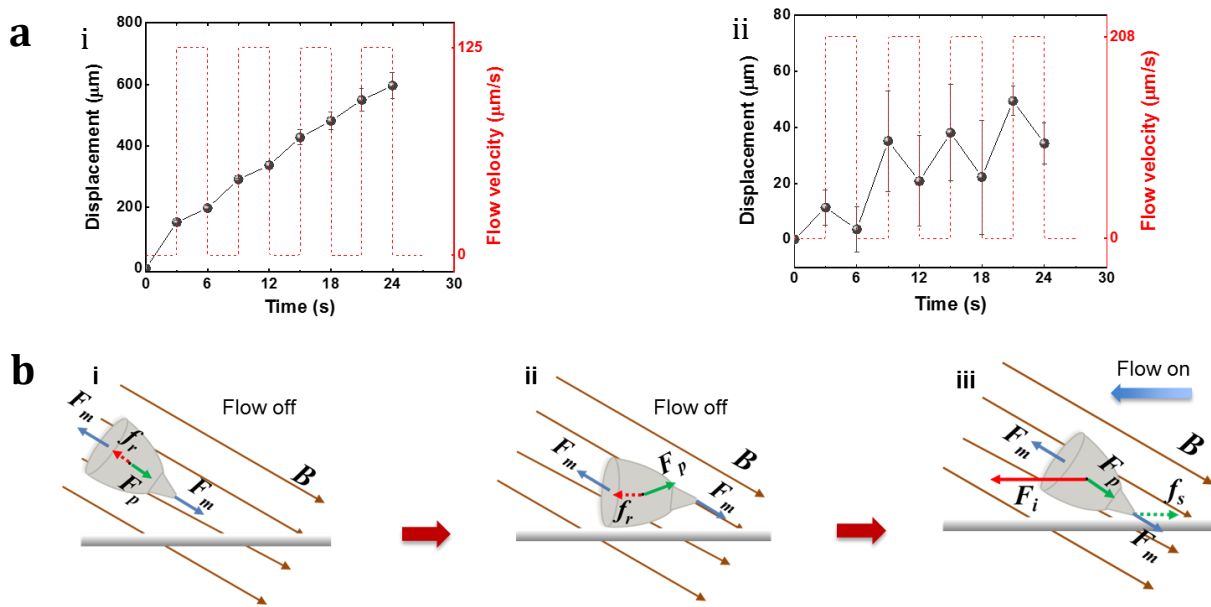


**Figure 6.6.** (a) SHC sperm-micromotor swimming against pulsing blood flow at (i) 0.125 mm/s; (ii) 0.208 mm/s. ( $n = 4$ ). (b) Schematic of the ratchet brake mechanism: (i) Guiding the sperm-micromotor toward the substrate; (ii). Sperm-micromotor swimming without flow; (iii) Ratchet brake against flow.  $F_m$ : magnetic torque.  $F_p$ : sperm propulsion.  $f_r$ : hydrodynamic resistance.  $F_i$ : blood flow impact.  $f_s$ : static friction.

## 6.5. SHC sperm-motor for anti-coagulation application.

As a primary demonstration of the potential application of the sperm-micromotor for a chemical medication in blood, we endowed the sperm-micromotor with an anti-coagulation ability. Heparin-loaded liposomes were prepared by extrusion (see details in **Section 3.6**) and covalently immobilized onto SHCs by an EDC/NHS catalytic reaction. In order to characterize the loading of heparin within the liposomes, Alexa 488-conjugated heparin was used as payload, thus a high fluorescence intensity was detected throughout the liposomes-functionalized SHCs, indicating an intact immobilization compared to the bare SHCs (**Figure 6.7a**). The SEM images in **Figure 6.7b** illustrate the distribution and density of liposomes on

the SHCs. The size of the liposomes varies from 30 to 150 nm. Since a 100 nm pore size filter membrane was used to control the liposome sizes, the larger liposomes probably originated from liposome fusion during the drying process.<sup>84,166</sup> As illustrated in **Figure 6.7c**, along with the increase of the liposome concentration, more and more liposomes are immobilized into densely packed arrays on the micromotor surface.

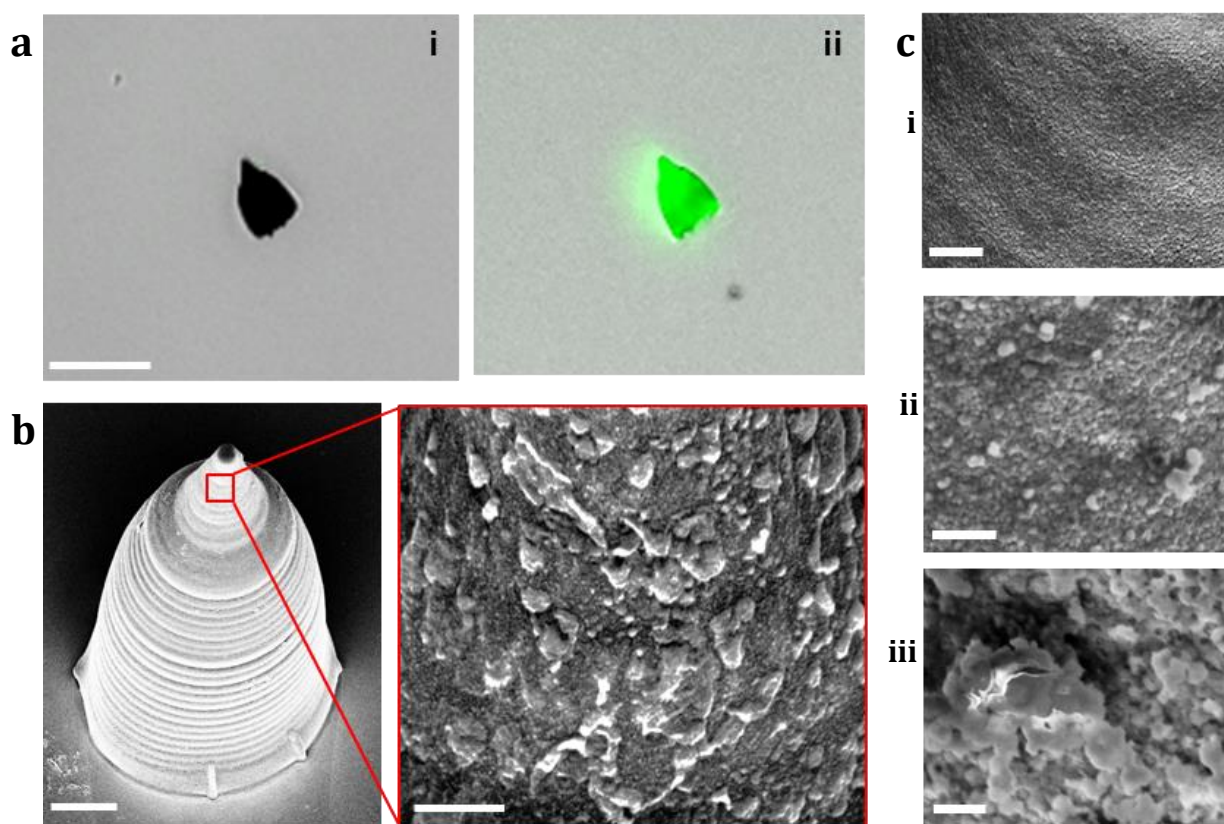


**Figure 6.7.** (a) Fluorescence microscopy images of (i) blank SHC (ii) Alexa 488-Heparin loaded liposomes immobilized HSC. Scale bar: 20  $\mu\text{m}$ . (b) SEM of HSC immobilized with Heparin-loaded liposomes (50  $\mu\text{M}$ ). Scale bars: 3  $\mu\text{m}$  and 300 nm in the magnified image. (c) SEM images of SHCs immobilized with different concentrations of liposomes. (i) Bare SHCs. (ii) 100  $\mu\text{M}$ . (iii) 200  $\mu\text{M}$ . Scale bars: 200 nm.

After washing and drying, we re-dispersed the heparin-loaded liposomes, immobilized SHCs (HLSs) in PBS and evaluated the anti-coagulation efficiency of the HLS sperm-micromotor system by determining the activated clotting time (ACT). Noticing the considerable burst release effect (45),<sup>167</sup> we only re-dispersed the HLSs in PBS right before used. After activation with thrombin, the free-swimming sperm-treated group showed a comparable clotting time ( $95 \pm 26$  s) to the blank control of 2× diluted whole blood ( $85 \pm 18$  s). Bare SHCs ( $75 \pm 26$  s) did not show a significant influence on the blood clotting, either, presumably because of the bio-compatible cap coating. No clotting was found in the HLS sperm-micromotor system even after 5 min, demonstrating a high anti-coagulation capability provided by the released heparin. Because of medium evaporation, we did not observe the samples for longer times. **Figure 6.8a** illustrates 8× diluted blood samples differently treated with the HLS sperm-micromotors and the bare SHC sperm-micromotors in microfluidic channels. After 5 min activation, blood samples including bare SHC sperm-micromotors had already been found with fibrin clots, while the samples treated with HLS sperm-micromotors were still clean with well dispersed single blood cells throughout. Furthermore, a whole blood incubation assay was implemented to quantitatively analyze the anti-coagulant activity of HLS sperm-micromotors in human blood. Prothrombin fragment F1+2<sup>168</sup> and integrin CD11b,<sup>169</sup> as markers of the coagulation cascade and granulocyte activation processes, respectively, were determined to evaluate the coagulation and inflammation levels of the treated blood. As shown in **Figure 6.8b** and **c**, the sperm-motors induced the lowest F1+2 concentration, while the bare SHCs and sperm samples did not deviate from the blank blood. All groups had commensurate counts of CD11b, which showed that both the SHCs and the sperm did not induce any obvious innate inflammatory response. The significantly lower level of hemostasis activation in the HLS sperm-micromotors group reflected a valuable heparin-induced anti-coagulation effect. Despite the fact that more detailed studies are still needed to push forward this effort to application, for instance studies on the encapsulating efficiency and stability of the liposomes, our results open up a potential application of micromotors towards the protection of the circulatory system from blood clot formation. In this scenario, HLS sperm-micromotors would be propelled and guided near the embolism sites, suppress the hemostasis activation by releasing heparin gradually into the environment and

consequently prevent further blood clots. In the future, this system could be further expanded to load various thrombolytic drugs for the therapy of already formed thrombus.

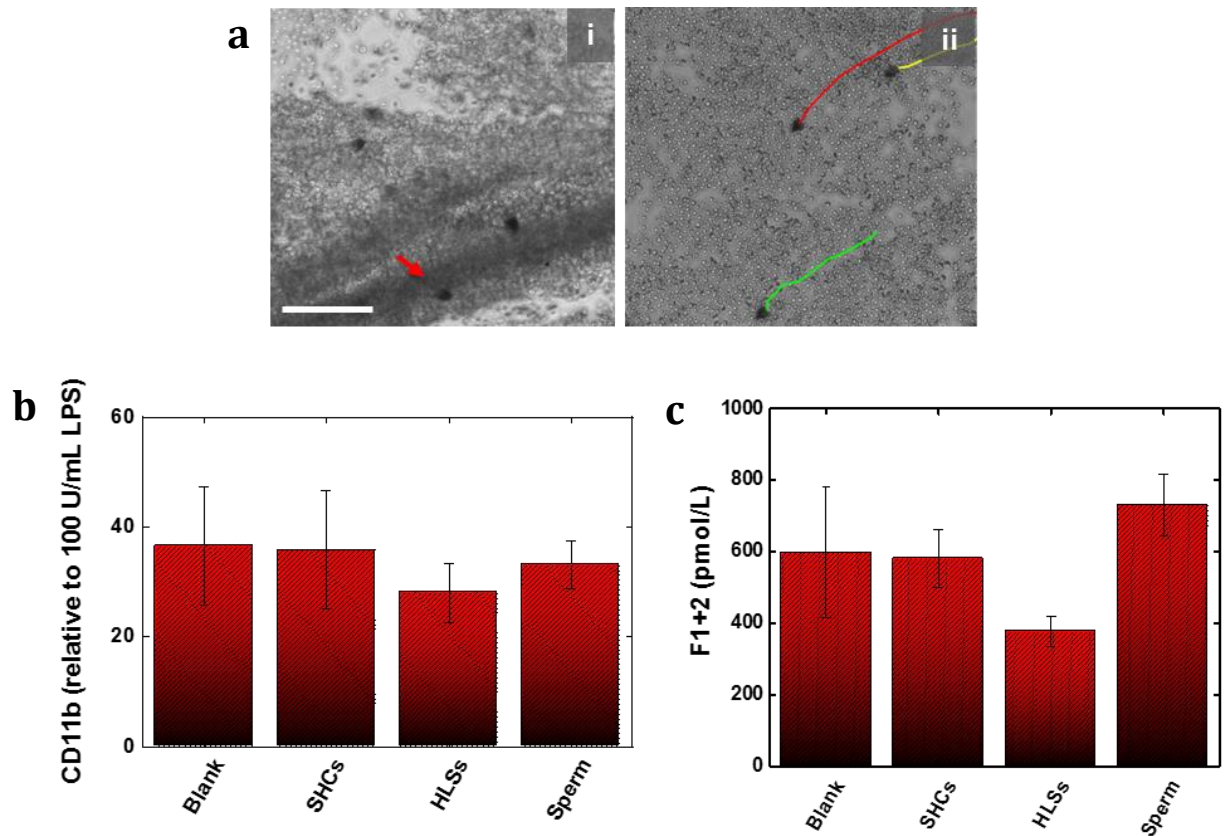


**Figure 6.8.** (a) Activated clotting of the blood treated with (i) bare SHC sperm-micromotors and (ii) HLS sperm-micromotors. Red arrow points at fibrin clot. Scale bar: 100  $\mu$ m. (b) CD11b level indicating coagulation cascade activation. (n = 6). (c) F1+2 level indicating granulocyte activation. (n = 6).

## 6.6. Summary

To summarize, we developed a blood adapted sperm-motor which could efficiently swim against blood flow comparable to the real blood stream in human body. This streamline-horned sperm-motors were able to work not only as individuals, but also as swarms to execute missions in flowing blood. The functionalized sperm-motors showed a significant anti-coagulant effect while the non-functionalized sperm-motors did not. The immobilized liposomes are also open for further functionalizations, for example with thermal-sensitive<sup>17038</sup> shells, or functional groups sensitive to activated coagulation factors<sup>168</sup> toward triggered release or specific targeting.



## 7. Transport of multiple motile sperm cells

### 7.1. Background

**Chapter 4, 5** and **6** have presented tetrapod-like, streamlined and SHC sperm-motors for the applications in both oviduct and the blood. However, all of these three were only for single sperm transport. In the drug delivery application, the sperm amount directly determines the drug dosage and the anticancer efficiency. The need of multiple sperm guidance can be also extended to the in vivo fertilization process, as the success rate is highly dependent on the amount of sperm that reach the fertilization site. Such an inefficient way of transporting the sperm one by one challenges both the surgical operability and the patient tolerance. Hence, it is necessary to establish strategies for collective sperm transport for the future applications in reality. Meanwhile, sperm, as a type of live cells, are extremely sensitive to the environment. Especially the motility and mobility can be largely decreased if the surrounding composition changes or the flagellum is damaged physically. The strategies therefore should have no toxicity and avoid direct contact with the sperm.

### 7.2. Self-assembled train-like sperm-motors swarm

This section is based on the publication titled: Sperm Micromotors for Cargo Delivery through Flowing Blood. Reprinted with permission from [ACS nano, 2020, 14(3), 2982-2993] ([doi.org/10.1021/acsnano.9b07851](https://doi.org/10.1021/acsnano.9b07851)). Copyright [2020] American Chemical Society.

Sperm-motors with specific design can assemble into a train-like structure under the asymmetric magnetization by an external magnetic field, facilitating enhanced transport for both multiple sperm and multiple functional microstructures. This section presents an example of the assembly of SHCs shown in **Chapter 6**. The asymmetric magnetization relies on partial magnetic coating achieved by depositing Fe at a 75° angle (details are given in **Section 3.1**). **Figure 7.1a** shows a schematic of the SHCs assembling into a sperm-train.



When a uniform magnetic field is applied across the sample with randomly dispersed SHCs and sperm, the magnetic layer on each SHC acquires a dipole configuration, leading to the alignment of SHCs along the direction of the magnetic field. The dipole-dipole based long-range attraction between two different SHCs results in their self-assembly. **Figure 7.1b** shows the change of the magnetic field distribution from a single SHC to a 4-SHC sperm-train. A more stable field distribution is found after the assembling process, mainly caused by the horn of the caps as anchor points within the sperm train. The assembled “train” can be further prolonged, stretched and organized with more and more SHCs involved under the alignment of the magnetic field (see **Figure 7.1c**), similar to the assembling process of previously reported microcubes.<sup>171</sup> The assembling of SHCs can be improved even more by decreasing the distance between them (by stirring or by increasing the density of caps in the solution).

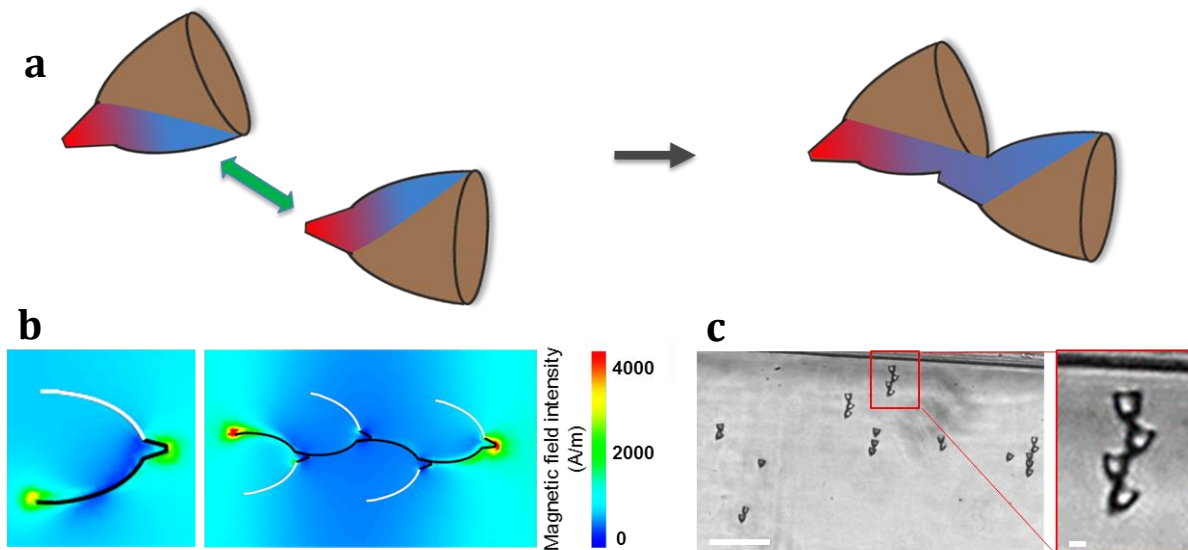


**Figure 7.1.** Magnetic assembly of SHCs. (a) Schematic of the assembling of two SHCs under magnetic field. (b) Magnetization simulations of a SHC and a 4-SHC sperm-train, both with partial iron coating. The metal coated part is colored in black. (c) A sperm-train swimming in sperm medium (SP-TALP). Red arrows point at the sperm heads. Scale bar: 100  $\mu\text{m}$ .

**Figure 7.2a** shows a sperm-train with 9 SHCs and 7 sperm. The SHCs are periodically arranged into opposite directions of the sperm-train, which ensures that the beating of the sperm flagellum in one SHC is not disturbed by another, also facilitating the sperm coupling to the structures. During the guidance, the sperm-train is still capable to assemble with other sperm-trains, breeding a new longer sperm-train but with a lower swimming speed. Finally, when the sperm-train arrives at the desired position, we can easily trigger the coupled sperm to escape by repeatedly flipping the SHCs and disassembling the sperm-train by abruptly turning the magnetic field. In this way, the SHCs are precisely transported and accumulated at the desired position.

This adjustable sperm-train with flexible structure can surprisingly adapt to the swimming environment in blood. 4× diluted whole blood was used as a model environment to verify its swimming performance for further blood application. As shown in **Figure 7.2b**, various sperm-trains with different numbers of SHCs are assembled and swim in static blood fluid. The guidance can be performed not only on a single sperm-train, but also on a troop of collective sperm-trains and sperm-micromotors. The swimming performance of sperm-trains in static blood solution is depicted in **Figure 7.2c**. The average swimming speed generally decreases with the increase of the SHCs numbers in sperm-trains. The cap number dependent swimming performance shows the same behavior when the sperm-trains swim against flow. For example, as tracked in **Figure 7.2d**, the average swimming speed of a 4-SHCs sperm-train against a blood flow of 63  $\mu\text{m/s}$  was 32  $\mu\text{m/s}$ , while a single SHC sperm-micromotor could swim at a high speed of 97  $\mu\text{m/s}$ . This speed decreases is probably because sperm are not pushing the cargoes in a synchronized way. The interference between the traveling waves generated by the tail beating of the coupled sperm as well as the increased load (caps number) also could influence the resulting swimming speed. In order to get a better understanding of the interaction between sperm micromotors within a sperm-train, further modeling and experiments are required.

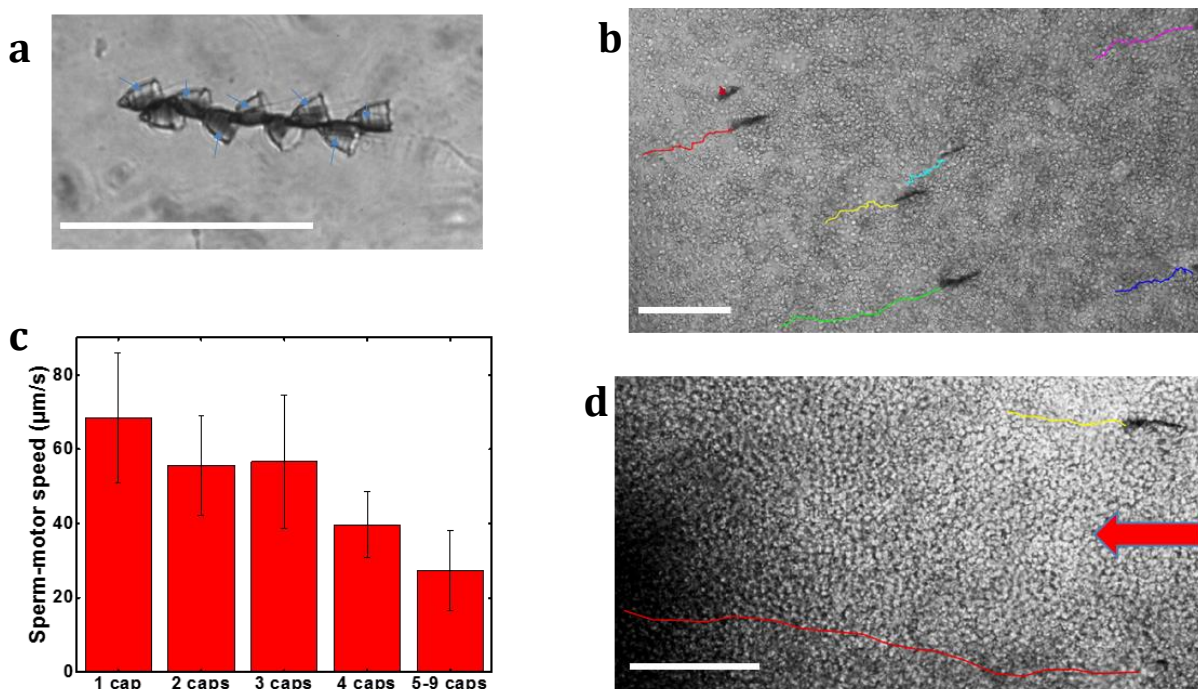


**Figure 7.2.** (a) A sperm-train swimming in sperm medium (SP-TALP). Blue arrows point at the sperm heads. (b) A troop of sperm-trains swimming in 4 $\times$  diluted blood. (c) Swimming speed of sperm-trains vs cap number. (n = 6). (d) Track of a sperm-train and a SHC sperm-micromotor swimming against flowing blood. Scale bars: 100  $\mu\text{m}$ .

### 7.3. Helical microcourier combined with a protein-based microflake

This chapter is based on the publication titled: Magnetic Micromotors for Multiple Motile Sperm Cells Capture, Transport, and Enzymatic Release. Reprinted with permission from [Angewandte Chemie, 2020, 59, 2-11] ([doi.org/10.1002/anie.202005657](https://doi.org/10.1002/anie.202005657)). Copyright [2020] WILEY-VCH.

This chapter Magnetically driven micromotors are of great interest because of their fuel-free actuation and controllable locomotion based on external magnetic field which can efficiently

penetrate tissue without inducing adverse effects.<sup>172</sup> Compared to those based on translational actuation by magnetic field gradient, micromotors based on oscillating or rotating magnetic fields only need very low field strength,<sup>50,173</sup> making them safer and more adaptable in human body. Indeed, helical microstructures were proposed to transduce the rotational actuation achieved from the rotating magnetic field into translational motion.<sup>51</sup> Nelson et al. demonstrated that helical micromotors could be propelled by orthogonal rotating magnetic field in a wide range of frequencies and furthermore be used for drug delivery targeting single cells.<sup>52</sup> Helical micromotors could also be used to manipulate micro-objects by direct contact pushing<sup>174</sup> or by locally induced hydrodynamic vortexes, as a more gentle way. For example, helical micromotors with a tubular front end were shown to be able to create mobile fluidic traps to capture microbeads without contact and deliver them to the desired location under a rotating magnetic field, showing a great potential on the transport of delicate cargos.<sup>175</sup>

One example of the cargos that need the special care from micromotors is the sperm. However, carrying motile cells represent a big challenge, in particular if the purpose is to transport and deliver multiple sperm to the area of interest. In the *in vivo* fertilization process, the success rate highly depends on the sperm amount. It has been found that a successful fertilization *in vivo* needs at least tens to hundreds of sperm to reach the oocyte.<sup>176</sup> In this process, interindividual cooperation among the sperm facilitates the locomotion and the sperm penetration through the cumulus cells and the zona-pellucid.<sup>177</sup> As well, in the drug delivery application, the sperm amount directly determines the drug dosage and the anticancer efficiency of the treatment. Such an inefficient way of transporting the sperm one by one challenges both the surgical operability and the patient tolerance to the treatment. Hence, a harmless micromotor that can transport collective motile sperm with no effect on their propulsion is needed. While the collection of immotile sperm can be done by simply mechanically trapping, a more robust method with a firm binding mechanism must be employed to collect motile sperm given the powerful propulsion of the sperm. In the clinical practice of *in vitro* fertilization, solid-state hyaluronic acid (HA) is widely used for sperm selection based on a receptor mediated coupling.<sup>178</sup> This method is crucial on the selection of healthy sperm as only sperm with intact DNA can successfully express this protein. The

binding neither influences the sperm activity nor the tail beating and thus the HA bound sperm can be safely used on fertilization.<sup>179</sup> Inspiringly, the dramatic interaction between HA and sperm can be employed in the research of micromotors for sperm transport. In this chapter, we present a magnetically driven microcourier (MC) that can efficiently transport sperm clusters, including both motile and immotile ones. The collection of motile sperm relies on a microflake (MF) made of bovine serum albumin (BSA) and HA (**Figure 7.3**). Motile sperm then are co-incubated with the HA microflakes, inducing their coupling by ligand-receptor binding between sperm and HA. Once the sperm are trapped within the microflake, a magnetic helical micromotor is approached to the microflake, capturing it due to a locally induced hydrodynamic vortex. After being precisely guided to the target zone, the sperm can be controllably released by hydrolyzing the microflake mediated by the proteases present in the surrounding environment. In the scenario of the application in the reproductive system, several proteases, for example Oviductin ( $\sim 10 \mu\text{g/mL}$  present in the oviduct),<sup>180</sup> will serve as the enzymatic trigger to catalyze the hydrolysis of the microflake. Here in this study, we employ trypsin at concentrations ranging from 50 to 200  $\mu\text{g/mL}$  to demonstrate the principle of operation.

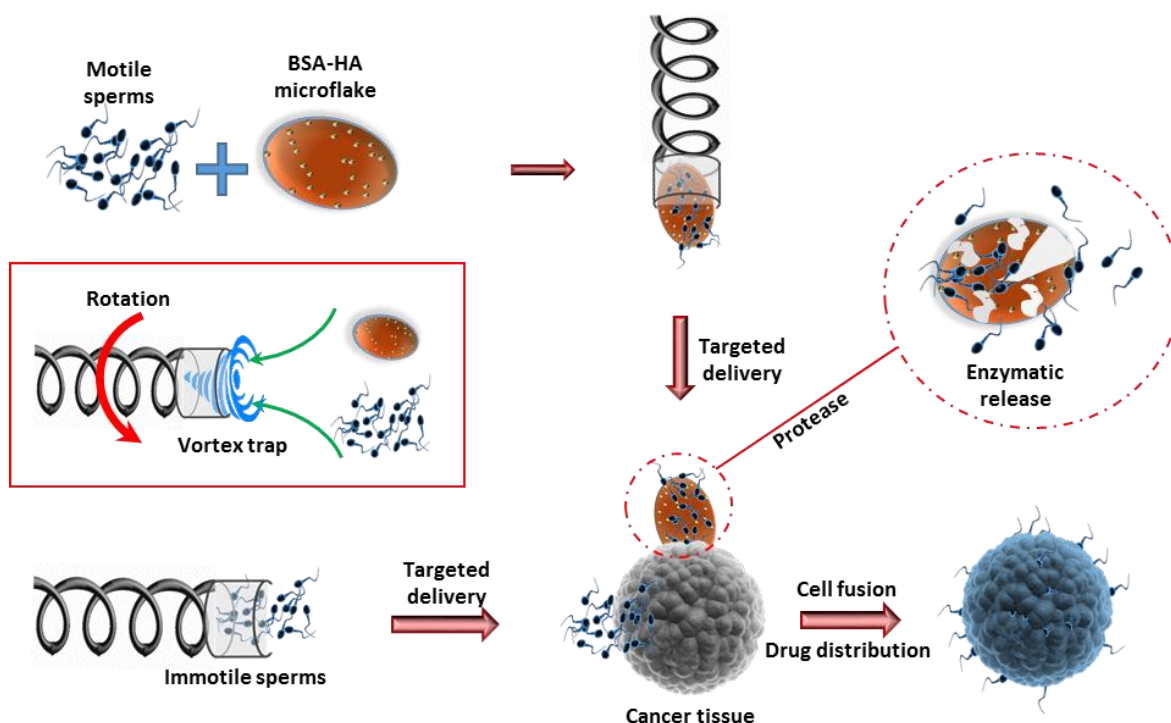


**Figure 7.3.** Concept of the transport of a cluster of motile sperm by the MC-MF system

The MC has a helical body and a tubular head. The helical body was designed as a single-threaded screw with a length of 100  $\mu\text{m}$  and a diameter of 50  $\mu\text{m}$ . It was constructed layer-by-layer in a shape of spiral stairs. Each structural line was exposed horizontally to enhance the mechanical stability of the structure. The tubular head was designed as the confinement for the target cargo with the same diameter of the helical body. Three prototypes (MC1, MC2 and MC3 as shown in **Figure 7.4a**) were fabricated by FSTL, with different mechanisms for cargo capture. The MCs were coated with 15 nm Fe and 2 nm Ti respectively as magnetic and biocompatible layers. When the helical body rotated synchronously with the external magnetic field, it converted rotational motion to translational motion. The MCs could be furthermore guided by changing the rotating direction of the field. Different MCs had no significant difference on the swimming velocity or the guidance performance. Therefore we used MC3 as an example to show the swimming performance the MCs under magnetic guidance. **Figure 7.4b** illustrates the overlay motion sequence of a MC under magnetic

guidance. A rough rectangular guidance was performed, reflecting a stable swimming behavior of the MC and its fine synchronization with the magnetic field. As shown in **Figure 7.4c**, the swimming performance of the MC was highly influenced by the strength and the rotating frequency of the applied magnetic field. From 0 to 4 Hz, the MC responded to the magnetic field with chaotic vibration. After the rotation reached the actuation frequency, the forward velocity of the MC almost linearly increased with the increase of the rotating frequency of the magnetic field until the rotating frequency reached a so-called step-out frequency. After that, the MC velocity declined rapidly as it was not able to synchronize with the input frequency. Higher field strength could elevate the step-out frequency and therefore increase the peak value of the forward velocity. Compared to the previously reported helical micromotors with smaller sizes, our MC generated higher swimming velocities with lower magnetic field strength and lower frequency. This is attributed to the efficient magnetic response and the high synchronization of the big MC with thicker Fe coating to the magnetic field.

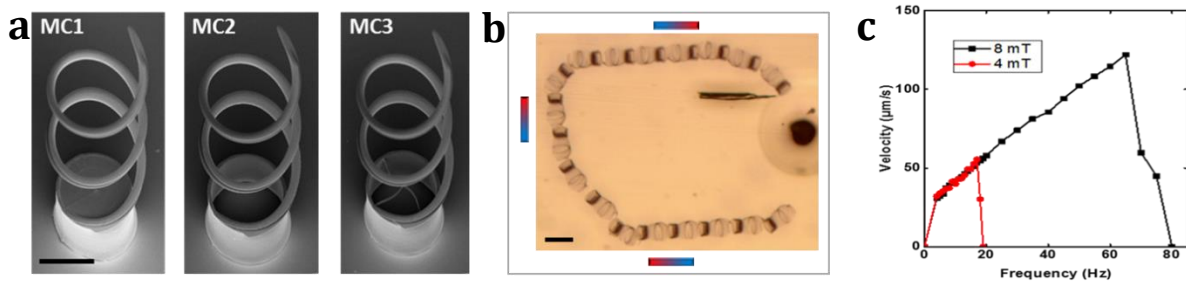


**Figure 7.4.** Swimming performance of MCs. (a) SEM images of 3 microcouriers. Scale bar: 50  $\mu\text{m}$ . (b) Swimming velocity of MC3 related to the rotating frequency of the magnetic field. Scale bar: 200  $\mu\text{m}$ . (c) Motion sequence of MC3 guided in a rectangular track.

The difference of three types of MCs is manifested in the sperm capturing. We first tested MC1 with a cup-like head (**Figure 7.4a**), which was previously reported to transport cargos based on direct contact pushing. Disappointingly, the cargo capturing rate of MC1 was very

low as the fluid flow created by MC1 always pushed the cargo away. As an improvement, MC2 was fabricated with a tube on top of its helical body (**Figure 7.4a**). The cargo coupling relies on a microvortex based noncontact transport, as previously demonstrated by Nelson et al.<sup>175</sup> When MC2 rotated by the magnetic field and swam forward, the rotary motion of the propeller could create a vortex in front of the head. Confined by the tubular head, the vortex could pump the nearby object in when the MC2 moved forward. **Figure 7.5** showed the transport of immotile sperm by MC2. When the MC2 swam near to the immotile sperm, the vortex in front of the tubular head pulled the nearby sperm in the fluid trap. The sperm were confined in the interior of the vortex by the translational suction force and rotated together with the MC. The efficient transport of the cluster of immotile sperm represents a promising non-invasive strategy toward asthenospermia, with which patients can provide sufficient sperm only in reduced motility. On the other hand, for the patients who have motile but reduced amount of sperm, i.e. oligospermia, it is more important to select the healthy sperm and transport to the oocyte.<sup>68</sup> However, the aggressive self-propulsion of motile sperm stays as a barrier for mechanical capturing. While the immotile sperm were efficiently trapped by the fluid vortex, the motile sperm could easily swim away at a high speed. To solve this problem, a sperm-friendly strategy is needed to harmlessly fix the sperm for mechanical capturing and controllably release them after approaching the target.



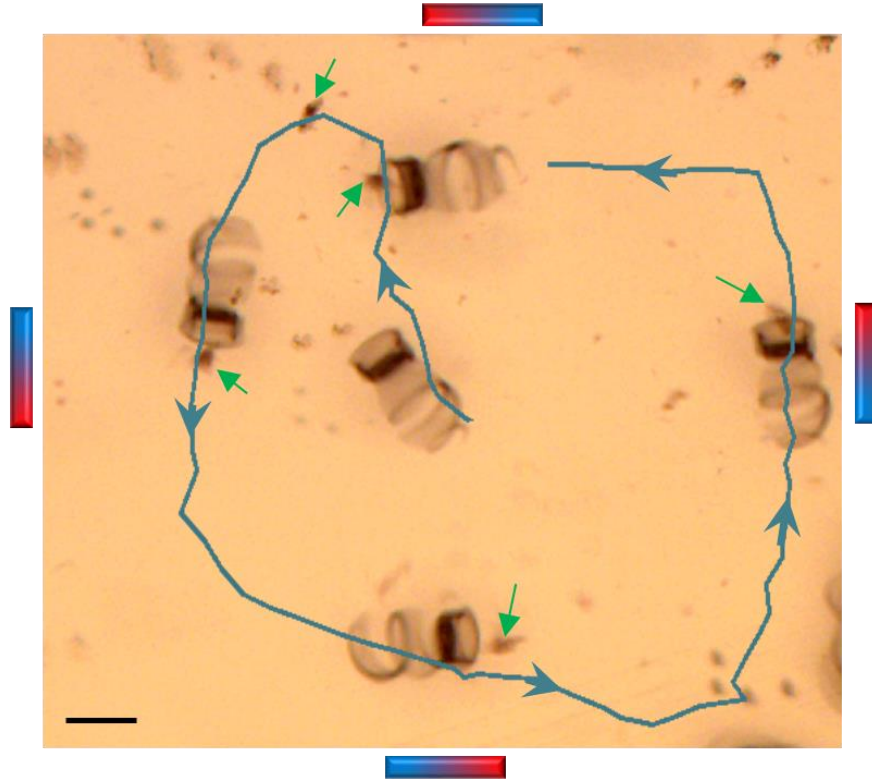


**Figure 7.5.** Overlaid motion sequence of the transport of a cluster of immotile sperm by MC2. Blue line and arrows depict the track of and directions of the MC movement. Green arrows point at the cluster of immotile sperm. Scale bar: 100  $\mu\text{m}$ .

Thermal-assembled BSA/HA microflakes were fabricated to select and carry healthy sperm. We first fabricated HA/BSA microbeads by using a micro-emulsion method. The BSA scaffold was initiated by heating, while the embedded HA microparticles were cross-linked by EDC.<sup>181</sup> After gentle milling at 4 degree, the microflake was prepared with a high surface area for the sperm to bind on. Solid-state HA was using here for its affinity to sperm as they have been extensively used on artificial fertilization thanks to its similar structure to the ligand on zona. The receptor mediated sperm binding to HA occurs specifically on mature sperm with intact genes.<sup>179</sup> Inspired by this, we employed HA particles to capture healthy motile sperm, when the BSA scaffold served to carry the sperm-bound HA particles and release the sperm after hydroxylation. The microflakes were around 80  $\mu\text{m}$  in diameter and 20  $\mu\text{m}$  in thickness.

Each HA particle is around 500 nm in diameter. Low-temperature milling enhanced the roughness of the microflake surface and exposed HA particles on it, generating a high efficiency of sperm capturing on these exposed binding sites. **Figure 7.6a** illustrates the sperm attachment on the microflake. sperm were captured by the microflake by being bound on the front part of the sperm head, revealing an acrosome related reaction. The sperm capturing efficiency was affected by the microflake size, the sperm concentration and incubation time. The microflake at around 80  $\mu\text{m}$  in diameter could averagely capture 50 sperm in 10 min co-incubation. Despite the fact that the sperm capturing was more difficult over time probably due to the repelling of the captured sperm, the sperm attachment could still occur after 30 min when a foreign sperm swam by.

To demonstrate the overall potential of the MC-MF based system for multiple sperm transport, we fabricated a microfluidic chamber as an in vitro environment. Although MC2 could successfully capture single immotile sperm, the BSA-HA microflake repeatedly slipped out of the back opening of the tube. Thereupon, we constructed a cross on the bottom of the tubular head to assist the microflake carrying without affecting the vortex. **Figure 7.6b** illustrated an entire transport process with an operation strategy as follows: First, the microcourier was slowly guided toward the sperm-loaded microflake at a low rotating frequency. If the microcourier approached to the targeted microflake at a high speed, the docking could be easily lost as the trapping force of the vortex declined rapidly outside the tube. When the front opening of microcourier was close to the microflake, the rotating frequency was increased to 20Hz to generate a powerful vortex to trap the microflake and firmly carry it. After the MC-MF reached to targeted position, the cargo discharge was accomplished by simply unscrewing the MC by rotating the magnetic field in the opposite direction at 20 Hz.

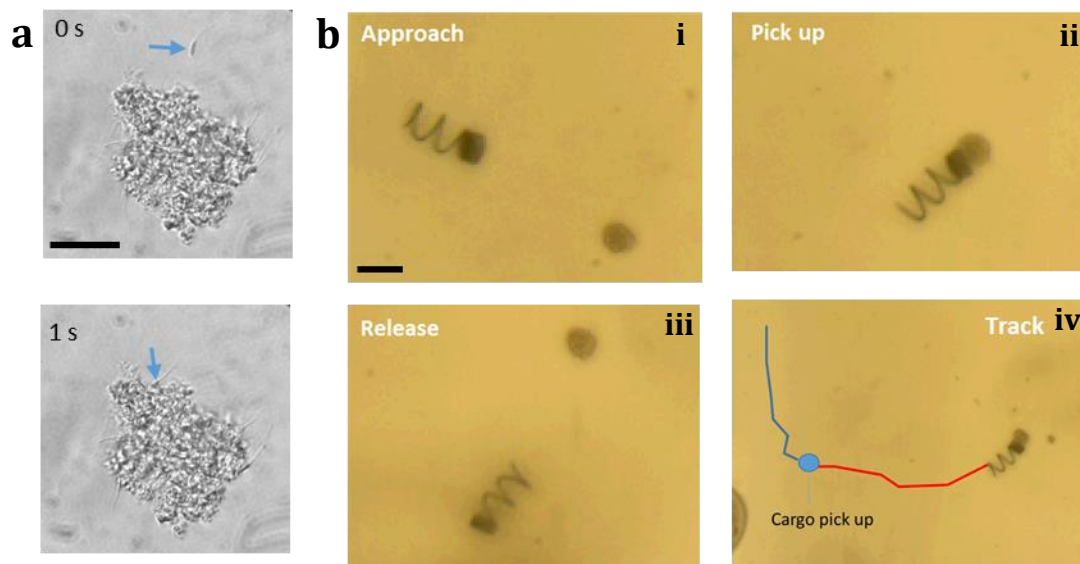


**Figure 7.6.** (a) Sperm capturing by a BSA-HA MF. Red arrows pointed at one sperm before and after being captured. Blue arrows point at a sperm being captured. Scale bar: 50  $\mu\text{m}$ . (b) Transport of a motile sperm loaded MF by MC3: (i) approaching to the MF; (ii) picking the MF up; (iii) releasing the MF; (iv) track of the whole transport. Blue and red lines depict the tracks of the movement before and after picking up the MF. Scale bar: 100  $\mu\text{m}$ .

Finally, the captured sperm were released by enzymatically hydrolyzing the BSA matrix. In general, protein hydrolysis occurs on the peptide linkages.<sup>182</sup> During the preparation of the microflake, the aggregated proteins lose solubility due to an exposure of hydrophobic groups after heating. Meanwhile, the aggregated proteins become more unstable, especially in the presence of protease, as the peptide linkages were also exposed to water.<sup>183,184</sup> We first tested the sperm release in PBS without protease. No sperm was released in 1 h of observation, revealing a stable coupling of sperm on the microflake. Physiologically, proteases are universally present in different organs in human body, while most of them exist as known in the digestive system.<sup>185</sup> Specifically in the female reproductive system, a trypsin-like protease termed “Oviductin” is secreted by the oviduct at a concentration of

around 80  $\mu\text{g/mL}$  for external protein degradation.<sup>186</sup> It plays an important role in the reproductive process, including preventing the oviduct obstruction.<sup>180</sup> Besides, the sperm also release proteases, including the most well-known acrosin, which helps the sperm to penetrate the cumulus and zona pellucida.<sup>187</sup> These proteases facilitates the hydrolysis of foreign proteins, which specifically helps the disintegration of the BSA scaffold in terms of this research. To demonstrate the enzymatic sperm release from microflake, we designed an accelerated experiment by adding trypsin in the system to mimic the function of the proteases in the oviduct. **Figure 7.7a** illustrates the sperm release based on the enzymatic disintegration of the microcourier where the trypsin was used at 100  $\mu\text{g/mL}$ . The microcourier was disintegrated very slowly at the beginning, revealing a diffusion time of the added trypsin and a water repelling effect by the exposed hydrophobic groups. The first sperm was released in the fourth minute. After that, the microcourier was rapidly disintegrated and thus the captured sperm detached from the microcourier separately or in a bundle with their heads attached on the same BSA-HA block. These bundles of sperm could be further released after the attached BSA-HA blocks were completely disintegrated. In the end, all the captured sperm swam away in 10 min. After being released, the sperm retained their mobility and swam away in random motion. As depicted in **Figure 7.7b**, the release rate of sperm declined as trypsin concentration decreased. Considering the lower concentration and the lower proteolytic activity of the protease in the oviduct compared the trypsin we used in this experiment,<sup>188,189</sup> the auto release of sperm in vivo is expected to be gentler than this accelerated experiment. The release time can be further regulated by the crosslinking degree of the BSA. In general, sperm can live for several days in the oviduct. This guarantees the safety and mobility of the released sperm during a wide range of release time.

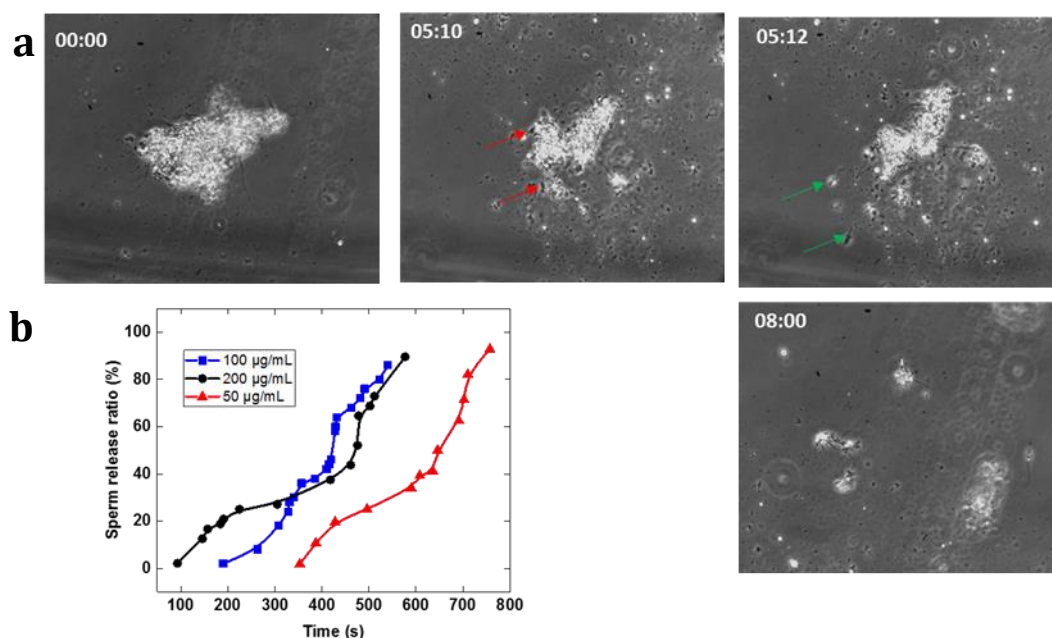


**Figure 7.7.** (a) Phase contrast images showing sperm release during MF hydrolysis by trypsin. (b) Sperm release numbers over time relative to the total captured numbers.

## 7.4. Multi-pocket sperm-bus

Another strategy for multiple sperm transport is to use “multi-pocket sperm-bus”. To do so, a large conical tube was designed containing nine micropockets, allowing multiple mechanically coupled sperm to simultaneously propel the structure forward (**Figure 7.8**). In this experiment, sperm and multi-pocket caps were co-incubated, similarly to the previous experiments in **chapter 5** using smaller microcaps. After a few seconds, multiple sperm entered the individual cavities and pushed the multi-pocket structures forward. The caps were coated with iron to allow their magnetic guidance. Future experiments will focus on optimizing the design of these structures to further reduce drag forces and improve the overall motion efficiency of the sperm-motors. Thus, it is important to consider how the separation and lengths of the cavities might affect the tail beating of the sperm, since external confinement of the sperm can influence the resulting motion, as reported previously by our

group.<sup>69</sup> Additionally, sperm induce traveling waves that can be summed up or cancelled out depending on the position of the different sperm within the multi-pocket cap. Although the sperm release from the sperm-bus remains a problem, the structure itself could serve as a platform for future sperm synchronization studies as well as for investigating the influence of sperm head rotation on the overall motion performance of the bio-hybrid micromotor.

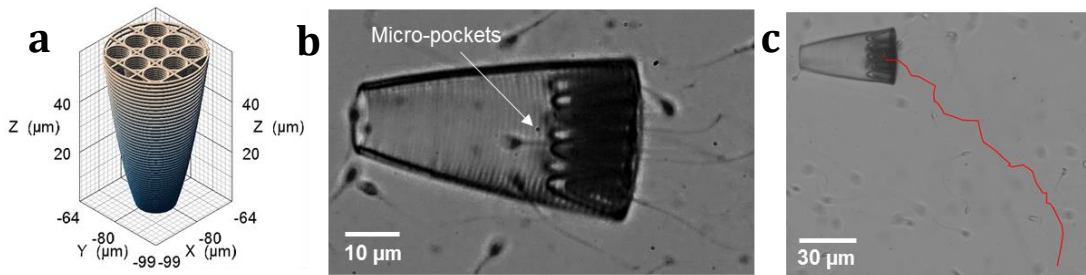


**Figure 7.8.** Sperm-bus for multiple sperm transport. (a) CAD Design. (b) Sperm capturing in the pocket. (c) Track of the movement of the sperm-bus propelled by coupled sperm.

## 7.5. Summary

To summarize, we have demonstrated three robotic systems to transport clusters of sperm. Firstly, the SHC sperm-train represents a self-assembly strategy for multiple single micromotors transport. The sperm-train comprised of multiple single SHC sperm-motors can be guided by external magnetic field one by one and even as a swarm. The streamlined figure enables them to efficiently swim in the blood flow. The train-like assembling and swarming could not only improve the efficiency of cargo transport, but also enable the sperm-motors swarm to swim through narrow capillaries, thanks to the deformable body of the sperm-train. The microcourier-microflake system represents a strategy of concentrated transportation of sensitive cargos. This integrated system is based on an external magnetic field as the power source, a helical micromotor as the courier and a microflake made of BSA

and HA as the sperm container. We demonstrated the magnetic actuation and the remote guidance of the microcourier. The microcourier was optimized to transport not only single dispersed immotile sperm but also the clusters of motile sperm with the assistance of the microflake. While the immotile sperm were released by simply unscrewing the microcourier, release of the motile sperm relied on the enzymatic hydrolysis of the BSA scaffold of the microflake. The MC-MF integrated system presented here can be envisioned to be a new strategy toward non-invasive artificial fertilization in vivo. The multiple-pocket sperm-bus provides a cooperative strategy of multiple self-propelled payloads. This system facilitates the loading of multiple cargos and transport of them at once. These three strategies for multiple sperm transport can not only work individually for different applications, but also be combined together for a more specific use in the future.

## 8. Conclusions and Outlook

### 8.1. Achievements

This dissertation presents a successful establishment of sperm-based micro-robotic systems on the application of drug delivery. Sperm, for the first time, are shown to serve as excellent candidates to carry anti-cancer drugs (DOX-HCl), attributable to their compact membrane system that acts as a protective layer surrounding the drug. One single bovine sperm can encapsulate 15 pg of DOX-HCl, while a human sperm can encapsulate 5 pg. The DOX-HCl transfer from the incubation solution into the sperm is driven by the binding of the drug on the sperm DNA. Almost all sperm including immotile ones can load DOX-HCl in the nucleus. DOX-HCl has no negative influence on bovine and human sperm, neither on the viability nor on the motility, as the sperm do not perform substance metabolism. In addition, sperm can swim through complex environments in an efficient manner not only due to their tail beating but also due to their membrane biochemistry. They remain functional in the human body for a longer time in comparison to other foreign cells (e.g. bacteria, fungi) due to their ability to inhibit the immune response by displaying specific proteins<sup>155</sup> and prostasomes<sup>156</sup> on the membrane. This reduces undesired immune response and thus makes this system more compatible to the host body.

In terms of the application for cancer treatment, the ability of sperm to fuse with somatic cells also confers them a unique property to deliver the drug locally into cancer cells through sperm-cell membrane fusion. Coupled with different types of magnetic microstructures, drug loaded sperm can be engineered to be micro-robotic systems that can be magnetically guided to the interest position, like cancer lesions, and release the sperm in a controlled way by means of specific trigger. Indeed, the tetrapod-like microstructure with 4 bendable arms works as a mechanical trigger for the sperm to escape when the arms reach the target, while the streamlined cap can discharge the sperm by abruptly flipping the cap with an external magnetic field. Compared to purely synthetic micromotors or other carriers, the here



proposed sperm-hybrid micromotor can encapsulate high concentrations of drug inside the sperm membrane and hence protect it from the dilution in the body fluids and enzyme degradation. In the foreseeable future, sperm can be also functionalized with imaging reporters such as infrared emitting molecules, radioactive isotopes or absorbing nanomaterials to improve image contrast in techniques such as optical imaging, positron emission tomography or optoacoustic tracking.<sup>190</sup> It will be intriguing to test how these micromotors perform *in vivo* in preclinical experiments, a key prerequisite for translating this technology to the clinic for future patient benefit. Such a system comprising guidable micro-enhancement and drug-loaded sperm can be envisioned to be employed in the future targeted cancer treatments in the female reproductive tract.

Environmental condition and material composition vary among different body fluids in human body. It is thus necessary for micromotors to adapt in different working environments. Propelled by sperm, a body-derived powerful propeller, sperm-hybrid micromotors can work not only in the reproductive system, but also in the blood. The sperm does not induce clotting or inflammation in the blood, while the blood composition has no deleterious effect on the sperm motility either. Equipped with a horn-like part, the streamlined sperm-motor can squeeze in the blood cells crowd so as to efficiently swim in blood with highly dense blood cells. The powerful propulsion provided by the sperm flagellum enables the sperm-motor to resist the blood at a high flow velocity comparable to the blood velocity in the microcirculation in human body. Gifted by nature, the sperm owns the rheotaxis ability to swim towards the wall and against the flow, enabling the sperm-motor to overcome stronger blood flow. By using specific guidance strategy, a ratchet-mechanism can help the sperm-motor swim against pulsing blood flow faster than 800  $\mu\text{m/s}$ . The coupled microstructure can be furthermore functionalized with anticoagulant drug. The drug loaded sperm-motor can then serve as an anticoagulant micro-surgeon which can inhibit the growing of the blood clots at desired locations after precise guidance.

Medical practice do not have much tolerance on inefficient transport of single micromotors one by one. From single to swarm, collective transport of sperm-motors stands as an important milestone on the way to the clinical application, showing value on increasing the

drug dose in this particular application. The self-assembled sperm-trains are employed to transport both multiple sperm and multiple cargo-loaded artificial parts. The tapered horn on the streamlined cap here acts as an anchor to connect to another cap by dipole-dipole attraction under magnetization. The assembled sperm-train is then propelled by the coupled multiple sperm and guided by the external magnetic field to the target. The slender shape enables it to go through narrow channels. Artificial caps and sperm can be finally released after the sperm-train is dissembled by abruptly flipping the magnetic field, realizing the targeted cargo delivery. This strategy can efficiently work as individuals and in swarm to transport multiple sperm in not only artificial cell medium but also ex vivo flowing blood.

To transport more sperm at once, a combined system of a magnetic microcourier and a protein-based microflake are utilized. Up to 50 motile sperm can be captured on the microflake at once without damage. The sperm captured microflake can be then transported by the helical microcourier under magnetic propulsion. When the microflake is enzymatically degraded by the body fluid, sperm can be released at the desired position to do the job of fertilization or cancer treatment if they are loaded with drug. This system can not only be used to efficiently transport sperm in a cluster, but also inspiring a new way to transport other biological organisms that needs special care. The strategy can be concluded as: encapsulate the sensitive organisms in a container, transport the loaded container by a micromotor and release the organisms out of the container at the presence of specific enzymes. Some other strategies for multiple sperm transport are also explored. For example, single sperm-motors with the same asymmetric shape of magnetic coatings can be aligned and guided to the same direction in the magnetic field. The fabrication is simple but the operation is not because sperm-motors starting from different positions cannot reach to the target at the same time. A multi-pockets sperm-bus shows up as another option. The sperm-bus loads multiple sperm in its pockets and is guided under the propulsion of these sperm to fulfill the goal of transport multiple sperm at once. Nonetheless, the coupling between the sperm and the sperm-bus has to be so firm to guarantee a stable propulsion that the sperm release comes out as an issue.

Finally, by realizing the navigation of the sperm-based micro-robotic system from single to multiple, this dissertation opens up the gate of sperm-based drug delivery and inspires its application in varieties of realistic body environments.

## 8.2. Outlook

Sperm-motors as a targeted delivery system represents a range of possibilities. For example, this non-invasive treatment could lead to the next generation of robotic medical procedure, especially towards the diseases in the female reproductive tract. In this scenario, sperm are loaded with essential medicines in advance and coupled with the guidable microstructures with certain release mechanisms. The administration route will be via the vagina and deep into the uterus at a location nearby the oviduct. The whole process does not induce any damage to the human body or exchange any substances with the circulation system of the human body. A 3D magnetic field will be used then to guide the cluster of these microsurgeons to the target. The precision can be extended to the scale on a single pathogen or injured cell. In addition, the sperm-motors can be also introduced through the blood as they can efficiently swim against the blood flow. Blood diseases or the disease sites with ruptured vessels (e.g. hepatitis) will be the target in this case. Such devices can be also engineered to carry genes, mRNA, imaging contrast agents or other substances of interest for diverse biomedical applications. On the exciting way of micromotors to the clinic, some milestones can be prospected.

### 8.2.1. Biology study

(1) It is necessary to investigate the drug loading mechanism before a mass of drugs are examined on sperm. The experiment can be done relying on mature molecular biological tools. Ion channels and translocators can be screened for a better understanding of the involving of the sperm membrane on the transmembrane transport of DOX-HCl or any other drugs during loading. Specific gene knockout can be used to load a specific drug by excluding the other out or provide a wide loading spectrum for multiple drugs as a cocktail therapy.

(2) The drug uptake mechanism by the targeted cell stays as another biochemical attraction. We confirmed the function of cell-fusion of the sperm on the DOX-HCl transfer, but the molecular participation behind this cell-fusion is still unknown.

#### 8.2.2. Robotics study

(1) Since micromotors were developed not earlier than 20 years ago, there has been no perfect one that can be applied in clinic so far. With respect to sperm, a cooperative microscale enhancement is needed. These enhancements should have a stable structure that can firmly couple the sperm, possess a sensitive response to the external guidance and a smart trigger to be controlled, be made of biocompatible and degradable material for the concern of the application safety. 3D lithography turns out to be an advantageous means to fabricate such structures. The next steps would be to include more editable materials, such as polyisopropylacrylamide as thermal sensitive trigger, polypyrrole as elastic joint, polyethylene dioxythiophene as conductive part to construct one micromotor with a compound system.

(2) The real-time tracking under deep tissue needs to be improved as the current imaging techniques (e.g. ultrasound and magnetic resonance imaging) are too coarse.<sup>34</sup> The recently developed photoacoustic imaging could be an answer for this. The micromotors could be polished with photosensitive surface, or modified with photo sensitive nanoparticles or quantum dots so that intense ultrasonic signal can be detected after efficient laser excitation.<sup>190</sup>

As a fascinating interdisciplinary study including biology, polymer science, photonics and robotics, to construct a sperm cyborg is never easy concerning the operation precision at the microscale and the coadaptation of the sensitive biological cell and the artificial enhancement. Nevertheless, as the abovementioned challenges are being answered step by step, patients in clinic will delightedly benefit from the sperm-motors. In this road, we hope that this dissertation can contribute to fulfill the great goal raised by Feynman: to apply the microscale surgeon in the human body.



## Bibliography:

1. Taylor, G. I. Analysis of the swimming of microscopic organisms. *Proc. R. Soc. London. Ser. A. Math. Phys. Sci.* **209**, 447–461 (1951).
2. Feynman, R. P. There's plenty of room at the bottom. *Calif. Inst. Technol. Eng. Sci. Mag.* (1960).
3. Fleischer, R. *Fantastic Voyage*. (20th Century Fox, 1966).
4. Wang, J. Nanomachines: fundamentals and applications. *John Wiley Sons* 119–138 (2013).
5. Medina-Sanchez, M., Xu, H. & Schmidt, O. G. Micro- and nano-motors: the new generation of drug carriers. *Ther. Deliv.* **9**, 303–316 (2018).
6. Allen, T. M. & Cullis, P. R. Liposomal drug delivery systems: From concept to clinical applications. *Adv. Drug Deliv. Rev.* **65**, 36–48 (2013).
7. Allen, T. M., Hansen, C. B. & de Menezes, D. E. L. Pharmacokinetics of long-circulating liposomes. *Adv. Drug Deliv. Rev.* **16**, 267–284 (1995).
8. Tannock, I. F., Lee, C. M., Tunggal, J. K., Cowan, D. S. & Egorin, M. J. Limited penetration of anticancer drugs through tumor tissue: a potential cause of resistance of solid tumors to chemotherapy. *Clin Cancer Res* **8**, 878–884 (2002).
9. World Medical Nanotechnology Congress 2017: Advances of Nanomedicine in Diagnosis Theanogtics. in October 18-19 (www.medicalnanotechnology.conferenceseries.com, 2017).
10. Chan, H.-K. & Kwok, P. C. L. Production methods for nanodrug particles using the bottom-up approach. *Adv. Drug Deliv. Rev.* **63**, 406–416 (2011).
11. Majumder, D. D., Banerjee, R., Ulrichs, C. H., Mewis, I. & Goswami, A. Nano-materials: Science of bottom-up and top-down. *IETE Tech. Rev.* **24**, 9–25 (2007).
12. Guozhong, C. *Nanostructures and nanomaterials: synthesis, properties and applications*. (World scientific, 2004).
13. Levinson, H. J. *Principles of lithography*. (SPIE Bellingham, WA, 2005).
14. Sun, H.-B. & Kawata, S. *Two-photon photopolymerization and 3D lithographic*

- microfabrication*. (Springer, 2004).
15. Baldacchini, T. *Three-dimensional microfabrication using two-photon polymerization: fundamentals, technology, and applications*. (William Andrew, 2015).
  16. Saleh, B. E. A. & Teich, M. C. *Fundamentals of photonics*. (John Wiley & Sons, 2019).
  17. Nolte, S. *et al.* Nanostructuring with spatially localized femtosecond laser pulses. *Opt. Lett.* **24**, 914–916 (1999).
  18. Boyd, R. W. *Nonlinear optics*. (Elsevier, 2003).
  19. Barnard, E. S. *et al.* Probing carrier lifetimes in photovoltaic materials using subsurface two-photon microscopy. *Sci. Rep.* **3**, 2098 (2013).
  20. Maruo, S., Nakamura, O. & Kawata, S. Three-dimensional microfabrication with two-photon-absorbed photopolymerization. *Opt. Lett.* **22**, 132–134 (1997).
  21. Nanoscribe GmbH. *Nanoscribe Photonic Professional User Manual*. (2015).
  22. Liao, C.-Y. *et al.* Two-dimensional slicing method to speed up the fabrication of micro-objects based on two-photon polymerization. *Appl. Phys. Lett.* **91**, 33108 (2007).
  23. Satoshi, K., Hong-Bo, S., Tomokazu, T. & Kenji, T. Finer features for functional microdevices. *Nature* **412**, 697–698 (2001).
  24. Richter, B. *et al.* Guiding Cell Attachment in 3D Microscaffolds Selectively Functionalized with Two Distinct Adhesion Proteins. *Adv. Mater.* **29**, 1604342 (2017).
  25. Marino, A. *et al.* A 3D Real-Scale, Biomimetic, and Biohybrid Model of the Blood-Brain Barrier Fabricated through Two-Photon Lithography. *Small* **14**, 1–9 (2018).
  26. Jeon, S. *et al.* Magnetically actuated microrobots as a platform for stem cell transplantation. *Sci. Robot.* **4**, 1–12 (2019).
  27. Solovev, A. A., Mei, Y., Ureña, E. B., Huang, G. & Schmidt, O. G. Catalytic microtubular jet engines self-propelled by accumulated gas bubbles. *Small* **5**, 1688–1692 (2009).
  28. Shah, R. K., Kim, J. & Weitz, D. A. Janus supraparticles by induced phase separation of nanoparticles in droplets. *Adv. Mater.* **21**, 1949–1953 (2009).
  29. Magdanz, V., Guix, M. & Schmidt, O. G. Tubular micromotors: from microjets to spermotors. *Robot. Biomimetics* **1**, 11 (2014).
  30. Wu, Z. *et al.* Self-Propelled Polymer-Based Multilayer Nanorockets for Transportation and Drug Release. *Angew. Chemie Int. Ed.* **52**, 7000–7003 (2013).

31. Purcell, E. M. Life at low Reynolds number. *Am. J. Phys.* **45**, 3–11 (1977).
32. Lauga, E. & Powers, T. R. The hydrodynamics of swimming microorganisms. *Reports Prog. Phys.* **72**, 96601 (2009).
33. Rafai, S., Jibuti, L. & Peyla, P. Effective viscosity of microswimmer suspensions. *Phys. Rev. Lett.* **104**, 98102 (2010).
34. Medina-Sánchez, M. & Schmidt, O. G. Medical microbots need better imaging and control. *Nature* **545**, 406–508 (2017).
35. Sundararajan, S., Lammert, P. E., Zudans, A. W., Crespi, V. H. & Sen, A. Catalytic motors for transport of colloidal cargo. *Nano Lett.* **8**, 1271–1276 (2008).
36. Kagan, D. *et al.* Rapid delivery of drug carriers propelled and navigated by catalytic nanoshuttles. *Small* **6**, 2741–2747 (2010).
37. Sanchez, S., Solovev, A. A., Harazim, S. M. & Schmidt, O. G. Microbots swimming in the flowing streams of microfluidic channels. *J. Am. Chem. Soc.* **133**, 701–703 (2010).
38. Gao, W. *et al.* Seawater-driven magnesium based Janus micromotors for environmental remediation. *Nanoscale* **5**, 4696–4700 (2013).
39. Gao, W., Pei, A. & Wang, J. Water-driven micromotors. *ACS Nano* **6**, 8432–8438 (2012).
40. Pantarotto, D., Browne, W. R. & Feringa, B. L. Autonomous propulsion of carbon nanotubes powered by a multienzyme ensemble. *Chem. Commun.* 1533–1535 (2008).
41. Hortelão, A. C., Patiño, T., Perez-Jiménez, A., Blanco, À. & Sánchez, S. Enzyme-Powered Nanobots Enhance Anticancer Drug Delivery. *Adv. Funct. Mater.* **28**, 1705086 (2018).
42. Wu, Y., Lin, X., Wu, Z., Möhwald, H. & He, Q. Self-Propelled Polymer Multilayer Janus Capsules for Effective Drug Delivery and Light-Triggered Release. *ACS Appl. Mater. Interfaces* **6**, 10476–10481 (2014).
43. Wu, Z., Lin, X., Zou, X., Sun, J. & He, Q. Biodegradable Protein-Based Rockets for Drug Transportation and Light-Triggered Release. *ACS Appl. Mater. Interfaces* **7**, 250–255 (2015).
44. Li, J. *et al.* Micromotors Spontaneously Neutralize Gastric Acid for pH-Responsive Payload Release. *Angew. Chemie Int. Ed.* **56**, 2156–2161 (2017).
45. de Ávila, B. E.-F. *et al.* Micromotor-enabled active drug delivery for in vivo treatment of stomach infection. *Nat. Commun.* **8**, 272 (2017).
46. Tu, Y., Peng, F., White, P. B. & Wilson, D. A. Redox-Sensitive Stomatocyte Nanomotors: Destruction and Drug Release in the Presence of Glutathione. *Angew. Chemie Int. Ed.*



- 129**, 7728–7732 (2017).
47. Tu, Y. *et al.* Biodegradable Hybrid Stomatocyte Nanomotors for Drug Delivery. *ACS Nano* **11**, 1957–1963 (2017).
  48. Wang, L. *et al.* Self-propelled manganese oxide-based catalytic micromotors for drug delivery. *RSC Adv.* **6**, 65624–65630 (2016).
  49. Baylis, J. R. *et al.* Self-propelled particles that transport cargo through flowing blood and halt hemorrhage. *Sci. Adv.* **1**, e1500379 (2015).
  50. Dreyfus, R. *et al.* Microscopic artificial swimmers. *Nature* **437**, 862–865 (2005).
  51. Zhang, L. *et al.* Artificial bacterial flagella: Fabrication and magnetic control. *Appl. Phys. Lett.* **94**, 64107 (2009).
  52. Mhanna, R. *et al.* Artificial bacterial flagella for remote-controlled targeted single-cell drug delivery. *Small* **10**, 1953–1957 (2014).
  53. Medina-Sánchez, M., Schwarz, L., Meyer, A. K., Hebenstreit, F. & Schmidt, O. G. Cellular Cargo Delivery: Toward Assisted Fertilization by Sperm-Carrying Micromotors. *Nano Lett.* **16**, 555–561 (2016).
  54. Schwarz, L., Medina-Sánchez, M. & Schmidt, O. G. Hybrid BioMicromotors. *Appl. Phys. Rev.* **4**, 31301 (2017).
  55. Wu, Z. *et al.* Turning erythrocytes into functional micromotors. *ACS Nano* **8**, 12041–12048 (2014).
  56. Shao, J. *et al.* Chemotaxis-Guided Hybrid Neutrophil Micromotors for Targeted Drug Transport. *Angew. Chemie Int. Ed.* **56**, 12935–12939 (2017).
  57. Hosseinidoust, Z. *et al.* Bioengineered and biohybrid bacteria-based systems for drug delivery. *Adv. Drug Deliv. Rev.* **106**, 27–44 (2016).
  58. Park, B.-W., Zhuang, J., Yasa, O. & Sitti, M. Multifunctional Bacteria-Driven Microswimmers for Targeted Active Drug Delivery. *ACS Nano* **11**, 8910–8923 (2017).
  59. Felfoul, O. *et al.* Magneto-aerotactic bacteria deliver drug-containing nanoliposomes to tumour hypoxic regions. *Nat. Nanotechnol.* **11**, 941–947 (2016).
  60. Ryan, K. J. & Ray, C. G. Medical microbiology. *McGraw Hill* **4**, 370 (2004).
  61. Donati, L. *et al.* Vaginal microbial flora and outcome of pregnancy. *Arch. Gynecol. Obstet.* **281**, 589–600 (2010).
  62. van Duijn Jr, C. Mensuration of the heads of bull spermatozoa. *Mikroskopie* **14**, 265–

276 (1960).

63. Rengan, A. K., Agarwal, A., van der Linde, M. & du Plessis, S. S. An investigation of excess residual cytoplasm in human spermatozoa and its distinction from the cytoplasmic droplet. *Reprod. Biol. Endocrinol.* **10**, 92 (2012).
64. Gravance, C. G., Vishwanath, R., Pitt, C., Garner, D. L. & Casey, P. J. Effects of Cryopreservation on Bull Sperm Head Morphometry. *J. Androl.* **19**, 704–709 (1998).
65. Van Dilla, M. A. *et al.* Measurement of mammalian sperm deoxyribonucleic acid by flow cytometry. Problems and approaches. *J Histochem Cytochem* **25**, 763–773 (1977).
66. Ishimoto, K. & Gaffney, E. A. Mechanical tuning of mammalian sperm behaviour by hyperactivation, rheology and substrate adhesion: a numerical exploration. *J. R. Soc. Interface* **13**, 20160633 (2016).
67. Medina-Sánchez, M., Magdanz, V., Schwarz, L., Xu, H. & Schmidt, O. G. Spermbots: Concept and Applications. in *Conference on Biomimetic and Biohybrid Systems* 579–588 (Springer, 2017).
68. Magdanz, V., Sanchez, S. & Schmidt, O. G. Development of a Sperm-Flagella Driven Micro-Bio-Robot. *Adv. Mater.* **25**, 6581–6588 (2013).
69. Magdanz, V., Medina-Sánchez, M., Chen, Y., Guix, M. & Schmidt, O. G. How to Improve Spermbot Performance. *Adv. Funct. Mater.* **25**, 2763–2770 (2015).
70. Magdanz, V. *et al.* Spermatozoa as Functional Components of Robotic Microswimmers. *Adv. Mater.* **29**, 1606301 (2017).
71. Kiyomiya, K., Matsuo, S. & Kurebe, M. Proteasome is a carrier to translocate doxorubicin from cytoplasm into nucleus. *Life Sci* **62**, 1853–1860 (1998).
72. Johnson, G. D. *et al.* The sperm nucleus: chromatin, RNA, and the nuclear matrix. *Reproduction* **141**, 21–36 (2011).
73. Kwon, G. S. & Okano, T. Polymeric micelles as new drug carriers. *Adv. Drug Deliv. Rev.* **21**, 107–116 (1996).
74. Srivastava, S. K., Medina-Sánchez, M., Koch, B. & Schmidt, O. G. Medibots: Dual-Action Biogenic Microdaggers for Single-Cell Surgery and Drug Release. *Adv. Mater.* **28**, 832–837 (2016).
75. Lin, X., Wu, Z., Wu, Y., Xuan, M. & He, Q. Self-Propelled Micro-/Nanomotors Based on Controlled Assembled Architectures. *Adv. Mater.* **28**, 1060–1072 (2016).
76. Wu, Z. *et al.* Near-infrared light-triggered “on/off” motion of polymer multilayer rockets. *ACS Nano* **8**, 6097–6105 (2014).

77. Bysell, H., Månsson, R., Hansson, P. & Malmsten, M. Microgels and microcapsules in peptide and protein drug delivery. *Adv. Drug Deliv. Rev.* **63**, 1172–1185 (2011).
78. Mattioli, M., Gloria, A., Mauro, A., Gioia, L. & Barboni, B. Fusion as the result of sperm-somatic cell interaction. *Reproduction* **138**, 679–687 (2009).
79. Bendich, A., Borenfreund, E. & Sternberg, S. S. Penetration of somatic mammalian cells by sperm. *Science* **183**, 857–859 (1974).
80. Higgins, P. J., Borenfreund, E. & Bendich, A. Appearance of foetal antigens in somatic cells after interaction with heterologous sperm. *Nature* **257**, 488–489 (1975).
81. Singh, J. & Wolfe, D. E. Review Nano and macro-structured component fabrication by electron beam-physical vapor deposition (EB-PVD). *J. Mater. Sci.* **40**, 1–26 (2005).
82. Zhou, W. *et al.* An efficient two-photon-generated photoacid applied to positive-tone 3D microfabrication. *Science* **296**, 1106–1109 (2002).
83. Xiong, L., Chen, P. & Zhou, Q. Adhesion promotion between PDMS and glass by oxygen plasma pre-treatment. *J. Adhes. Sci. Technol.* **28**, 1046–1054 (2014).
84. Kim, J.-M., Ji, E.-K., Woo, S. M., Lee, H. & Ahn, D. J. Immobilized Polydiacetylene Vesicles on Solid Substrates for Use as Chemosensors. *Adv. Mater.* **15**, 1118–1121 (2003).
85. Samardzija, M. *et al.* Effects of bovine spermatozoa preparation on embryonic development in vitro. *Reprod Biol Endocrinol* **4**, 58 (2006).
86. Tacar, O., Sriamornsak, P. & Dass, C. R. Doxorubicin: an update on anticancer molecular action, toxicity and novel drug delivery systems. *J. Pharm. Pharmacol.* **65**, 157–170 (2013).
87. Ishida, T., Atobe, K., Wang, X. & Kiwada, H. Accelerated blood clearance of PEGylated liposomes upon repeated injections: effect of doxorubicin-encapsulation and high-dose first injection. *J. Control. release* **115**, 251–258 (2006).
88. Kumar, R., Kulkarni, A., Nagesha, D. K. & Sridhar, S. In vitro evaluation of theranostic polymeric micelles for imaging and drug delivery in cancer. *Theranostics* **2**, 714–722 (2012).
89. Chudakov, D. M. *et al.* Photoswitchable cyan fluorescent protein for protein tracking. *Nat Biotechnol* **22**, 1435–1439 (2004).
90. Hathout, R. M., Mansour, S., Mortada, N. D. & Guinedi, A. S. Liposomes as an ocular delivery system for acetazolamide: in vitro and in vivo studies. *Aaps Pharmscitech* **8**, E1–E12 (2007).
91. Shi, G., Guo, W., Stephenson, S. M. & Lee, R. J. Efficient intracellular drug and gene

- delivery using folate receptor-targeted pH-sensitive liposomes composed of cationic/anionic lipid combinations. *J. Control. release* **80**, 309–319 (2002).
92. Liu, N. *et al.* Hyaluronan synthase 3 overexpression promotes the growth of TSU prostate cancer cells. *Cancer Res.* **61**, 5207–5214 (2001).
  93. Ince, T. A. *et al.* Characterization of twenty-five ovarian tumour cell lines that phenocopy primary tumours. *Nat. Commun.* **6**, 7419 (2015).
  94. Cho, K., Wang, X., Nie, S., Chen, Z. G. & Shin, D. M. Therapeutic nanoparticles for drug delivery in cancer. *Clin Cancer Res* **14**, 1310–1316 (2008).
  95. De Jong, W. H. & Borm, P. J. Drug delivery and nanoparticles: applications and hazards. *Int J Nanomedicine* **3**, 133–149 (2008).
  96. Tan, S., Wu, T., Zhang, D. & Zhang, Z. Cell or cell membrane-based drug delivery systems. *Theranostics* **5**, 863–881 (2015).
  97. Stuckey, D. W. & Shah, K. Stem cell-based therapies for cancer treatment: separating hope from hype. *Nat. Rev. Cancer* **14**, 683–691 (2014).
  98. Xuan, M., Shao, J., Dai, L., Li, J. & He, Q. Macrophage Cell Membrane Camouflaged Au Nanoshells for in Vivo Prolonged Circulation Life and Enhanced Cancer Photothermal Therapy. *ACS Appl. Mater. Interfaces* **8**, 9610–9618 (2016).
  99. Hamidi, M., Zarrin, A., Foroozesh, M. & Mohammadi-Samani, S. Applications of carrier erythrocytes in delivery of biopharmaceuticals. *J. Control. release* **118**, 145–160 (2007).
  100. Tanaka, Y. *et al.* An actuated pump on-chip powered by cultured cardiomyocytes. *Lab Chip* **6**, 362–368 (2006).
  101. Zhuang, J. & Sitti, M. Chemotaxis of bio-hybrid multiple bacteria-driven microswimmers. *Sci. Rep.* **6**, 32135 (2016).
  102. Akin, D. *et al.* Bacteria-mediated delivery of nanoparticles and cargo into cells. *Nat. Nanotechnol.* **2**, 441–449 (2007).
  103. Stanton, M. M., Simmchen, J., Ma, X., Miguel-López, A. & Sánchez, S. Biohybrid Janus Motors Driven by Escherichia coli. *Adv. Mater. Interfaces* **3**, 1500505 (2016).
  104. Stanton, M. M. *et al.* Biohybrid Microtube Swimmers Driven by Single Captured Bacteria. *Small* **13**, 1603679 (2017).
  105. Palffy, R. *et al.* Bacteria in gene therapy: bactofection versus alternative gene therapy. *Gene Ther* **13**, 101–105 (2005).

106. Makhluaf, S. B.-D., Abu-Mukh, R., Rubinstein, S., Breitbart, H. & Gedanken, A. Modified PVA-Fe<sub>3</sub>O<sub>4</sub> Nanoparticles as Protein Carriers into Sperm Cells. *Small* **4**, 1453–1458 (2008).
107. Geerts, N., McGrath, J., Stronk, J. N., Vanderlick, T. K. & Huszar, G. Spermatozoa as a transport system of large unilamellar lipid vesicles into the oocyte. *Reprod. Biomed. Online* **28**, 451–461 (2014).
108. Kiyomiya, K., Matsuo, S. & Kurebe, M. Mechanism of Specific Nuclear Transport of Adriamycin: the Mode of Nuclear Translocation of Adriamycin-Proteasome Complex. *Cancer Res.* **61**, 2467–2471 (2001).
109. Munerati, M., Cortesi, R., Ferrari, D., Di Virgilio, F. & Nastruzzi, C. Macrophages loaded with doxorubicin by ATP-mediated permeabilization: potential carriers for antitumor therapy. *Biochim. Biophys. Acta, Mol. Cell Res.* **1224**, 269–276 (1994).
110. Gill, D. R. *et al.* Separation of drug transport and chloride channel functions of the human multidrug resistance P-glycoprotein. *Cell* **71**, 23–32 (1992).
111. Batrakova, E. V *et al.* Effects of pluronic and doxorubicin on drug uptake, cellular metabolism, apoptosis and tumor inhibition in animal models of MDR cancers. *J. Control. release* **143**, 290–301 (2010).
112. Gur, Y. & Breitbart, H. Protein synthesis in sperm: dialog between mitochondria and cytoplasm. *Mol Cell Endocrinol* **282**, 45–55 (2008).
113. Jikeli, J. F. *et al.* Sperm navigation along helical paths in 3D chemoattractant landscapes. *Nat. Commun.* **6**, 7985 (2015).
114. Frimat, J. P. *et al.* Make it spin: individual trapping of sperm for analysis and recovery using micro-contact printing. *Lab Chip* **14**, 2635–2641 (2014).
115. Ishijima, S. Dynamics of flagellar force generated by a hyperactivated spermatozoon. *Reproduction* **142**, 409–415 (2011).
116. Nosrati, R., Graham, P. J., Liu, Q. & Sinton, D. Predominance of sperm motion in corners. *Sci. Rep.* **6**, 26669 (2016).
117. Grimes, D. R., Kelly, C., Bloch, K. & Partridge, M. A method for estimating the oxygen consumption rate in multicellular tumour spheroids. *J. R. Soc. Interface* **11**, 20131124 (2014).
118. Gwatkin, R. B. L. & Andersen, O. F. Effect of glycosidase inhibitors on the capacitation of hamster spermatozoa by cumulus cells in vitro. *J. Reprod. Fertil.* **35**, 565–567 (1973).
119. Ha, C. W. & Yang, D.-Y. Rotational elastic micro joint based on helix-augmented cross-spring design for large angular movement. *Opt. Express* **22**, 20789–20797 (2014).

120. Labidi-Galy, S. I. *et al.* High grade serous ovarian carcinomas originate in the fallopian tube. *Nat. Commun.* **8**, 1093 (2017).
121. Bowtell, D. D. *et al.* Rethinking ovarian cancer II: reducing mortality from high-grade serous ovarian cancer. *Nat. Rev. Cancer* **15**, 668–679 (2015).
122. Miller, K. D. *et al.* Cancer treatment and survivorship statistics, 2016. *CA. Cancer J. Clin.* **66**, 271–289 (2016).
123. Wilhelm, S. *et al.* Analysis of nanoparticle delivery to tumours. *Nat. Rev. Mater.* **1**, 16014 (2016).
124. Miller, M. R., Mansell, S. A., Meyers, S. A. & Lishko, P. V. Flagellar ion channels of sperm: similarities and differences between species. *Cell Calcium* **58**, 105–113 (2015).
125. Perreault, S. D., Barbee, R. R., Elstein, K. H., Zucker, R. M. & Keefer, C. L. Interspecies Differences in the Stability of Mammalian Sperm Nuclei Assessed in Vivo by Sperm Microinjection and in Vitro by Flow Cytometry. *Biol. Reprod.* **39**, 157–167 (1988).
126. Jager, S. Sperm Nuclear Stability and Male Infertility. *Arch. Androl.* **25**, 253–259 (1990).
127. Frattini, A. *et al.* High variability of genomic instability and gene expression profiling in different HeLa clones. *Sci. Rep.* **5**, 15377 (2015).
128. Wright, C. S. Structural comparison of the two distinct sugar binding sites in wheat germ agglutinin isolectin II. *J. Mol. Biol.* **178**, 91–104 (1984).
129. Wyrobek, A. J., Meistrich, M. L., Furrer, R. & Bruce, W. R. Physical characteristics of mouse sperm nuclei. *Biophys. J.* **16**, 811–825 (1976).
130. Komiya, A. *et al.* Sperm nuclear vacuoles in relation to acrosome reactions and sperm motility. *ScientificWorldJournal.* **2014**, 178970 (2014).
131. Patil, N. *et al.* Blocks of Limited Haplotype Diversity Revealed by High-Resolution Scanning of Human Chromosome 21. *Science* **294**, 1719–1723 (2001).
132. Chen, F. *et al.* Serous tubal intraepithelial carcinomas associated with high-grade serous ovarian carcinomas: a systematic review. *BJOG An Int. J. Obstet. Gynaecol.* **124**, 872–878 (2017).
133. Levanon, K. *et al.* Primary ex vivo cultures of human fallopian tube epithelium as a model for serous ovarian carcinogenesis. *Oncogene* **29**, 1103 (2009).
134. Kim, D.-H. *et al.* Biofunctionalized magnetic-vortex microdiscs for targeted cancer-cell destruction. *Nat. Mater.* **9**, 165–171 (2009).
135. Eliaz, R. E., Nir, S., Marty, C. & Szoka, F. C. J. Determination and modeling of kinetics of

- cancer cell killing by doxorubicin and doxorubicin encapsulated in targeted liposomes. *Cancer Res.* **64**, 711–718 (2004).
136. Masters, J. R. HeLa cells 50 years on: the good, the bad and the ugly. *Nat. Rev. Cancer* **2**, 315–319 (2002).
  137. Ben-David, U. *et al.* Genetic and transcriptional evolution alters cancer cell line drug response. *Nature* **560**, 325–330 (2018).
  138. Feeley, K. M. & Wells, M. Precursor lesions of ovarian epithelial malignancy. *Histopathology* **38**, 87–95 (2001).
  139. Gottesman, M. M. Mechanisms of Cancer Drug Resistance. *Annu. Rev. Med.* **53**, 615–627 (2002).
  140. Long, M. & Rack, H. J. Titanium alloys in total joint replacement—a materials science perspective. *Biomaterials* **19**, 1621–1639 (1998).
  141. Sanchez, S., Solovev, A. A., Schulze, S. & Schmidt, O. G. Controlled manipulation of multiple cells using catalytic microbots. *Chem. Commun.* **47**, 698–700 (2011).
  142. Harrison, R. A. Sperm plasma membrane characteristics and boar semen fertility. *J. Reprod. Fertil. Suppl.* **52**, 195–211 (1997).
  143. Zhao, G., Viehrig, M. & Pumera, M. Challenges of the movement of catalytic micromotors in blood. *Lab Chip* **13**, 1930–1936 (2013).
  144. Soler, L., Martínez-Cisneros, C., Swiersy, A., Sánchez, S. & Schmidt, O. G. Thermal activation of catalytic microjets in blood samples using microfluidic chips. *Lab Chip* **13**, 4299–4303 (2013).
  145. Venugopalan, P. L. *et al.* Conformal Cytocompatible Ferrite Coatings Facilitate the Realization of a Nanovoyager in Human Blood. *Nano Lett.* **14**, 1968–1975 (2014).
  146. Khalil, I. S. M. *et al.* Magnetic localization and control of helical robots for clearing superficial blood clots. *APL Bioeng.* **3**, 26104 (2019).
  147. Sherwood, L. *Human physiology: from cells to systems.* (Cengage learning, 2015).
  148. Waugh, A. & Grant, A. *Ross & Wilson Anatomy and physiology in health and illness E-book.* (Elsevier Health Sciences, 2014).
  149. Kolaczkowska, E. & Kubes, P. Neutrophil recruitment and function in health and inflammation. *Nat. Rev. Immunol.* **13**, 159–175 (2013).
  150. Champion, J. A., Walker, A. & Mitragotri, S. Role of Particle Size in Phagocytosis of Polymeric Microspheres. *Pharm. Res.* **25**, 1815–1821 (2008).

151. Xiang, S. D. *et al.* Pathogen recognition and development of particulate vaccines: Does size matter? *Methods* **40**, 1–9 (2006).
152. Miki, K. & Clapham, D. E. Rheotaxis guides mammalian sperm. *Curr. Biol.* **23**, 443–452 (2013).
153. Allen, W. E., Zicha, D., Ridley, A. J. & Jones, G. E. A Role for Cdc42 in Macrophage Chemotaxis. *J. Cell Biol.* **141**, 1147–1157 (1998).
154. Zhang, F. *et al.* A Macrophage–Magnesium Hybrid Biomotor: Fabrication and Characterization. *Adv. Mater.* **31**, 1901828 (2019).
155. Rooney, I. A., Oglesby, T. J. & Atkinson, J. P. Complement in human reproduction: activation and control. *Immunol Res* **12**, 276–294 (1993).
156. Kelly, R. W. *et al.* Extracellular organelles (prostasomes) are immunosuppressive components of human semen. *Clin Exp Immunol* **86**, 550–556 (1991).
157. Elgeti, J., Kaupp, U. B. & Gompper, G. Hydrodynamics of sperm cells near surfaces. *Biophys. J.* **99**, 1018–1026 (2010).
158. Tsukada, K., Minamitani, H., Sekizuka, E. & Oshio, C. Image correlation method for measuring blood flow velocity in microcirculation: correlation ‘window’ simulation and in vivo image analysis. *Physiol. Meas.* **21**, 459–471 (2000).
159. Goldsmith, H. L. & Turitto, V. T. Rheological aspects of thrombosis and haemostasis: basic principles and applications. *Thromb. Haemost.* **56**, 415–435 (1986).
160. Jacobs, M., Slaaf, D. W., Lemmens, H. A. J. & Reneman, R. S. The use of hemorheological and microcirculatory parameters in evaluating the effect of treatment in Raynaud’s phenomenon. *Vasc. Surg.* **21**, 9–16 (1987).
161. Zhang, Z. *et al.* Human sperm rheotaxis: A passive physical process. *Sci. Rep.* **6**, 1–8 (2016).
162. Klindt, G. S., Ruloff, C., Wagner, C. & Friedrich, B. M. Load Response of the Flagellar Beat. *Phys. Rev. Lett.* **117**, 1–5 (2016).
163. Manning, W. J., Katz, S. E., Douglas, P. S. & Silverman, D. I. Atrial ejection force: a noninvasive assessment of atrial systolic function. *J. Am. Coll. Cardiol.* **22**, 221–225 (1993).
164. Pastuszak, A. W. & Wang, R. Varicocele and testicular function. *Asian J. Androl.* **17**, 659–667 (2015).
165. Miller, J. D., Pegelow, D. F., Jacques, A. J. & Dempsey, J. A. Skeletal muscle pump versus respiratory muscle pump: modulation of venous return from the locomotor limb in



- humans. *J. Physiol.* **563**, 925–943 (2005).
166. Crowe, L. M. *et al.* Prevention of fusion and leakage in freeze-dried liposomes by carbohydrates. *Biochim. Biophys. Acta, Biomembranes* **861**, 131–140 (1986).
  167. Dhoot, N. O. & Wheatley, M. A. Microencapsulated liposomes in controlled drug delivery: strategies to modulate drug release and eliminate the burst effect. *J. Pharm. Sci.* **92**, 679–689 (2003).
  168. Maitz, M. F. *et al.* Bio-responsive polymer hydrogels homeostatically regulate blood coagulation. *Nat. Commun.* **4**, 2168 (2013).
  169. Sperling, C. *et al.* In vitro blood reactivity to hydroxylated and non-hydroxylated polymer surfaces. *Biomaterials* **28**, 3617–3625 (2007).
  170. Chen, W.-H. & Regen, S. L. Thermally Gated Liposomes. *J. Am. Chem. Soc.* **127**, 6538–6539 (2005).
  171. Han, K. *et al.* Sequence-encoded colloidal origami and microbot assemblies from patchy magnetic cubes. *Sci. Adv.* **3**, e1701108 (2017).
  172. Kangarlu, A. *et al.* Cognitive, cardiac, and physiological safety studies in ultra high field magnetic resonance imaging. *Magn. Reson. Imaging* **17**, 1407–1416 (1999).
  173. Tottori, S. *et al.* Magnetic helical micromachines: fabrication, controlled swimming, and cargo transport. *Adv. Mater.* **24**, 811–816 (2012).
  174. Frutiger, D. R., Vollmers, K., Kratochvil, B. E. & Nelson, B. J. Small, Fast, and Under Control: Wireless Resonant Magnetic Micro-agents. *Int. J. Rob. Res.* **29**, 613–636 (2009).
  175. Huang, T. Y. *et al.* Generating mobile fluidic traps for selective three-dimensional transport of microobjects. *Appl. Phys. Lett.* **105**, 114102 (2014).
  176. Schwarz, L., Medina-Sanchez, M., Magdanz, V. & Schmidt, O. G. Spermbots: Magnetic microrobots that assist sperm cells on their journey, opening new routes to assisted reproduction. *Reprod. Abstr.* **3**, 0033 (2016).
  177. Fisher, H. S., Giomi, L., Hoekstra, H. E. & Mahadevan, L. The dynamics of sperm cooperation in a competitive environment. *Proc. R. Soc. B Biol. Sci.* **281**, 20140296 (2014).
  178. Huszar, G. *et al.* Fertility testing and ICSI sperm selection by hyaluronic acid binding: Clinical and genetic aspects. *Reprod. Biomed. Online* **14**, 650–663 (2007).
  179. Huszar, G. *et al.* Hyaluronic acid binding by human sperm indicates cellular maturity, viability, and unreacted acrosomal status. *Fertil. Steril.* **79**, 1616–1624 (2003).

180. Hiyoshi, M. *et al.* Oviductin, the oviductal protease that mediates gamete interaction by affecting the vitelline coat in *Bufo japonicus*: Its molecular cloning and analyses of expression and posttranslational activation. *Dev. Biol.* **243**, 176–184 (2002).
181. Zhou, Z. *et al.* Preparation and characterization of hyaluronic acid hydrogel blends with gelatin. *J. Macromol. Sci. Part B Phys.* **51**, 2392–2400 (2012).
182. Adler-Nissen, J. *Enzymic hydrolysis of food proteins*. (Elsevier applied science publishers, 1986).
183. Voutsinas, L. P., Cheung, E. & Nakai, S. Relationships of Hydrophobicity to Emulsifying Properties of Heat Denatured Proteins. *Food Sci.* **48**, 26–32 (1983).
184. Murphy, K. P., Privalov, P. L. & Gill, S. J. Common features of protein unfolding and dissolution of hydrophobic compounds. *Science* **247**, 559–561 (1990).
185. Rawlings, N. D. & Barrett, A. J. Evolutionary families of peptidases. *Biochem. J.* **290**, 205–218 (1993).
186. Kan, F. W. K. & Esperanzate, P. W. Surface Mapping of Binding of Oviductin to the Plasma Membrane of Golden Hamster Spermatozoa During In Vitro Capacitation and Acrosome Reaction. *Mol. Reprod. Dev.* **766**, 8–9 (2006).
187. Adham, I. M., Nayernia, K. & Engel, W. Spermatozoa lacking acrosin protein show delayed fertilization. *Mol. Reprod. Dev. Inc. Gamete Res.* **46**, 370–376 (1997).
188. Lindsay, L. A. L., Yang, J. C. & Hedrick, J. L. Ovochymase, a *Xenopus laevis* egg extracellular protease, is translated as part of an unusual polyprotease. *Proc. Natl. Acad. Sci. U. S. A.* **96**, 11253–11258 (1999).
189. Barrett, A. J., Woessner, J. F. & Rawlings, N. D. *Handbook of proteolytic enzymes*. vol. 1 (Elsevier, 2012).
190. Aziz, A., Medina-Sánchez, M., Claussen, J. & Schmidt, O. G. Real-Time Optoacoustic Tracking of Single Moving Micro-objects in Deep Phantom and Ex Vivo Tissues. *Nano Lett.* **19**, 6612–6620 (2019).

# List of Figures

**Figure 1.** Prospective scenario of micromotors working in blood

**Figure 2.1.** Difference between single-photon and two-photon absorption processes on (a) energy level; (b) exposure area.

**Figure 2.2.** Typical FSTL setup

**Figure 2.3.** Examples of FSTL products: (a) Microcattle;<sup>23</sup> (b) Microscaffold for cell culture.<sup>24</sup>

**Figure 2.4.** Fabrications methods for micromotors

**Figure 2.5.** A microscale scallop in low Reynolds number conditions.

**Figure 2.6.** Three micromotor prototypes.<sup>34</sup>

**Table 1.** Details of chemical micromotors

**Figure 2.7.** (a) Structure of a bovine sperm. (b) SEM of the tubular spermbot.<sup>68</sup>

**Figure 3.1.** Design of the microtetrapod

**Figure 3.2.** Design of the SHC.

**Figure 3.3.** Design of the microcourier.

**Figure 3.4.** Fabrication of microtetrapods

**Figure 3.5.** PDMS channel fabrication

**Figure 3.6.** DOX-HCl loading in sperm

**Figure 4.1.** sperm loaded with (a) DOX-HCl; (b) FITC-BSA. (i), (ii), (iii) represent 10×, 40× and 3D reconstruction of z-stack images.

**Figure 4.2.** Encapsulation efficiency of DOX-HCl in sperm.

**Figure 4.3.** (a) Sperm motility after drug loading. (b) Stability of DOX-HCl loading in sperm.

**Figure 4.4.** Geometry of the microtetrapod. (a) SEM images. (b) Top view of the microtetrapod with schematic sperm head inside. (c) Finite element analysis results demonstrating the deformation of one single arm. Yellow arrows represent the applied forces. (i) 128 pN from a motile, non-hyperactivated sperm, and (ii) 450pN from a hyperactivated sperm.

**Figure 4.5.** Track (red line) of a sperm-hybrid motor under magnetic guidance in the (a) horizontal plane and (b) vertical plane. (c) Image sequence of a sperm release process when the arms hit the corner of a PDMS wall. Blue arrows point at the sperm head. Time lapse in min:s.

**Figure 4.6.** FITC-BSA distribution in a HeLa spheroid after the co-incubation of FITC-BSA loaded sperm with a HeLa spheroid. (a) Overlaid z-stack images. Red lines circle the spheroid. FITC-BSA is fluorescing in green under an excitation light of 470 nm. (b) Semi-quantitative analysis of the fluorescence intensity of the spheroid shown in (a). Area of BSA distribution describes the spreading area of FITC-BSA fluorescence signals on the spheroid, i.e. drug distribution. Integrated intensity describes the sum of fluorescence intensity in the red-circled spheroid in (a), which corresponds to the total amount of FITC-BSA in the spheroid.

**Figure 4.7.** Overlaid z-stack images of HeLa spheroids under treatment by DOX-HCl-loaded sperm. Red color shows the fluorescence of DOX-HCl under an excitation light with a wavelength of 470 nm. Blue arrows point at ruptured spheroids.

**Figure 4.8.** (a) Histogram of the percentage of live cells relative to the total amount of cells at different time points. ( $n = 4$ , cell count =  $10^4$  for each sample, \*  $p < 0.01$ , ANOVA analysis). (b) LIVE/DEAD staining images of cells from digested spheroids at 72 h.

**Figure 4.9.** (a) Schematic of the microfluidic chip for drug-loaded sperm transport and delivery. (b) Schematic depicting tumor targeted drug delivery by a sperm-hybrid micromotor under magnetic guidance with mechanical sperm release trigger.

**Figure 4.10.** (a) Image sequence of the sperm release process when the arms hit HeLa cells. Time lapse in min:s. Red arrows point at the sperm head. (b) DOX-HCl distribution in a HeLa spheroid with overlaid z-stack images of the fluorescence channel (20 images with a stack separation distance of 2  $\mu\text{m}$ ). Red arrows point at the sperm head.

**Figure 4.11.** SEM images showing the sperm-HeLa cell fusion. (i) Cell fusion with the DOX-HCl-loaded sperm; (ii) Cell fusion with an unloaded sperm. Red arrows point at a cell in apoptosis and the blue arrows point at live cells.

**Figure 5.1.** Human sperm-based drug-delivery system to target early ovarian cancer precursor lesions. Inset shows an alternative design for carrying human drug-loaded sperm.

**Figure 5.2.** DOX-HCl loading sperm. (a) Merged fluorescence and bright-field images of DOX-HCl-loaded sperm. Red color indicates autofluorescence of DOX-HCl. (b) Fluorescence and Airyscan images of two DOX-HCl-loaded human sperm, revealing the precise location of DOX-HCl inside sperm heads. Green indicates membrane staining by Alexa Fluor 488-conjugated wheat germ agglutinin (WGA). Red indicates DOX-HCl autofluorescence within sperm heads. (c) DOX-HCl localizes to the nucleus inside the sperm head. Detailed information on three different sperm cells. White arrows point at structures resembling nuclear vacuoles. DOX-HCl autofluorescence shown in red; Alexa Fluor 488-conjugated wheat germ agglutinin shown in green. (d) Percentage of motile sperm monitored over 8 h in unloaded and DOX-HCl-loaded human sperm (data represent means of two different samples, with a sperm count of 100 sperm per sample. Error bars represent standard deviations between samples).

**Figure 5.3. Anti-cancer effects of DOX-HCl loaded human sperm on Hela cells.** (a) Optical microscopy images of HeLa cell spheroids before and after 96 h of treatment with drug-loaded human sperm. (b) Survival rate of HeLa spheroid-derived cells after 96 h of

treatment (data represent means  $\pm$  standard deviations of  $n = 4$  independent biological replicates, HeLa cell count  $\sim 1.5 \times 10^5$  in blank spheroids. \*  $p < 0.01$ , ANOVA analysis).

**Figure 5.4. Anti-cancer effects of DOX-HCl loaded human sperm on HGSOC cells.** (a) Optical microscopy images of HGSOC cell spheroids before and after 96 h of treatment with drug-loaded human sperm. (b) Survival rate of HGSOC spheroid-derived cells after 96 h of treatment (data represent means  $\pm$  standard deviations of  $n = 4$  independent biological replicates, HeLa cell count  $\sim 1.5 \times 10^5$  in blank spheroids. \*  $p < 0.01$ , ANOVA analysis).

**Figure 5.5.** (a) Flow simulations of (i) a streamlined and (ii) a tubular sperm cap based on the same diameter and height. Finite element analysis tool: SOLIDWORKS Flow Simulation; flow medium: water; velocity:  $21 \mu\text{m/s}$  (the average velocity of a sperm at  $20^\circ\text{C}$  in HeLa medium); roughness: 0;  $f$ : total resistance. Biocompatibility evaluation of the microcaps. (b) Optical images of (i) microcaps treated group and (ii) cell medium control group. (c) HeLa cell survival after 3 days culture.

**Figure 5.6.** (a) Drug-loaded sperm approaching OCMI66 cell spheroid. (b) Transport of up to three human sperm using the proposed streamlined magnetic cap. (c) Magnetic guidance of a human sperm.

**Figure 5.7.** (a) Ejection mechanism of sperm from streamlined cap. The sperm head was regarded as an ellipse in its projective plane, in which the projection of the streamlined cap takes the shape of a semi-ellipsoid structure (blue line). The encapsulated sperm bears a drag force along its long axis (i) and can only move tangentially in the semi-ellipsoid structure of the cap. The cap swerving is carried out by rapidly changing the direction of the imposed magnetic field. In this situation the torque is always directed along the tangent line in the same direction of the drag force during continuous swerving of the cap (ii). Sperm escape occurs when the drag force becomes perpendicular to the tangent line (iii). After taking the wiggling angle of the sperm head ( $\theta$ ,  $57^\circ$ , middle panel) into account, the resultant critical decoupling angle is shown as  $\varphi$  ( $147^\circ$ ). (b) Guidance and release of a DOX-HCl-loaded human sperm onto an OCMI66 cell spheroid.

**Figure 6.1.** Concept of the blood-adapted SHC sperm-micromotors

**Figure 6.2.** (a) Hydrodynamic simulations of (i) tubular and (ii) SHC caps, assuming a swimming speed of 50  $\mu\text{m/s}$  and particles mimicking red blood cells of 5  $\mu\text{m}$  in diameter. Blue arrows point at the swimming direction. (b) SEM images of SHCs. The red arrow indicates the horn structure used for enhancing the micromotor motion in blood. Scale bar: 40  $\mu\text{m}$ .

**Figure 6.3.** (a) (i) Free sperm moving in 8 $\times$  diluted blood; Sperm-micromotors with (ii) a tubular and (iii) a SHC cap in static 8 $\times$  blood solution. (b) Image sequence of a SHC sperm-motor moving in static 2 $\times$  blood. Transparent blue region indicates the wake flow resulting from their motion. (c) Speed comparison of SHC sperm-micromotors varying with the dilution of whole blood and sperm medium.  $n=4$ . Scale bars: 40  $\mu\text{m}$ .

**Figure 6.4.** (a) Magnetic guidance of a SHC sperm-micromotor swimming against blood flow at a velocity of 0.167 mm/s. Scale bar: 40  $\mu\text{m}$ . (b) Rheotaxis of the sperm-micromotor. Chiral beating and imbalance of hydrodynamic force on posterior ( $F_p$ ) and anterior flagellum ( $F_a$ ), if  $F_p > F_a$ , a net lift force is generated on the flagellum, perpendicular to the flow direction. The lift force provides the sperm-micromotor a rheotactic velocity ( $V_r$ ) toward the wall, leading to a total swimming speed ( $U$ ) at an angle ( $\theta$ ) to the horizontal direction.

**Figure 6.5.** (a) Track of SHC sperm-micromotors against flowing blood at a velocity of (i) 0.042; (ii) 0.125; (iii) 0.167; (iv) 0.208; (v) 0.292 mm/s. The duration of the tracking in all cases was 3 s. Scale bar: 40  $\mu\text{m}$ . (b) Absolute swimming speed of SHC sperm-micromotors versus blood flow velocity. (i) Sperm-micromotor speed against varying flow velocity ( $n = 4$ ); (ii) Hysteresis loop of SHC sperm-micromotor speed against continuously changing blood flow.

**Figure 6.6.** (a) SHC sperm-micromotor swimming against pulsing blood flow at (i) 0.125 mm/s; (ii) 0.208 mm/s. ( $n = 4$ ). (b) Schematic of the ratchet brake mechanism: (i) Guiding the sperm-micromotor toward the substrate; (ii). Sperm-micromotor swimming without

flow; (iii) Ratchet brake against flow.  $F_m$ : magnetic torque.  $F_p$ : sperm propulsion.  $f$ : hydrodynamic resistance.  $F_i$ : blood flow impact.  $f_s$ : static friction.

**Figure 6.7.** (a) Fluorescence microscopy images of (i) blank SHC (ii) Alexa 488-Heparin loaded liposomes immobilized HSC. Scale bar: 20  $\mu\text{m}$ . (b) SEM of HSC immobilized with Heparin-loaded liposomes (50  $\mu\text{M}$ ). Scale bars: 3  $\mu\text{m}$  and 300 nm in the magnified image. (c) SEM images of SHCs immobilized with different concentrations of liposomes. (i) Bare SHCs. (ii) 100  $\mu\text{M}$ . (iii) 200  $\mu\text{M}$ . Scale bars: 200 nm.

**Figure 6.8.** (a) Activated clotting of the blood treated with (i) bare SHC sperm-micromotors and (ii) HLS sperm-micromotors. Red arrow points at fibrin clot. Scale bar: 100  $\mu\text{m}$ . (b) Coagulation cascade activation. ( $n = 6$ ). (c) Granulocyte activation. ( $n = 6$ ).

**Figure 7.1.** Magnetic assembly of SHCs. (a) Schematic of the assembling of two SHCs under magnetic field. (b) Magnetization simulations of a SHC and a 4-SHC sperm-train, both with partial iron coating. The metal coated part is colored in black. (c) A sperm-train swimming in sperm medium (SP-TALP). Red arrows point at the sperm heads. Scale bar: 100  $\mu\text{m}$ .

**Figure 7.2.** (a) A sperm-train swimming in sperm medium (SP-TALP). Blue arrows point at the sperm heads. (b) A troop of sperm-trains swimming in 4 $\times$  diluted blood. (c) Swimming speed of sperm-trains vs cap number. ( $n = 6$ ). (d) Track of a sperm-train and a SHC sperm-micromotor swimming against flowing blood. Scale bars: 100  $\mu\text{m}$ .

**Figure 7.3.** Concept of the transport of a cluster of motile sperm by the MC-MF system

**Figure 7.4.** Swimming performance of MCs. (a) SEM images of 3 microcouriers. (b) Swimming velocity of MC3 related to the rotating frequency of the magnetic field. (c) Motion sequence of MC3 guided in a rectangular track.

**Figure 7.5.** Overlaid motion sequence of the transport of a cluster of immotile sperm by MC2. Blue line and arrows depict the track of and directions of the MC movement. Green arrows point at the cluster of immotile sperm.



**Figure 7.6.** (a) Sperm capturing by a BSA-HA MF. Red arrows pointed at one sperm before and after being captured. Blue arrows point at a sperm being captured. (b) Transport of a motile sperm loaded MF by MC3. Blue and red lines depict the tracks of the movement before and after picking up the MF.

**Figure 7.7.** (a) Phase contrast images showing sperm release during MF hydrolysis by trypsin. (b) Sperm release numbers over time relative to the total captured numbers.

**Figure 7.8.** Sperm-bus for multiple sperm transport. (a) CAD Design. (b) Sperm capturing in the pocket. (c) Track of the movement of the sperm-bus propelled by coupled sperm.

# Selbständigkeitserklärung

Ich erkläre, dass ich die vorliegende Arbeit selbständig verfasst habe und keine anderen als die angegebenen Quellen und Hilfsmittel von mir genutzt wurden.

.....

Ort, Datum

.....

Unterschrift



# Acknowledgements

First of all, I would like to thank Prof. Oliver Schmidt for giving a chance to work in this wonderful institute. Thank him and Dr. Mariana Medina-Sanchez for their supervision on this research, including fruitful discussions, constructive suggestions and revisions on the manuscripts. Thank Prof. Dr. Klaus Reinhardt for agreeing to be my second supervisor and reviewing this dissertation.

I also thank Dr. Veronika Magdanz and Lukas Schwarz for the help at my starting in the research. Thank them for having shown me a wonderful sperm- and nano-world.

I thank Franziska Hebenstreit, Cornelia Krien, Dr. Martin Bauer, Sandra Nestler, Ronny Engelhard and all technicians who have helped me struggle out when I was trapped in the experiment mire.

I thank Dr. Christine Schmidt, Dr. Manfred Maitz and all collaborators in MCRC and IPF. Thank Wunan Zhang, Friedrich Striggow, Prof. Dr. Vladimir Fomin and all the other colleagues in MNBE group as well as in IIN. Many thanks to Chinese colleagues: Lixiang Liu, Dr. Gungun Lin, Dr. Xiaolei Sun, Dr. Xueyi Lu for the laughter in the working and daily life.

Finally, I thank my wife, Mingming Xu, for being the firmest support to me. Efficient work always starts from a harmonious family. When her virtue purifies my spiritual world, her wisdom also inspires my scientific life. I treasure this luck to be married with Muse so much that I always spur on myself to deserve this happiness, especially when Mingming shines me with some leaked sheen that her modesty cannot cover.



## Publications

(1) **Haifeng Xu**, Mariana Medina-Sanchez, Veronika Magdanz, Lukas Schwarz, Franziska Hebenstreit, and Oliver G. Schmidt. *Sperm-Hybrid Micromotor for Targeted Drug Delivery*. *ACS Nano* 2018 12 (1), 327-337. DOI: 10.1021/acsnano.7b06398.

(2) **Haifeng Xu**, Mariana Medina-Sanchez, Daniel R. Brison, Richard J. Edmondson, Stephen S. Taylor, Louisa Nelson, Kang Zeng, Steven Bagley, Carla Ribeiro, Lina P. Restrepo, Elkin Lucena, Christine K. Schmidt and Oliver G. Schmidt. *Human Spermrobots for Cancer-Relevant Drug Delivery*. *arXiv:1904.12684*. Submitted in April, 2019.

(3) **Haifeng Xu**, Mariana Medina-Sánchez, Manfred F. Maitz, Carsten Werner, Oliver G. Schmidt. *Sperm-Micromotors for Cargo Delivery through Flowing Blood*. *ACS Nano* 2020 14 (3), 2982-2993. DOI: 10.1021/acsnano.9b07851.

(4) **Haifeng Xu**, Mariana Medina-Sánchez, Oliver G. Schmidt. *Magnetic Micromotors for Multiple Motile Sperm Cells Capture, Transport, and Enzymatic Release*. *Angewandte Chemie International Edition* 2020. Doi:10.1002/anie.202005657.

(4) Mariana Medina-Sanchez, **Haifeng Xu**, Oliver G. Schmidt. *Micro- and nano-motors: the new generation of drug carriers*. *Therapeutic delivery* 2018 9 (4), 303-316. DOI: 10.4155/tde-2017-0113.

(5) Veronika Magdanz, Mariana Medina-Sanchez, Lukas Schwarz, **Haifeng Xu**, Jens Elgeti and Oliver G. Schmidt. *Spermatozoa as Functional Components of Robotic Microswimmers*. *Advanced Materials* 2017 29, 1606301. DOI: 10.1002/adma.201606301.

### Posters:

(1) **Haifeng Xu**, Mariana Medina-Sanchez, Lukas Schwarz, Veronika Magdanz, Franziska Hebenstreit and Oliver G. Schmidt. *Sperm-hybrid micromotor for drug delivery*. International Conference on Micro/Nanomachines 2017, August 26-28. (**Best Poster Award**)

(2) **Haifeng Xu**, Azaam Aziz, Jing Claussen, Christine Schmidt, Mariana Medina-Sánchez and Oliver G. Schmidt. *Steps further to the clinic: human based materials and in vivo real-time tracking*. International Conference on Micro/Nanomachines 2019, August 26-28.

# Curriculum Vitae

## Basic Information

Name	Haifeng Xu
Date of birth	10.07.1990
Place of birth	Jilin, China

## Scientific Education

**Master of Science, Pharmaceutics 2012- 2014**      Department of Pharmaceutics,  
school of Pharmaceutical Sciences, Health Science Center, Peking University.

**Bachelor of Science, Pharmacy 2008- 2012**      School of Pharmaceutical Sciences,  
Health Science Center, Peking University.

**PhD candidate, 2015- present**      Institute for Integrative  
Nanosciences, Leibniz Institute for Solid State and Materials Research Dresden

## Research Experience

**2012.2- 2014.6**      Master project on “Development of intelligent hydrogels based on  
poloxamer for nasal administration”      **Peking University**

**2012.10- 2013.4**      Involved in the program on “BSA labelling with FITC and development  
of a fluorescence detection method of protein”      **Peking University**

**2015- Present**      PhD project on “Custom-designed biohybrid micromotor for potential  
disease treatment”      **IFW Dresden**